

# Morphology and interaction between lipid domains

Tristan S. Ursell<sup>a</sup>, William S. Klug<sup>b</sup>, and Rob Phillips<sup>a,1</sup>

<sup>a</sup>Department of Applied Physics, California Institute of Technology, Pasadena, CA 91125; and <sup>b</sup>Department of Mechanical and Aerospace Engineering, Program in Biomedical Engineering, and California NanoSystems Institute, University of California, Los Angeles, CA 90095

Edited by L. B. Freund, Brown University, Providence, RI, and approved June 10, 2009 (received for review April 8, 2009)

**Cellular membranes are a heterogeneous mix of lipids, proteins and small molecules. Special groupings enriched in saturated lipids and cholesterol form liquid-ordered domains, known as “lipid rafts,” thought to serve as platforms for signaling, trafficking and material transport throughout the secretory pathway. Questions remain as to how the cell maintains small fluid lipid domains, through time, on a length scale consistent with the fact that no large-scale phase separation is observed. Motivated by these examples, we have utilized a combination of mechanical modeling and *in vitro* experiments to show that membrane morphology plays a key role in maintaining small domain sizes and organizing domains in a model membrane. We demonstrate that lipid domains can adopt a flat or dimpled morphology, where the latter facilitates a repulsive interaction that slows coalescence and helps regulate domain size and tends to laterally organize domains in the membrane.**

bilayer mechanics | lipid rafts | membrane morphology

The plasma and organelle membranes of cells are composed of a host of different lipids, lipophilic molecules, and membrane proteins (1). Together, they form a heterogeneous layer capable of regulating the flow of materials and signals into and out of the cell. Lipid structure and sterol content play a key role in bilayer organization, where steric interactions and energetically costly mismatch of lipid hydrophobic thickness result in a line tension that induces lateral phase separation (2). Saturated lipids and cholesterol are sequestered into liquid-ordered ( $L_o$ ) domains, often known as “lipid rafts,” distinct from an unsaturated liquid-disordered ( $L_d$ ) phase (3–5). Domains whose lipids include saturated sphingolipids and cholesterol, with sizes in the range of  $\approx 50$ –500 nm, have been implicated in a range of biological processes from lateral protein organization and virus uptake to signaling and plasma-membrane tension regulation (6–18). In the biological setting, maintenance of small domain size is thought to arise from a combination of lipid recycling and energetic barriers to domain coalescence (19–21) [potentially provided by transmembrane proteins (22)], ostensibly resulting in a stable distribution of domain sizes. These biological examples serve as a motivation to better understand the biophysical mechanisms that maintain small lipid domains over time and pose challenges to the classical theories of phase-separation and “domain ripening” [such as Cahn–Hilliard kinetics (23)].

A simple physical model that describes the evolution of lipid domain size and position predicts that domains diffuse and coalesce, such that the number of domains constantly decreases, whereas the average domain size constantly increases (23). Indeed, models of 2D phase separation have been studied in detail for many physical systems (24–27), and where the phase boundary is unfavorable and characterized by an energy per unit length (28), the domain size grows continuously (23, 29, 30). However, membranes can adopt 3D morphologies that affect the kinetics of phase separation (31–35). In those cases where morphology is considered as part of the phase separation model, previously uncharacterized coalescence kinetics emerge (32). Experimentally, model membranes have shown that nearly complete phase separation on the surface of a giant unilamellar vesicle can be reached in as little as 1 minute (3). With these facts in mind, our central questions are: How can model membranes that have phase separated maintain a distribution of small domain sizes on long time scales and short length scales? Are there membrane-mediated

(i.e., elastic) forces that inhibit coalescence and spatially organize domains?

We begin to answer these questions by examining the energetics of the membrane using a linear elastic model. A phase-separated membrane is endowed with bending stiffness, membrane tension, an energetic cost at the phase boundary, and domains of a particular size. Membrane bending and tension establish a natural length scale over which a morphological instability develops that switches domains from a flat to “dimpled” shape, similar to classical Euler buckling (36) (see Fig. 1). The dimpling instability is size-selective and “turns on” a membrane-mediated interaction that inhibits domain coalescence. This transition is a precursor to budding and is distinct from transitions that require spontaneous curvature. Although variations in membrane composition may change specific parameter values, the mechanical effects we describe are generic. Thus, these systems exhibit shape-dependent coarsening kinetics that are relevant for a broad class of 2D phase-separating systems. The interaction between domains is a mechanical effect, and we use a model treating dimpled domains as curved rigid inclusions to distill the main principles governing this interaction. Experimentally, we use a model mixture of lipids and cholesterol to show that such an interaction exists between dimpled domains and is well approximated by a simple model. We hypothesize that a combination of lipid recycling (19) and elastic interactions could serve as a mechanism for the organization of domains and the maintenance of small domain sizes in cellular membranes.

The first section of the article outlines the energetic contributions to the mechanical model and predicts the conditions under which domain dimpling occurs. The second section outlines how dimpled domains facilitate an elastic interaction and compares the model interaction to our measurements made in phase-separated giant unilamellar vesicles.

## Elastic Model and Morphological Transitions

The energetics of a lipid domain are dominated by a competition—on one hand, the applied membrane tension and bending stiffness both energetically favor a flat domain; on the other hand, the phase boundary line tension prefers any domain morphology (in 3D) that reduces the boundary length. We use a continuum mechanical model that couples these effects, relating the energetics of membrane deformation to domain morphology. As we will show, this competition results in a morphological transition from a flat to dimpled domain shape, where 2 dimpled domains are then capable of interacting elastically.

Lipid domains in a liquid state naturally adopt a circular shape to minimize the phase boundary length (3), allowing us to formulate our continuum mechanical model in polar coordinates. We employ a Monge representation, where the membrane mid-plane is described by a height function  $h(\mathbf{r})$  in the limit of small membrane deformations (i.e.,  $|\nabla h| < 1$ ). With this height

PHYSICS

BIOPHYSICS AND COMPUTATIONAL BIOLOGY

Author contributions: T.S.U. and W.S.K. performed research; T.S.U. analyzed data; and T.S.U., W.S.K., and R.P. wrote the paper.

The authors declare no conflict of interest.

This article is a PNAS Direct Submission.

<sup>1</sup>To whom correspondence should be addressed. E-mail: phillips@pboc.caltech.edu.

This article contains supporting information online at [www.pnas.org/cgi/content/full/0903825106/DCSupplemental](http://www.pnas.org/cgi/content/full/0903825106/DCSupplemental).

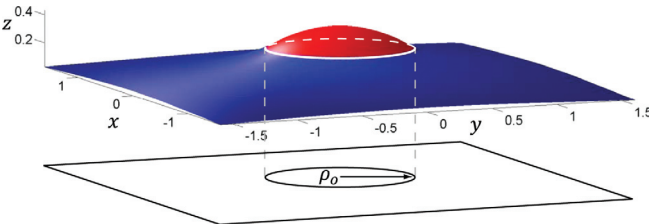


**Fig. 1.** Three-dimensional rendering of a dimpled lipid domain in dimensionless coordinates. For a domain (shown in red), a competition between bending, membrane tension and phase boundary line tension results in a morphological transition from a flat to a dimpled state as depicted. The dimple costs bending energy but reduces line tension energy by reducing the phase boundary length (shown as a white line around the domain). This morphology facilitates interactions between domains that significantly alter the kinetics of coalescence and lateral lipid organization. The dimensionless projected domain radius is  $\rho_o = r_o/\lambda_2$ , where  $r_o$  is projected radius, and  $\lambda_2$  is the elastic decay length.

function, we characterize how membrane tension, bending, spontaneous curvature, and line tension all contribute to domain energetics.

Changes in membrane height alter the projected area of the membrane and hence do work against the applied membrane tension, resulting in an increase in energy written as

$$G_{\text{tens}} = \pi\tau \left( \int_0^{r_o} (\nabla h_1)^2 r dr + \int_{r_o}^{\infty} (\nabla h_2)^2 r dr \right), \quad [1]$$

where  $\tau$  is the constant membrane tension,  $r_o$  is the projected radius of the domain,  $h_1$  is the height function of the domain, and  $h_2$  is the height function of the surrounding membrane (37, 38). Membrane curvature is penalized by the bending stiffness with a bending energy written as (37, 39)

$$G_{\text{bend}} = \pi\kappa_b^{(2)} \left( \sigma \int_0^{r_o} (\nabla^2 h_1)^2 r dr + \int_{r_o}^{\infty} (\nabla^2 h_2)^2 r dr \right). \quad [2]$$

This model allows the domain and surrounding membrane to have differing stiffnesses,  $\kappa_b^{(1)}$  and  $\kappa_b^{(2)}$  respectively, characterized by the parameter  $\sigma = \kappa_b^{(1)}/\kappa_b^{(2)}$ , and from this point on we drop the superscript on  $\kappa_b^{(2)}$ . Recent experiments suggest that the bending moduli of a cholesterol-rich domain and the surrounding membrane are approximately equal (5, 40), and hence for simplicity, we assume that the bending moduli of the 2 regions are equal (i.e.,  $\sigma = 1$ ), unless otherwise noted. In addition to bending stiffness, the domain may exhibit a preferred “spontaneous” curvature due, for instance, to lipid asymmetry (35, 41). The contribution of domain spontaneous curvature can be simplified to a boundary integral that couples to the overall curvature field by

$$G_{\text{spont}} = -2\pi\sigma\kappa_b c_o \int_0^{r_o} (\nabla^2 h_1) r dr = -2\pi\sigma\kappa_b c_o r_o \epsilon, \quad [3]$$

where  $c_o$  is the spontaneous curvature of the domain, and  $\epsilon$  is the membrane slope at the phase boundary. Furthermore, we assume the saddle-splay curvature moduli are equal in the 2 regions, yielding no dependence on Gaussian curvature. In principle, this contribution could be accounted for with a boundary term, explored in detail in supporting information (SI) Appendix. The phase boundary line tension is applied to the projected circumference of the domain, as shown in Fig. 1, by  $G_{\text{line}} = 2\pi r_o \gamma$ , where  $\gamma$  is the energy per unit length at the phase boundary.

Finally, a constraint must be imposed that relates the actual domain area,  $\mathcal{A}$ , to the projected domain radius  $r_o$ . The energetic cost to change the area per lipid molecule is high [ $\approx 50\text{--}100 k_B T/\text{nm}^2$  where  $k_B = 1.38 \times 10^{-23} \text{ J/K}$  and  $T = 300 \text{ K}$  (42)];

hence, we assume the domain area is conserved during any morphological change (see SI Appendix for details). We impose this constraint using a Lagrange multiplier,  $\tau_o$ , with units of tension by

$$G_{\text{area}} = \tau_o \left( \pi \int_0^{r_o} (\nabla h_1)^2 r dr + \pi r_o^2 - \mathcal{A} \right). \quad [4]$$

This results in an effective membrane tension within the domain  $\tau_1 = \tau + \tau_o$ , which must be negative to induce dimpling. Examining the interplay between bending and membrane tension, we see that 2 natural length scales emerge—within the domain we define  $\lambda_1 = \sqrt{\sigma\kappa_b/\tau_1}$ , and outside the domain we define  $\lambda_2 = \sqrt{\kappa_b/\tau}$ . These length scales allow us to define the relevant dimensionless parameters in this system.

The total free energy of an elastic domain and its surrounding membrane is then the sum of these 5 terms,  $G = G_{\text{tens}} + G_{\text{bend}} + G_{\text{spont}} + G_{\text{line}} + G_{\text{area}}$ . Details on all the terms in the free energy can be found in SI Appendix. With this free energy in hand, we examine how the morphology of a circular domain evolves as we tune domain size and the elastic properties of the membrane.

The height field and radius can be rescaled by the elastic decay lengths such that the Euler–Lagrange equation for the domain can be written in the parameter-free form  $\nabla^2(\nabla^2 + \beta^2)\eta_1 = 0$ , whereas the equation for the surrounding membrane is  $\nabla^2(\nabla^2 - 1)\eta_2 = 0$ , where the dimensionless variables are defined by  $\lambda_2 \eta_i = h_i$ ,  $\lambda_2 \rho = r$ ,  $\lambda_2 \rho_o = r_o$  and  $\beta = i\lambda_2/\lambda_1$ . Using the same dimensionless notation, the energy from line tension and spontaneous curvature can be written as  $G_{\text{line}} = 2\pi\kappa_b \rho_o \chi$  and  $G_{\text{spont}} = -2\pi\sigma\kappa_b \epsilon \rho_o v_o$ , with  $v_o = \lambda_2 c_o$  and  $\chi = \gamma\lambda_2/\kappa_b$ . The dimensionless line tension,  $\chi$ , is simply a rescaled version of the line tension  $\gamma$  and is 1 of 2 key parameters that characterize the morphological transition; the dimensionless domain area,  $\alpha = \mathcal{A}/\lambda_2^2$ , is the second key parameter.

The admissible solutions for  $\eta_1(\rho)$  and  $\eta_2(\rho)$  are zeroth order Bessel functions  $J_0(\beta\rho_o)$  and  $K_0(\rho_o)$ , respectively, with the boundary conditions  $|\nabla\eta_1(0)| = |\nabla\eta_2(\infty)| = 0$  and  $|\nabla\eta_1(\rho_o)| = |\nabla\eta_2(\rho_o)| = \epsilon$ . The boundary slope,  $\epsilon$ , is the parameter that indicates the morphology of the domain;  $\epsilon = 0$  indicates a flat domain, whereas  $0 < |\epsilon| \lesssim 1$  indicates a dimpled domain. The 5 contributions to membrane deformation energy yield a relatively simple expression for the total free energy, given by

$$G = \pi\kappa_b \rho_o \left[ \epsilon^2 \left( \sigma\beta \frac{J_0(\beta\rho_o)}{J_1(\beta\rho_o)} + \frac{K_0(\rho_o)}{K_1(\rho_o)} \right) + 2(\chi - \epsilon\sigma v_o) \right] - \kappa_b(\sigma\beta^2 + 1)(\pi\rho_o^2 - \alpha). \quad [5]$$

Mechanical equilibrium is enforced by rendering the energy stationary with respect to the unknown parameters  $\epsilon$ ,  $\rho_o$ , and  $\beta$ ,

$$\frac{\partial G}{\partial \epsilon} = 0, \quad \frac{\partial G}{\partial \rho_o} = 0, \quad \frac{\partial G}{\partial \beta} = 0. \quad [6]$$

These equilibrium equations physically correspond to torque balance at the phase boundary, lateral force balance at the phase boundary, and domain area conservation, respectively.

Analysis of the equilibrium equations reveals a second-order transition at a critical line-tension,  $\chi_c$ , as shown in Fig. 2. For  $\chi$  less than this critical value, only the flat, trivial solution with  $\epsilon = 0$  exists. At  $\chi_c$  a nontrivial solution describing buckled or dimpled morphologies emerges. For zero spontaneous curvature, the bifurcation is defined by a transcendental characteristic equation

$$\sigma\beta \frac{J_0(\beta\rho_o)}{J_1(\beta\rho_o)} + \frac{K_0(\rho_o)}{K_1(\rho_o)} = 0, \quad [7]$$

with  $\beta = \sqrt{(\chi_c/\rho_o - 1)/\sigma}$  and  $\rho_o = \sqrt{\alpha/\pi}$ . For a given dimensionless domain area,  $\alpha$ , this defines the critical line tension required to dimple the domain. In Fig. 2A Inset, this relation is used to generate a morphological phase diagram that shows where in the

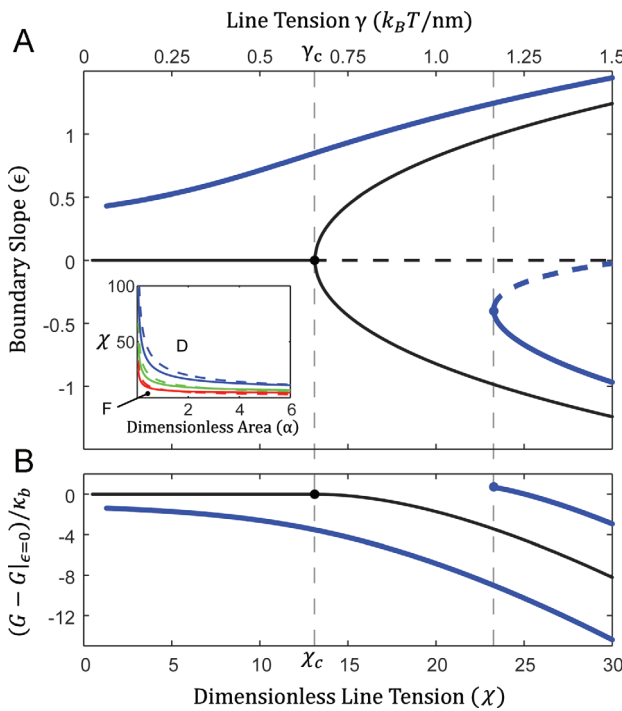


**Fig. 2.** Bifurcation diagram for dimpling transition at constant area (dimensionless domain area  $\alpha = \pi/4$ , bending modulus  $\kappa_b = 25 k_B T$ , elastic decay length  $\lambda_2 = 500$  nm, ratio of bending moduli  $\sigma = 1$ ). Constant line tension and increasing area produces a qualitatively similar graph. (A) At zero spontaneous curvature ( $v_o = 0$ , thin black line) the bifurcation is symmetric, the upper and lower branches are at the same energy, and the flat domain,  $\epsilon = 0$ , becomes unstable above the critical point (horizontal black dashed line). With finite spontaneous curvature [ $v_o = 2$ ,  $c_o = (250 \text{ nm})^{-1}$ , thick blue line] the lower energy branch (upper) has nonzero boundary slope for all line tensions, asymptoting to the zero spontaneous curvature branch. At a line tension slightly higher than the critical line tension,  $\chi_c$ , for the zero spontaneous curvature case, a bifurcation yields a higher energy dimple with the opposite curvature as  $v_o$  (indicated by the second vertical dashed line). (Inset) Equilibrium phase diagrams for bending moduli ratios of  $\sigma = 0.5$  (red),  $\sigma = 1$  (green), and  $\sigma = 2$  (blue) (the dashed lines are the approximation of Eq. 8) showing flat (F) and dimpled (D) domains. (B) Energy difference between the flat and dimpled state, normalized by the bending modulus  $\kappa_b$ , for domains with and without spontaneous curvature ( $v_o = 0 \rightarrow$  thin black line;  $v_o = 2 \rightarrow$  thick blue line).

space of dimensionless domain area and line tension we find the discontinuous transition (i.e., bifurcation) from a flat domain to a dimpled domain. Near the morphological transition the boundary slope grows as  $|\epsilon| \propto \sqrt{\chi/\chi_c - 1}$ , indicating that a dimple rapidly deviates from the flat state. The transition is symmetric, in that both possible dimple curvatures have the same energy, and hence the domain is equally likely to dimple upwards or downwards. In the experimentally relevant limit of small dimensionless domain area, the complexity of Eq. 7 is reduced to

$$\chi_c \sqrt{\alpha} = \frac{\gamma_c}{\kappa_b} \sqrt{\mathcal{A}} \simeq 8\sigma\sqrt{\pi}. \quad [8]$$

This leads to the conclusion that the dominant parameter governing domain dimpling at zero spontaneous curvature is  $\chi\sqrt{\alpha}$ . For a small domain, the dimpling transition is directly regulated by domain area, the bending modulus, and line tension but only weakly depends on applied membrane tension. Intuitively, domains dimple when line tension or domain size increase, as shown in Fig. 2A Inset. Likewise, a decrease in bending stiffness can also induce dimpling. The effects of applied membrane tension are weak because the change in projected area upon dimpling does not lead to a significant energy cost relative to the cost of bending and line tension.

If membrane elastic properties are fixed (i.e., fixed  $\kappa_b$ ,  $\tau$  and  $\gamma$ ), the dimpling-induced interactions “turn on” only after a critical domain size is achieved. This scenario is encountered when 2 domains, too small to dimple on their own, diffusively coalesce into a larger domain capable of dimpling and hence interacting. Indeed, such a size-selective coalescence mechanism was observed recently in model membrane vesicles (43). This constitutes a distinct class of coarsening dynamics, where classical diffusion-limited kinetics are obeyed until the domain size distribution has matured past the critical size for dimpling—then domain coalescence is a relatively slow, interaction-limited process.

For the model domain considered in Fig. 2, with area  $\alpha = \pi/4$  ( $r_o \simeq 250$  nm), the critical dimensionless line tension is  $\chi_c \simeq 13$ , corresponding to a critical line tension of  $\gamma_c \simeq 0.65 k_B T/\text{nm}$  ( $1 k_B T/\text{nm} = 4.14 \text{ pN}$ ). This value compares well with theoretical estimates of the line tension (28, 44) and falls squarely in the range of values from AFM measurements (2), though it is slightly higher than the value of  $\gamma \simeq 0.22 k_B T/\text{nm}$  measured via shape analysis of fully phase-separated vesicles (5) and  $\gamma \simeq 0.40 k_B T/\text{nm}$  measured from micropipette aspiration experiments (45). In general, measured values of the line tension depend heavily on bilayer composition, spanning a range of  $\approx 0.05 - 1.5 k_B T/\text{nm}$  (2, 5, 45).

Spontaneous curvature does not affect the Euler–Lagrange equations and, hence, will not effect the class of equilibrium membrane shapes. However, domains with zero and nonzero spontaneous curvature exhibit qualitatively different behavior. Membranes can be asymmetric with respect to leaflet composition (6, 46, 47), endowing a domain with potentially large spontaneous curvature. The energetic contribution from spontaneous curvature takes the form of an additional line tension depending linearly on the slope taken by the domain boundary,  $\epsilon$ . This breaks the symmetry of the membrane, giving an energetic preference to a dimple with the same curvature as the spontaneous curvature and eliminating the trivial  $\epsilon = 0$  solution even at small line tensions. As line tension increases, a bifurcation produces a second, stable, higher-energy dimple of the opposite curvature as  $v_o$ . The more energetically stable branch of this transition corresponds to a dimpled state for all values of line tension and nonzero values of domain area, as demonstrated in Fig. 2A. This predicts that as soon as a domain with finite spontaneous curvature forms, it dimples, regardless of size, and begins to experience interactions with any nearby dimpled domains. It is reasonable to expect that domains with similar composition will have similar spontaneous curvature, and hence form dimples whose curvature has the same sign. As we will show, dimples whose curvature has the same sign tend to interact repulsively. Such a mechanism of coalescence inhibition was observed recently in simulation (35). This indicates that control of spontaneous curvature via domain composition can regulate dimpling and hence, domain interaction (47, 48). Indeed, recent theoretical (49) work shows that lipid asymmetry leads to precisely these kinds of dimpled domains.

Calculated shapes of dimpled domains induced by line tension and spontaneous curvature are shown in Fig. 3A, alongside dimpled domains observed on giant unilamellar vesicles, shown in Fig. 3B and D.

### Elastic Interactions of Dimpled Domains

Given 2 domains that have met the criteria for dimpling, the deformation in the membrane surrounding the domains mediates an elastic interaction when they are within a few elastic decay lengths ( $\lambda_2$ ) of each other. This equips us to begin addressing how small membrane domains might be achieved on short and long time scales. As previously stated, free diffusion sets the maximum rate at which a quenched membrane can evolve into a fully phase-separated membrane (23), where this evolution can happen in as little as a minute on the surface of a giant unilamellar vesicle (GUV) (3). By comparison, recycling and, hence, homogenization

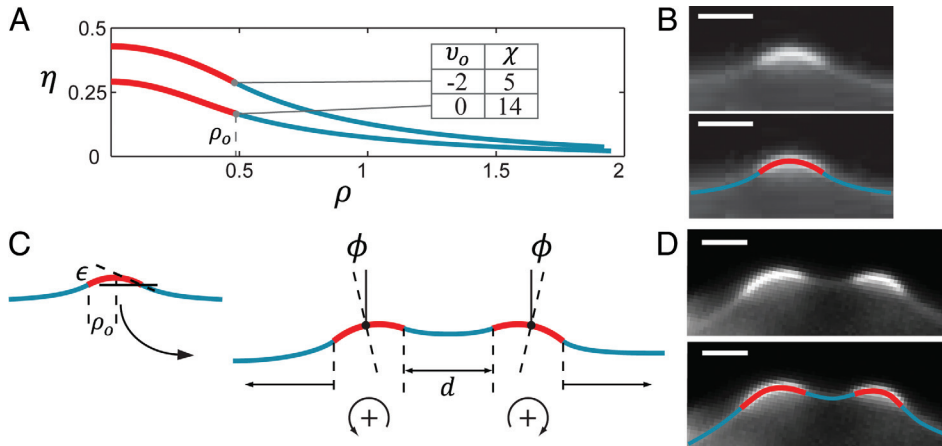


**Fig. 3.** Theoretical and experimental dimpled domain shapes. Domains are shown as thicker red lines, surrounding membrane as thinner blue lines. (A) The dimensionless height profile ( $\eta$ ) as a function of dimensionless radius ( $\rho$ ) for minimum energy dimples with and without spontaneous curvature (dimensionless spontaneous curvature,  $v_0$ , and line tension,  $\chi$ , are indicated in the legend; dimensionless domain area  $\alpha = \pi/4$ ). (B) Epifluorescence cross-section of a dimple on the surface of a GUV; the red and blue lines are a guide to the eye. (C) 1D model of interaction—dimples maintain shape, but tilt ( $\phi$ ) as a function of separation distance ( $d$ ). Dimples with the same sign of curvature repel, whereas dimples with opposite sign attract. The single domain shape, with boundary slope  $\epsilon$  and dimensionless projected radius  $\rho_0$  is shown for reference. (D) Epifluorescence cross-section of 2 dimpled domains interacting on the surface of a GUV. (Scale bars, 3  $\mu\text{m}$ .)

of cellular membrane is a process that takes place on the time scale of an hour or more (50). Our measurements of domain interactions (detailed below and other data shown in *SI Appendix*) estimate the coalescence barrier between dimpled domains at  $\approx 5 - 10 k_B T$ . Hence, given the diffusion-limited rate of coalescence, interactions slow this process by approximately  $e^{-5} \approx 0.007$  to  $e^{-10} \approx 0.00005$ .

The physical origin of domain interaction is explained by a simple model based on the assumption that the dimpled domain shape is constant during interaction, but the domains are free to tilt by an angle  $\phi$ , as shown in Fig. 3C. This assumption was, in part, inspired by experimental observations of domain shapes on the surface of giant unilamellar vesicles, as shown, for example, in Fig. 3D. The interaction energy is approximately an order of magnitude less than the free energy associated with the morphological transition itself (see Fig. 2B), thus interaction does not perturb the domain shape significantly. Only allowing domains to rotate simplifies the interaction between 2 domains to a change in the boundary conditions in the 3 regions of interest, shown in blue in Fig. 3C. Applying the small gradient approximation, the boundary slope is given by  $|\epsilon - \phi|$  in the outer regions and by  $|\epsilon + \phi|$  in the inner region. With the single domain boundary slope,  $\epsilon$ , set by the energy minimization of the previous section (i.e., eq. 6), the pairwise energy is minimized at every domain spacing,  $d$ , by  $\partial G/\partial\phi = 0$  to find the domain tilt angle that minimizes the deformation energy (see *SI Appendix* for details). This results in 2 qualitatively distinct scenarios: 2 domains whose curvatures have the same sign repel each other, whereas 2 domains whose curvatures have the opposite sign attract each other. Scaling arguments can be used to show that the strength of interaction between 2 dimpled domains increases approximately linearly with their area so long as they are both larger than some critical area (see *SI Appendix* for details). Mathematically, the assumption of rigidly rotating dimpled domains is identical to a previous 2D model of bending-mediated interactions between intramembrane proteins, represented by rigid conical inclusions (51).

Independent of the effects of spontaneous curvature, slight osmolar imbalances and constriction due to the lipid phase boundaries create small pressure gradients across the membrane that tend to orient all dimples on a vesicle in the same direction, resulting in net repulsive interactions between all domains. Transitions between “upward” and “downward” dimples are infrequent due to a large energy barrier. In the simplest case, where the

domains are the same size, the tilt angle  $\phi$  monotonically increases as 2 domains get closer,  $\phi(d) \approx -\epsilon e^{-d}$ . Likewise, the interaction energy increases monotonically with decreasing domain separation,  $V_{\text{int}}(d) \approx 2\pi\kappa_b\epsilon^2\rho_0^2e^{-d}$ . To quantitatively compare our interaction model with experiment, we analyzed the thermal motion of small domains on the surface of giant unilamellar vesicles, as described in *Materials and Methods*. For direct comparison, we fit both the 1D model outlined here and the 2D inclusion model (51) to the measured potential of mean force between domains, as shown in Fig. 4. The 2 models are experimentally indistinguishable, though with a slightly different elastic decay length.

In these experiments, membrane tension was regulated by balancing the internal and external osmolarity, giving us coarse

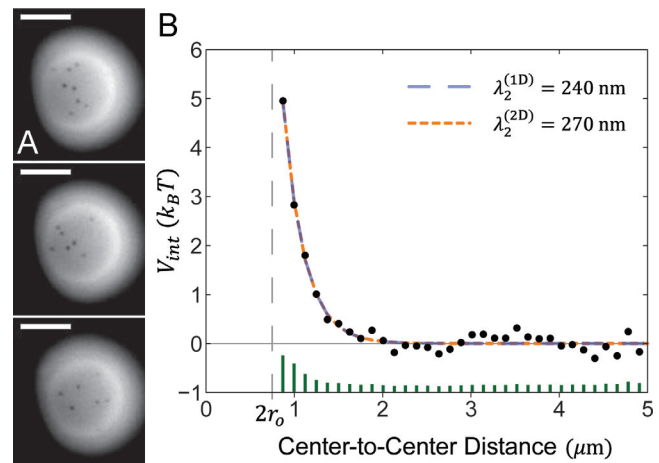


**Fig. 4.** Measuring domain interactions on the surface of a vesicle. (A) Three images of dilute interacting domains on the surface of the same vesicle. (B) The repulsive interaction potential ( $V_{\text{int}}$ ) between domains on the surface of the same vesicle as A. The energy is measured in  $k_B T$ , and distance is domain center-to-center. The blue dashed line is a fit to the 1D interaction model in this article,  $V_{\text{int}}(r) = a_1 e^{-r/\lambda_2^{(1D)}} + a_2$ , with elastic decay length  $\lambda_2^{(1D)} = 240 \text{ nm}$ . The orange dashed line is a fit to the model,  $V_{\text{int}}(r) = 2\pi\kappa_b[(a_1 a_2)^2 K_0(r/\lambda_2^{(2D)}) + a_2^2 a_3^4 K_2^2(r/\lambda_2^{(2D)})] + a_4$ , with elastic decay length  $\lambda_2^{(2D)} = 270 \text{ nm}$ , based on the theory of Weikl et al. (51). Both elastic decay lengths indicate a membrane tension of  $\sim 4 \times 10^{-4} k_B T/\text{nm}^2$ . Errors bars are shown in green on the x-axis.

control over the elastic decay length  $\lambda_2$ . Through time, the distance between every domain pair was measured, and the net results were used to construct a histogram of center-to-center distance probability, the natural logarithm of which is the potential of mean force, as shown in Fig. 4B. We selected vesicles that had a low density of approximately equal-sized domains, and thus, generally, the interactions were described by a repulsive pairwise potential. Though areal density of domains and generic data quality varied in our experiments (see *SI Appendix*), all datasets exhibit the repulsive core of the elastic interaction. Multibody interactions occur, though infrequently; their effect can be seen as a small variation in the baseline of Fig. 4B, which is not captured by the pairwise interaction model. At high membrane tension, when we would not expect dimpled domains, we qualitatively verified that domains coalesce in a rapid manner as compared with our low-tension experiments (data not shown). Other recent experiments have also observed repulsive interactions and a correspondingly slower rate of coalescence between domains on low membrane tension vesicles, and a marked increase in coalescence kinetics on the surface of taut vesicles (43).

Our measurement of the pairwise potential allows us to estimate elastic properties of the membrane. The elastic decay length was fit to the 1D and 2D interaction models described above and found to be  $\lambda_2^{(1D)} \approx 240$  nm and  $\lambda_2^{(2D)} \approx 270$  nm, respectively. Taken with a nominal bending modulus of  $25 k_B T$ , we estimate the membrane tension to be  $\approx 4 \times 10^{-4} k_B T / \text{nm}^2$ . From the images, we measure the size of the domains at  $r_o \approx 350 - 400$  nm, and hence  $\rho_o \approx 1.5$ . We estimate the line tension,  $\gamma$ , using Eq. 8, based on the fact that the domains are dimpled, and find a lower bound of  $\gamma \approx 0.49 k_B T / \text{nm}$  ( $1 k_B T / \text{nm} = 4.14 \text{ pN}$ ). This is in good agreement with theoretical estimates and values determined from experiment as discussed above. Finally, viewing the repulsive core of the interaction as an effective activation barrier to coalescence, a simple Arrhenius argument suggests a decrease in coalescence kinetics by 2–3 orders of magnitude. Indeed, such a slowing of coalescence was recently observed in a similar model membrane system (43).

## Discussion

Our experiments on the surface of GUVs have 3 potentially confounding effects, all due to the spherical curvature of the vesicle. First, the surface metric is not entirely flat with respect to the image plane. Thus, measurements of distance are underestimated the farther they are made from the projected vesicle center. This problem is ameliorated by concentrating on domains that are at the bottom (or top) of the vesicle where the surface is nearly flat and demanding that our tracking software exclude domains that are out of focus; see *SI Appendix* for a more detailed explanation. The second potential complication is that we use a flat 2D coordinate system for our theoretical analysis; however, domains reside on a curved surface. Given that the domain deformation, and hence energy density, decays exponentially with  $\lambda_2$ , as long as  $\lambda_2$  is small with respect to the vesicle radius, the energetics that govern morphology converge on an essentially flat surface metric. The final complication is that the circular area of focus creates a fictitious confining potential for the domains, such that the effective measured potential of mean force is the sum of the elastic pairwise potential and a fictitious potential,  $V_{\text{eff}} = V_{\text{int}} + V_{\text{fict}}$ . The fictitious potential is removed by simulating noninteracting particles in a circle the same size as the radius of focus (see *SI Appendix* for details).

The constant tension ensemble used in our theoretical analysis has an experimental range of validity, determined by the excess area available on a thermally fluctuating membrane with conserved volume and total surface area  $A_o$  (i.e., a vesicle). In the limit where the morphological transitions use only a small portion ( $\Delta A$ ) of this excess area, defined by  $k_B T / 8\pi\kappa_b \gg \Delta A / A_o$ , the tension is constant. Outside this regime, the tension rises exponentially with

reduction in excess area, tending to stabilize dimples from fully budding (see *SI Appendix* for details).

In addition to the elastic mechanism of interaction, described herein, there may be other organizing forces at work in a phase-separated membrane, for instance, those of elastic (28) or entropic (52, 53) origin. However, the putative length scale over which these effects compete with thermal fluctuations (on the order of tens of nanometers) is not accessible to the spatial and temporal resolution of our experiments. Electrostatics may also be at work, in the form of dipole–dipole repulsion due to the net difference in dipole density between the 2 phases (54–56), although to first order, symmetry suggests there is a net zero dipole moment per unit volume of bilayer (57). In our experimental system, the modulator of repulsive interactions is membrane morphology (i.e., domain dimpling); if other interactions were a major repulsive effect, we would not expect such forces to depend markedly on large-scale membrane morphology.

## Conclusion

We have shown that lipid domains are subject to a morphological dimpling transition that depends on the bilayer elastic properties and domain size. Dimpling allows 2 domains in proximity to repulsively interact due to the deformation in the surrounding membrane. Our model makes 2 key predictions: (i) at zero spontaneous curvature, the domain size distribution reaches a critical point where coalescence is arrested by repulsive interactions (43) and (ii) domains with finite spontaneous curvature are always subject to interaction and hence should always coalesce at a rate slower than the diffusion-limited rate (35). Additionally, the strength of elastic interactions is augmented by increasing line tension or domain area, with an approximately linear scaling. We proposed a simple 1D model of an elastic interaction that mediates dimpled-domain repulsion and then used a standard ternary membrane system to verify the existence of dimpled domains and their subsequent repulsive interaction. Our model offers a mechanism that works against diffusion-driven coalescence, to maintain small lipid domains over time.

## Materials and Methods

GUVs were prepared from a mixture of DOPC (1,2-dioleoyl-sn-glycero-3-phosphocholine), DPPC (1,2-dipalmitoyl-sn-glycero-3-phosphocholine) and cholesterol (Avanti Polar Lipids, Inc.) (25:55:20/molar) that exhibits liquid–liquid phase coexistence (3). Fluorescence contrast between the 2 lipid phases is provided by the rhodamine head-group-labeled lipids: DOPE (1,2-dioleoyl-sn-glycero-3-phosphoethanolamine-N-(lissamine rhodamine B sulfonyl)) or DPPE (1,2-dipalmitoyl-sn-glycero-3-phosphoethanolamine-N-(lissamine rhodamine B sulfonyl)), at a molar fraction of  $\approx 0.005$ . The leaflet compositions are presumed symmetric, and, hence,  $v_o = 0$ .

GUVs were formed via electroformation (3, 58). Briefly, 3–4  $\mu\text{g}$  of lipid in chloroform were deposited on an indium–tin oxide-coated slide and dessicated for  $\approx 2$  h to remove excess solvent. The film was then hydrated with a 100 mM sucrose solution and heated to  $\approx 50^\circ\text{C}$  to be above the miscibility transition temperature. An alternating electric field was applied; 10 Hz for 120 m, 2 Hz for 50 m, at  $\approx 500$  Volts/m over  $\approx 2$  mm. Low membrane tensions were achieved by careful osmolar balancing with sucrose ( $\approx 100$  mM) inside the vesicles, and glucose ( $\approx 100$ –108 mM) outside.

Domains were induced by a temperature quench (see *SI Appendix*) and imaged by using standard TRITC epifluorescence microscopy at  $80\times$  magnification with a cooled ( $-30^\circ\text{C}$ ) CCD camera ( $6.7 \times 6.7 \mu\text{m}^2$  per pixel, 20 MHz digitization; Roper Scientific). Images were taken from the top or bottom of a GUV where the surface metric is approximately flat (see *SI Appendix*). Datasets contained  $\approx 500$ –1,500 frames collected at 10–20 Hz with a varying number of domains (usually 5–10). The frame rate was chosen to minimize exposure-time blurring of the domains while allowing sufficiently large diffusive domain motion. Software was written to track the position of each well-resolved domain and calculate the radial distribution function. The raw radial distribution function was corrected for the fictitious confining potential of the circular geometry (see *SI Appendix*). In the dilute interaction limit, pairwise interactions dominate, and the negative natural logarithm of the radial distribution function is the interaction potential (potential of mean force) plus a constant, as shown in Fig. 4B.

**Note Added in Proof.** Just recently, another group (59) has independently come to similar conclusions about the presence of elastically mediated interactions among dimpled domains, specifically commenting on their tendency to order domains.

**ACKNOWLEDGMENTS.** We thank Patricia Bassereau, Evan Evans, Ben Freund, Kerwyn Huang, Greg Huber, Sarah Keller, and Udo Seifert for stimulating

discussion and comments on the manuscript and Jenny Hsiao for help with experiments. T.U. and R.P. acknowledge the support of National Science Foundation (NSF) Award CMS-0301657, NSF Award ACI-0204932, Nanoscale Interdisciplinary Research Teams Award CMS-0404031, and the National Institutes of Health Director's Pioneer Award, and National Institutes of Health Award RO1 GM084211. W.S.K. acknowledges support from NSF CAREER Award CMMI-0748034.

1. Singer SJ, Nicolson GL (1972) The fluid mosaic model of the structure of cell membranes. *Science* 175:720–731.
2. Garcia-Saez AJ, Chiantia A, Schwille P (2007) Effect of line tension on the lateral organization of lipid membranes. *J Biol Chem* 282:33537–33544.
3. Veatch SL, Keller SL (2003) Separation of liquid phases in giant vesicles of ternary mixtures of phospholipids and cholesterol. *Biophys J* 85:3074–3083.
4. Bacic K, Schwille P, Kurzchalia T (2005) Sterol structure determines the separation of phases and the curvature of the liquid-ordered phase in model membranes. *Proc Natl Acad Sci USA* 102:3272–3277.
5. Baumgart T, Hess ST, Webb WW (2003) Imaging coexisting fluid domains in biomembrane models coupling curvature and line tension. *Nature* 425:821–824.
6. Simons K, Ikonen E (1997) Functional rafts in cell membranes. *Nature* 387:569–572.
7. Sens P, Turner MS (2006) Budded membrane microdomains as tension regulators. *Phys Rev E* 73:031918.
8. Raucher D, Sheetz MP (1999) Characteristics of a membrane reservoir buffering membrane tension. *Biophys J* 77:1992–2002.
9. Simons K, Vaz WL (2004) Model systems, lipid rafts, and cell membranes. *Annu Rev Biophys Biomol Struct* 33:269–295.
10. Schlegel A, et al. (1998) Crowded little caves: Structure and function of caveolae. *Cell Signal* 10:457–463.
11. van Meer G, Sprong H (2004) Membrane lipids and vesicular traffic. *Curr Opin Cell Biol* 16:373–378.
12. Chazal N, Gerlier D (2003) Virus entry, assembly, budding, and membrane rafts. *Microbiol Mol Biol Rev* 67:226–237.
13. Mayor S, Rao M (2004) Rafts: Scale-dependent, active lipid organization at the cell surface. *Traffic* 5:231–240.
14. Dietrich C, et al. (2001) Lipid rafts reconstituted in model membranes. *Biophys J* 80:1417–1428.
15. Park H, et al. (1998) Plasma membrane cholesterol is a key molecule in shear stress-dependent activation of extracellular signal-regulated kinase. *J Biol Chem* 273:32304–32311.
16. Helms JB, Zurzolo C (2004) Lipids as targeting signals: lipid rafts and intracellular trafficking. *Traffic* 5:247–254.
17. Lucero HA, Robbins PW (2004) Lipid rafts-protein association and the regulation of protein activity. *Arch Biochem Biophys* 426:208–224.
18. Gaus K, et al. (2003) Visualizing lipid structure and raft domains in living cells with two-photon microscopy. *Proc Natl Acad Sci USA* 100:15554–15559.
19. Turner MS, Sens P, Socci ND (2005) Nonequilibrium raftlike membrane domains under continuous recycling. *Phys Rev Lett* 95:168301.
20. Gheber LA, Edidin M (1999) A model for membrane patchiness: Lateral diffusion in the presence of barriers and vesicle traffic. *Biophys J* 77:3163–3175.
21. Dietrich C, Yang B, Fujiwara T, Kusumi A, Jacobson K (2002) Relationship of lipid rafts to transient confinement zones detected by single particle tracking. *Biophys J* 82:274–284.
22. Murase K, et al. (2004) Ultrafine membrane compartments for molecular diffusion as revealed by single molecule techniques. *Biophys J* 86:4075–4093.
23. Bray AJ (2002) Theory of phase-ordering kinetics. *Adv Phys* 51:481–587.
24. Sagui S, Desai RC (1995) Ostwald ripening in systems with competing interactions. *Phys Rev Lett* 74:1119–1122.
25. Laradji M, Sunil Kumar PB (2004) Dynamics of domain growth in self-assembled fluid vesicles. *Phys Rev Lett* 93:198105.
26. Seul M, Andelman D (1995) Domain shapes and patterns: The phenomenology of modulated phases. *Science* 267:476–483.
27. Sagui C, Desai RC (1994) Kinetics of phase separation in two-dimensional systems with competing interactions. *Phys Rev E* 49:2225–2244.
28. Kuzmin PI, Akimov SA, Chizmadzhev YA, Zimmerberg J, Cohen FS (2005) Line tension and interaction energies of membrane rafts calculated from lipid splay and tilt. *Biophys J* 88:1120–1133.
29. Seul M, Morgan NY, Sire C (1994) Domain coarsening in a two-dimensional binary mixture: Growth dynamics and spatial correlations. *Phys Rev Lett* 73:2284–2287.
30. Foret L (2005) A simple mechanism of raft formation in two-component fluid membranes. *Europhys Lett* 71:508–514.
31. Harden JL, Mackintosh FC, Olmsted PD (2005) Budding and domain shape transformations in mixed lipid films and bilayer membranes. *Phys Rev E* 72:011903.
32. Taniguchi T (1996) Shape deformation and phase separation dynamics of two-component vesicles. *Phys Rev Lett* 76:4444–4447.
33. Gozdz WT, Gompper G (2001) Shape transformations of two-component membranes under weak tension. *Europhys Lett* 55:587–593.
34. Reigada R, Buceta J, Lindenberg K (2005) Nonequilibrium patterns and shape fluctuations in reactive membranes. *Phys Rev E* 71:051906.
35. Laradji M, Kumar PB (2006) Anomalously slow domain growth in fluid membranes with asymmetric transbilayer lipid distribution. *Phys Rev E* 73:040901.
36. Freund LB, Suresh S (2004) *Thin Film Materials: Stress, Defect Formation and Surface Evolution* (Cambridge Univ Press, Cambridge, UK).
37. Boal D (2002) *Mechanics of the Cell* (Cambridge Univ Press, Cambridge UK), 1st Ed.
38. Wiggins P, Phillips R (2005) Membrane-protein interactions in mechanosensitive channels. *Biophys J* 88:880–902.
39. Helfrich W (1973) Elastic properties of lipid bilayers: theory and possible experiments. *Z Naturforsch C* 28:693–703.
40. Parthasarathy R, Yu CH, Groves JT (2006) Curvature-modulated phase separation in lipid bilayer membranes. *Langmuir* 22:5095–5099.
41. Farsad K, De Camilli P (2003) Mechanisms of membrane deformation. *Curr Opin Cell Biol* 15:372–381.
42. Rawicz W, Olbrich KC, McIntosh T, Needham D, Evans E (2000) Effect of chain length and unsaturation on elasticity of lipid bilayers. *Biophys J* 79:328–339.
43. Yanagisawa M, Imai M, Masui T, Komura S, Ohta T (2007) Growth dynamics of domains in ternary fluid vesicles. *Biophys J* 92:115–125.
44. Lipowsky R (1992) Budding of membranes induced by intramembrane domains. *J Phys II France* 2:1825–1840.
45. Tian A, Johnson C, Wang W, Baumgart T (2007) Line tension at fluid membrane domain boundaries measured by micropipette aspiration. *Phys Rev Lett* 98:208102.
46. Simons K, Ikonen E (2000) How cells handle cholesterol. *Science* 290:1721–1726.
47. Wang W, Yang L, Huang HW (2007) Evidence of cholesterol accumulated in high curvature regions: Implication to the curvature elastic energy for lipid mixtures. *Biophys J* 92:2819–2830.
48. McMahon HT, Gallop JT (2005) Membrane curvature and mechanisms of dynamic cell membrane remodelling. *Nature* 438:590–596.
49. Huang KC, Mukhopadhyay R, Wingreen NS (2006) A curvature-mediated mechanism for localization of lipids to bacterial poles. *PLoS Comput Biol* 2:e151.
50. Hansen SH, Sandvig K, van Deurs B (1992) Internalization efficiency of the transferrin receptor. *Exp Cell Res* 199:19–28.
51. Weikl TR, Kozlov MM, Helfrich W (1998) Interaction of conical membrane inclusions: Effect of lateral tension. *Phys Rev E* 57:6988–6995.
52. Dean DS, Manghi M (2006) Fluctuation-induced interactions between domains in membranes. *Phys Rev E* 74:021916.
53. Goulian M, Pincus P, Bruinsma R (1993) Long-range forces in heterogeneous fluid membranes. *Europhys Lett* 22:145–150.
54. Andelman D, Brochard F, Joanny JF (1987) Phase transitions in Langmuir monolayers of polar molecules. *J Chem Phys* 86:3673–3681.
55. McConnell HM (1989) Theory of hexagonal and stripe phases in monolayers. *Proc Natl Acad Sci USA* 86:3452–3455.
56. Liu J, Qi S, Groves JT, Chakraborty AK (2005) Phase segregation on different length scales in a model cell membrane system. *J Phys Chem B* 109:19960–19969.
57. Wohlfert J, Edholm O (2004) The range and shielding of dipole–dipole interactions in phospholipid bilayers. *Biophys J* 87:2433–2445.
58. Angelova ME, Soleau S, Meleard P, Faucon JF, Bothorel P (1992) Preparation of giant vesicles by external AC electric fields: kinetics and applications. *Prog Colloid Polymer Sci* 89:127–131.
59. Semrau S, Idema T, Schmidt T, Storm C (2009) Membrane-mediated interactions measured using membrane domains. *Biophys J* 96:4906–4915.

Supplementary Information for:  
'Morphology and Interaction between Lipid Domains'

Tristan S. Ursell, William S. Klug, and Rob Phillips

May 19, 2009

## Contents

<b>1</b>	<b>Introduction to the Theory of Lipid Domain Morphology</b>	<b>2</b>
1.1	Calculating Membrane Curvature and Area . . . . .	2
1.2	Conservation of Domain Area . . . . .	4
1.3	The Small Gradient Limit . . . . .	5
1.4	Gaussian Curvature . . . . .	10
1.5	Equilibrium Domain Shapes . . . . .	12
1.6	Scaling and the Critical Exponent . . . . .	13
1.7	Divergence Theorem Solution for the Deformation Energy . . . . .	15
<b>2</b>	<b>Vesicle Tension and Entropy</b>	<b>17</b>
2.1	Constructing a Thermal Ensemble . . . . .	17
2.2	The Equation of State . . . . .	18
<b>3</b>	<b>The 1D Interaction Potential</b>	<b>26</b>
3.1	Interactions of Asymmetric Domains . . . . .	27
3.2	Effects of Domain Size Asymmetry . . . . .	30
3.2.1	Corrections from Size Asymmetry . . . . .	31
<b>4</b>	<b>Coarse Control of Membrane Tension and Inducing Phase Separation</b>	<b>34</b>
<b>5</b>	<b>Error Introduced by the Curved Vesicle Surface</b>	<b>35</b>
<b>6</b>	<b><i>In vitro</i> Selection and Representative Data</b>	<b>37</b>
<b>7</b>	<b>Domain Tracking and Data Analysis</b>	<b>40</b>
7.1	The Fictitious Confining Potential . . . . .	46
7.1.1	The Geometric Derivation . . . . .	48

# 1 Introduction to the Theory of Lipid Domain Morphology

Our goal in the following few sections is to add detail to calculations already performed or alluded to in the text. We begin by building up the linearized Helfrich functional and examining how spontaneous curvature, line tension and membrane tension affect membrane morphology [1, 2, 3].

## 1.1 Calculating Membrane Curvature and Area

In general, a thin elastic sheet can be described by a surface,  $\mathcal{S}(u, v)$ , embedded in  $\mathbb{R}^3$  and written as a function of the parametric variables  $(u, v)$ . At each point on this surface, one can calculate the curvature tensor and pointwise contribution to the total area. As we will show in the next few sections, the curvature tensor is used to calculate contributions to the elastic energy from two different modes of bending and the area is used to couple membrane tension, via a particular ensemble, to membrane energetics.

Our first simplifying assumption is that there is some one-to-one height function (*i.e.* no folds) that describes the membrane midplane,  $h(\mathbf{r})$ , often referred to as a *Monge* representation. Using this representation, the exact area of the membrane is a simple, though non-linear, function of  $h$ , given by

$$\mathcal{A} = \int_{\mathcal{S}} \sqrt{1 + (\nabla h)^2} d^2\mathbf{r}. \quad (1)$$

In comparison to a completely flat membrane, the increase in actual area due to deformation is given by

$$\Delta\mathcal{A} = \int_{\mathcal{S}} (\sqrt{1 + (\nabla h)^2} - 1) d^2\mathbf{r}, \quad (2)$$

which couples to the lateral membrane tension  $\tau$  by  $G_{\text{tens}} = \tau\Delta\mathcal{A}$  in a constant tension ensemble<sup>1</sup>. In the limit where gradients are small,  $|\nabla h| \ll 1$ , this simplifies to

$$\Delta\mathcal{A} = \frac{1}{2} \int_{\mathcal{S}} (\nabla h)^2 d^2\mathbf{r}. \quad (3)$$

At every point on the surface  $\mathcal{S}$ , the matrix of second partial derivatives defines the curvature tensor  $\mathcal{C}$ , whose eigenvalues are the principal curvatures of the surface at that point, and whose eigenvectors specify the directions of those principal curvatures on the surface, as shown in Fig. 1b. Any elastic energy formulation we construct from the curvature tensor should be invariant under rotations, reflections and translations and therefore can be written as a function of the invariants of the curvature tensor, namely the trace, which is the sum of the principal curvatures, and the determinant, which is the product of the principal curvatures. To lowest order, these symmetries dictate that the energy should be linear in the determinant and quadratic in the trace. The determinant's contribution is usually called the Gaussian curvature and will be addressed in subsection 1.4. One half the sum of the principal curvatures is called the *mean curvature*, denoted by  $H$ , and contributes energy of the form  $H^2$ . An intuitively pleasing formulation of the mean curvature is the divergence of the unit normal vector field of the surface [4], as shown in Fig. 1a, that is

$$H(\mathbf{r}) = \frac{1}{2} \nabla \cdot \hat{n}(\mathbf{r}), \quad (4)$$

---

<sup>1</sup>See section 2 for an in depth discussion of a variable tension ensemble, applicable to thermal environments.

from which the mean curvature energy is calculated as

$$G_{\text{bend}} = 2\kappa_b \int_{\mathcal{S}} H^2 \sqrt{g} d^2\mathbf{r}, \quad (5)$$

where  $g = 1 + (\nabla h)^2$  is the surface metric in the Monge representation. The surface  $h(x, y)$  can be written as an implicit function  $F(x, y, z)$ , by

$$h(x, y) = z \rightarrow F(x, y, z) = h(x, y) - z = 0, \quad (6)$$

from which the unit normal vector is given by

$$\hat{n} = \frac{\nabla F}{\sqrt{(\nabla F)^2}}. \quad (7)$$

On the surface defined by  $h$ , the unit normal vector field is the gradient normalized by the size of the small piece of area associated with the unit vector at the point  $\mathbf{r}$ , namely

$$\hat{n} = \frac{(\partial_x h, \partial_y h, -1)}{\sqrt{1 + (\nabla h)^2}}. \quad (8)$$

Then the mean curvature becomes a straight-forward, though non-linear, function of  $h$ , given by

$$H = \frac{1}{2} \nabla \cdot \left( \frac{\nabla F}{\sqrt{1 + (\nabla h)^2}} \right). \quad (9)$$

In situations where the height function is azimuthally symmetric, this can be expanded to

$$H = \frac{1}{2r} \frac{\partial}{\partial r} \left[ \frac{r \frac{\partial h}{\partial r}}{\sqrt{1 + (\frac{\partial h}{\partial r})^2}} \right]. \quad (10)$$

Application of the small gradient approximation yields a linearized curvature of the well-known form

$$H \simeq \frac{1}{2} \nabla^2 h, \quad (11)$$

with the linearized metric  $g \simeq 1$ , such that the integral of the mean curvature elastic energy over the surface is

$$G_{\text{bend}} = 2\kappa_b \int_{\mathcal{S}} H^2 \sqrt{g} d^2\mathbf{r} \simeq \frac{\kappa_b}{2} \int_{\mathcal{S}} (\nabla^2 h)^2 d^2\mathbf{r}. \quad (12)$$

With azimuthal symmetry this simplifies further to

$$G_{\text{bend}} = \pi \kappa_b \int_{\mathcal{S}} (\nabla^2 h)^2 r dr, \quad (13)$$

and this contribution can now be combined into a linear elastic picture of a stiff membrane under lateral tension.

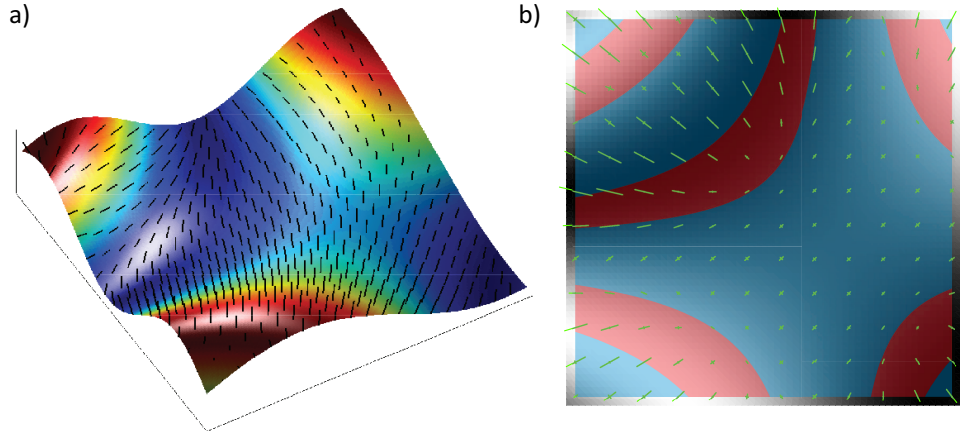


Figure 1: Curvature on a Monge surface. a) Plot showing a Monge surface with its corresponding unit normal vector field. b) The same surface, now laid flat and shown in grayscale. The small green lines indicate the directions of the principal curvatures, while their lengths indicate the magnitude of the principal curvatures at those points. Zones whose principal curvatures have the same sign are colored in red (positive Gaussian curvature), while zones whose principal curvatures have opposite signs are colored in blue (negative Gaussian curvature).

## 1.2 Conservation of Domain Area

Before constructing the full elastic model of a deformed lipid domain and its surrounding membrane, it behooves us to constrain the class of elastic models by discussing certain properties of the domain. In particular, if changes in domain morphology were accompanied by significant changes in domain area, this would require a more complex elastic model. The point of this section is to decisively show that the relevant elastic model conserves domain area during any morphological transition, as posited in the text, though strictly speaking, this need not be true. For instance, if the material parameters were such that the stretch modulus of the domain was very low, while the line tension around the domain was very high, we would expect a large change in domain area. However, as we demonstrate in this section, the material properties of a bilayer favor the conserved area picture, and hence the use of a Lagrange multiplier formulation to impose this area constraint. To see this explicitly, we estimate the area change induced by the line tension for representative values of the relevant bilayer properties.

To be rigorous about this statement, we note that the membrane tension ( $\tau$ ) is linearly related to the areal strain ( $\phi$ ) by the area stretch modulus  $K_A$  [5],

$$\tau = K_A \phi, \quad (14)$$

where

$$\phi = \frac{\mathcal{A} - \mathcal{A}_o}{\mathcal{A}_o} \quad (15)$$

and  $\mathcal{A}_o$  is the domain area at zero tension. Thus a small change in domain area costs free energy

$$dG_{\text{area}} = \tau(\phi)d\mathcal{A} = \mathcal{A}_o K_A \phi d\phi, \quad (16)$$

and hence upon integration we find the elastic stretch energy of a domain is

$$G_{\text{area}} = \mathcal{A}_o \frac{K_A}{2} \phi^2. \quad (17)$$

For simplicity, let us consider the case where the domain is flat and hence the membrane tension and phase boundary line tension directly compete with each other - this is also the scenario where we would expect the largest potential area change. In this case, the phase boundary is characterized by the circumference

$$\ell = 2\pi r_o = 2\pi \sqrt{\frac{A_o(1+\phi)}{\pi}} \quad (18)$$

where  $r_o$  is the projected radius of the domain. This contributes energy of the form

$$G_{\text{line}} = \gamma\ell, \quad (19)$$

where  $\gamma$  is the line tension and we assume  $\partial\gamma/\partial\phi = 0$ . The combined energy,  $G_{\text{area}} + G_{\text{line}}$ , can be used to solve for the equilibrium value of  $\phi$  by evaluating

$$\frac{\partial}{\partial\phi}(G_{\text{area}} + G_{\text{line}}) = \omega^2\phi^2(1+\phi) - \pi = 0, \quad (20)$$

where we introduce the dimensionless parameter  $\omega = K_A\sqrt{A_o}/\gamma$ . Using the high estimate of  $\gamma = 1.0 \text{ } k_B T/\text{nm}$  and low estimate of  $K_A = 50 \text{ } k_B T/\text{nm}^2$  [5], corresponds to  $\omega \gg 1$  for all reasonable domain areas (*i.e.* one lipid or more), and hence the areal strain is

$$\phi \simeq \frac{\sqrt{\pi}}{\omega}, \quad (21)$$

resulting in a fractional area change of less than 1% for all reasonable domain areas - thus we work within an approximation in which the domain area is conserved.

### 1.3 The Small Gradient Limit

Using a small gradient approximation is not the most general model for the membrane surface, but it allows us to state our results analytically, and couches domain dimpling as a linearized buckling problem. The line tension at the phase boundary of a domain favors a circular geometry, and hence our model utilizes polar coordinates. Employing a small gradient approximation, valid when  $|\nabla h| \ll 1$ , yields a quadratic approximation to the functional which can be solved analytically [4, 6, 7]. With no other approximations, the mean curvature and constant membrane tension give rise to an energy functional of the form

$$G_{\text{el}} = G_{\text{tens}} + G_{\text{bend}} = \frac{1}{2} \int_S \left( \tau(\nabla h)^2 + \kappa_b (\nabla^2 h - c_o)^2 \right) d^2\mathbf{r} \quad (22)$$

where  $S$  is the projected surface of integration,  $\tau$  is the applied membrane tension,  $\kappa_b$  is the mean curvature bending modulus, and  $c_o$  is the spontaneous curvature of the membrane comprising the domain.

However, this only forms part of the complete free energy of a dimpled membrane. In addition to the elastic components, we must conserve area of the domain through the use of a Lagrange multiplier. Further, to have any interesting behavior at all, we impose a penalty at the phase boundary through the use of a line tension, as we did in the estimate of the previous section. Our strategy is to delineate all of the energy sources, posit a set of length-scales that clearly elucidate the important parameters, and solve for the constrained minima in free energy.

To be clear about all of the sources of energy they can be listed as follows: the elastic free energy in the domain region (region 1) is given by

$$G_{\text{el}}^{(1)} = \pi \int_0^{r_o} [\tau(\nabla h_1)^2 + \kappa_b^{(1)}(\nabla^2 h_1 - c_o)^2] r dr \quad (23)$$

while the elastic energy in outer region (region 2) is given by

$$G_{\text{el}}^{(2)} = \pi \int_{r_o}^{\infty} [\tau(\nabla h_2)^2 + \kappa_b^{(2)}(\nabla^2 h_2)^2] r dr, \quad (24)$$

where  $r_o$  is the projected domain radius. The subscripts on  $h$  and superscripts on  $\kappa_b$  refer to the region of interest. The phase boundary is simply penalized by its length, hence the energy from line tension is given by

$$G_{\text{line}} = 2\pi r_o \gamma, \quad (25)$$

where  $\gamma$  is the energy per unit length along the phase boundary. Finally, the area constraint is imposed through the use of a Lagrange multiplier,  $\tau_o$ , written as

$$G_{\text{area}} = \tau_o \left( 2\pi \int_0^{r_o} \left( 1 + \frac{1}{2}(\nabla h_1)^2 \right) r dr - \mathcal{A} \right). \quad (26)$$

Our first step is to rearrange the constraint equation to construct what can be thought of as the ‘effective’ tension in the domain  $\tau_1 = \tau + \tau_o$ . In particular, we can absorb part of  $G_{\text{area}}$  into  $G_{\text{el}}^{(1)}$ , resulting in

$$G_{\text{el}}^{(1)} = \pi \int_0^{r_o} [\tau_1(\nabla h_1)^2 + \kappa_b^{(1)}(\nabla^2 h_1 - c_o)^2] r dr \quad (27)$$

and

$$G_{\text{area}} = \tau_o (\pi r_o^2 - \mathcal{A}). \quad (28)$$

Our next step is to non-dimensionalize the free energy, with the understanding that if we are to see dimpling at all, the membrane tension in the domain region must be compressive, in other words, the sum of the external membrane tension and the membrane tension generated by the line tension must be negative. Mathematically this is stated simply as  $\tau_1 < 0$ ; this will turn out to be an important fact when choosing admissible solutions to the Euler-Lagrange equations. To non-dimensionalize the free energy, we first note the two length scales in the problem are

$$\lambda_1 = \sqrt{\frac{\kappa_b^{(1)}}{\tau_1}} \quad \text{and} \quad \lambda_2 = \sqrt{\frac{\kappa_b^{(2)}}{\tau}}, \quad (29)$$

and we use these to define the constants

$$\beta = i \frac{\lambda_2}{\lambda_1} \quad \text{and} \quad \sigma = \frac{\kappa_b^{(1)}}{\kappa_b^{(2)}}. \quad (30)$$

Given our previous statements, we know that  $\lambda_2$  and  $\beta$  are both positive and real, while  $\lambda_1$  is purely imaginary with a positive coefficient when  $\tau_1 < 0$ . These length-scales give a notion of how quickly the perturbed height functions return to a flat state, where  $\lambda_2$  is a constant, but  $\lambda_1$  changes as domain area and line tension are varied. The constant length scale allows us to define the dimensionless variables

$$r = \lambda_2 \rho, \quad h_i = \lambda_2 \eta_i, \quad r_o = \lambda_2 \rho_o \quad \text{and} \quad \lambda_2 c_o = v_o. \quad (31)$$

With these definitions we can redefine the derivatives as

$$\frac{\partial}{\partial r} = \frac{1}{\lambda_2} \frac{\partial}{\partial \rho} \quad \text{and} \quad dr = \lambda_2 d\rho. \quad (32)$$

Finally, making all of these substitutions gives the elastic contributions

$$G_{\text{el}}^{(1)} = \pi \sigma \kappa_b^{(2)} \int_0^{\rho_o} [-\beta^2 (\nabla \eta_1)^2 + (\nabla^2 \eta_1 - v_o)^2] \rho d\rho \quad (33)$$

and

$$G_{\text{el}}^{(2)} = \pi \kappa_b^{(2)} \int_{\rho_o}^{\infty} [(\nabla \eta_2)^2 + (\nabla^2 \eta_2)^2] \rho d\rho, \quad (34)$$

also showing that a natural energy scale is  $\kappa_b^{(2)}$ . The line energy is then written as

$$G_{\text{line}} = 2\pi \kappa_b^{(2)} \rho_o \chi \quad (35)$$

with  $\chi = \gamma \lambda_2 / \kappa_b^{(2)}$  defined as the dimensionless line tension. This is one of two key parameters used to characterize the phase space of dimple morphology. The remaining contribution from the Lagrange multiplier is then written as

$$G_{\text{area}} = -\kappa_b^{(2)} (\sigma \beta^2 + 1) (\pi \rho_o^2 - \alpha). \quad (36)$$

where the dimensionless area,  $\alpha = \mathcal{A}/\lambda_2^2$ , is the second key parameter that characterizes the phase space of dimple morphology. The governing differential equations are distinct in each region; in region 1 the Euler-Lagrange equation is

$$\nabla^2 (\nabla^2 + \beta^2) \eta_1 = 0, \quad (37)$$

while in region 2

$$\nabla^2 (\nabla^2 - 1) \eta_2 = 0. \quad (38)$$

The solutions to these differential equations, and as we will show in section 1.7, part of the derivation of the elastic free energy, can be found by splitting these fourth order equations into two simpler, second order equations. In particular, let us view these differential equations as differential operators acting on  $\eta_i$

$$\nabla^2 (\nabla^2 + c) \eta_i = \mathcal{L} [\eta_i] = 0 \rightarrow \mathcal{L} = \nabla^2 (\nabla^2 + c), \quad (39)$$

where  $c$  is a constant. To break this down into a set of simpler equations, we call the first differential operator  $\mathcal{L}_1 = \nabla^2$  and the second  $\mathcal{L}_2 = \nabla^2 + c$ , such that  $\mathcal{L} = \mathcal{L}_1 \mathcal{L}_2$ . Each of these simpler operators defines a familiar differential equation:  $\mathcal{L}_1 [\eta_i^{(1)}] = 0$  is commonly referred to as the Laplace equation, while  $\mathcal{L}_2 [\eta_i^{(2)}] = 0$  is commonly referred to as the Helmholtz equation. The solutions to each equation are unique, as indicated by the superscripts. In polar coordinates, the Laplace equation yields a solution that is the sum of a constant and a natural logarithm, and the Helmholtz equation yields a sum of Bessel functions whose ‘kind’ depend on the sign of the constant  $c$ . For the moment, let us assume that the full solution to the fourth order equation is the addition of the solutions from each of these second order equations, that is

$$\eta_i = \eta_i^{(1)} + \eta_i^{(2)}, \quad (40)$$

and see what that implies for the operators  $\mathcal{L}_i$ . The fourth order equation would then be written as

$$\mathcal{L}[\eta_i] = \mathcal{L}_1 \mathcal{L}_2 \left[ \eta_i^{(1)} + \eta_i^{(2)} \right] = 0, \quad (41)$$

and since the operators  $\mathcal{L}_i$  are linear, this can be written as

$$\mathcal{L}_1 \mathcal{L}_2 \left[ \eta_i^{(1)} \right] + \mathcal{L}_1 \mathcal{L}_2 \left[ \eta_i^{(2)} \right] = 0. \quad (42)$$

With the trivial fact that  $\mathcal{L}_i[0] = 0$ , and recalling that the solutions to each second order equation are unique, this can be simplified to

$$\underbrace{\mathcal{L}_1 \mathcal{L}_2 \left[ \eta_i^{(1)} \right]}_{\neq 0} + \underbrace{\mathcal{L}_1 \mathcal{L}_2 \left[ \eta_i^{(2)} \right]}_{=0} = \mathcal{L}_1 \mathcal{L}_2 \left[ \eta_i^{(1)} \right] = 0. \quad (43)$$

If the differential operators commute, that is if  $[\mathcal{L}_1, \mathcal{L}_2] = 0$ , this can be rearranged to

$$\underbrace{\mathcal{L}_1 \mathcal{L}_2 \left[ \eta_i^{(1)} \right]}_{\neq 0} = \mathcal{L}_2 \underbrace{\mathcal{L}_1 \left[ \eta_i^{(1)} \right]}_{=0} = 0. \quad (44)$$

Indeed, one can show that the operators do commute and hence the full solution to the fourth order equation is the sum of the solutions from each of the second order equations. Additionally, the knowledge that the Euler-Lagrange equations can be broken down into commuting operators will prove useful for calculating the elastic energy in section 1.7.

The solutions must meet certain physical boundary conditions; symmetry about  $r = 0$  dictates that

$$|\nabla \eta_1(0)| = |\nabla \eta_2(\infty)| = 0, \quad (45)$$

while demanding that the membrane be contiguous demands  $\eta_1(\rho_o) = \eta_2(\rho_o)$ . Finally, as we will show later, the surface cannot have ridges if the bending energy is to be finite, hence

$$|\nabla \eta_1(\rho_o)| = |\nabla \eta_2(\rho_o)| = \epsilon, \quad (46)$$

where  $\epsilon$  is the membrane slope at the phase boundary, which acts as an order parameter for the morphological phase space. Then the general solutions are

$$\eta_1(\rho) = \underbrace{a_1^{(1)} + a_2^{(1)} \ln(\rho)}_{\eta_1^{(1)}} + \underbrace{a_3^{(1)} J_0(\beta\rho) + a_4^{(1)} Y_0(\beta\rho)}_{\eta_1^{(2)}}, \quad (47)$$

and

$$\eta_2(\rho) = \underbrace{a_1^{(2)} + a_2^{(2)} \ln(\rho)}_{\eta_2^{(1)}} + \underbrace{a_3^{(2)} K_0(\rho) + a_4^{(2)} I_0(\rho)}_{\eta_2^{(2)}}, \quad (48)$$

where  $J_k$  and  $Y_k$  are  $k$ -th order Bessel functions of the first and second kind respectively, and  $I_k$  and  $K_k$  are  $k$ -th order modified Bessel functions of the first and second kind, respectively. The brackets indicate the contributions from each of the separate differential operators. The constants  $a_i^{(j)}$  are set by the boundary conditions and the physical constraint that the area change associated with morphological transitions be finite. Our stated boundary conditions demand that  $a_4^{(1)} = a_4^{(2)} = 0$ , and to keep the change in the membrane area in both regions bounded we demand  $a_2^{(1)} = a_2^{(2)} = 0$ . We have a freedom of vertical translation, which we choose

to apply to region 2, such that  $a_1^{(2)} = 0$ . Applying the slope boundary conditions at the phase boundary gives the final solutions

$$\eta_1(\rho) = -\epsilon \left[ \frac{1}{\beta} \frac{J_0(\beta\rho)}{J_1(\beta\rho_o)} - \frac{1}{\beta} \frac{J_0(\beta\rho_o)}{J_1(\beta\rho_o)} + \frac{K_0(\rho_o)}{K_1(\rho_o)} \right] \quad (49)$$

and

$$\eta_2(\rho) = -\epsilon \frac{K_0(\rho)}{K_1(\rho_o)}. \quad (50)$$

These solutions can be integrated to give closed-form expressions for the elastic energy in the two regions, as shown in section 1.7, where in region 1

$$G_{\text{el}}^{(1)} = \pi \sigma \kappa_b^{(2)} \epsilon^2 \rho_o \beta \frac{J_0(\beta\rho_o)}{J_1(\beta\rho_o)} \quad (51)$$

and in region 2

$$G_{\text{el}}^{(2)} = \pi \kappa_b^{(2)} \epsilon^2 \rho_o \frac{K_0(\rho_o)}{K_1(\rho_o)}. \quad (52)$$

The only remaining component of the free energy is the elastic contribution from spontaneous curvature in the domain. If we explicitly write the terms of the bending elastic energy from eqn. 33 we find

$$\frac{1}{2} \int (\nabla^2 \eta_1 - v_o)^2 \sqrt{g} d^2 \rho = \frac{1}{2} \int (\nabla^2 \eta_1)^2 \sqrt{g} d^2 \rho - v_o \int (\nabla^2 \eta_1) \sqrt{g} d^2 \rho + \underbrace{\frac{v_o^2}{2} \int \sqrt{g} d^2 \rho}_{\text{domain area } (\alpha)}, \quad (53)$$

where  $\sqrt{g}$  is the surface metric, equal to unity in the current approximation. Here, the term proportional to  $v_o^2$  is conventionally added to the elastic functional so that the interplay between mean curvature and spontaneous curvature is clear, however it is unimportant for determining morphology because the spontaneous curvature does not appear in the governing differential equations (eqn. 37 and 38), and since the domain area is conserved it does not affect the membrane free energy.

The domain area itself is calculated with the expression for the height field in region 1, namely eqn. 49, to give

$$\alpha = 2\pi \int_0^{\rho_o} \sqrt{1 + (\nabla \eta_1)^2} \rho d\rho \simeq 2\pi \int_0^{\rho_o} \left( 1 + \frac{(\nabla \eta_1)^2}{2} \right) \rho d\rho, \quad (54)$$

and approximated as

$$\alpha = \pi \rho_o^2 \left[ 1 + \frac{\epsilon^2}{2} \left( 1 + \left( \frac{J_0(\beta\rho_o)}{J_1(\beta\rho_o)} \right)^2 - \frac{2}{\beta\rho_o} \frac{J_0(\beta\rho_o)}{J_1(\beta\rho_o)} \right) \right]. \quad (55)$$

Let us separate out the term dealing with spontaneous curvature that *does* affect the free energy, namely

$$G_{\text{spont}} = -2\pi \sigma \kappa_b^{(2)} v_o \int_0^{\rho_o} (\nabla^2 \eta_1) \rho d\rho. \quad (56)$$

For the case in which we have azimuthal symmetry, the Laplacian can be written as  $\nabla^2 = \frac{\partial^2}{\partial \rho^2} + \frac{1}{\rho} \frac{\partial}{\partial \rho}$ , and hence we can evaluate this energy by partial integration, where

$$\int_0^{\rho_o} \frac{1}{\rho} \frac{\partial \eta}{\partial \rho} \rho d\rho = \frac{\partial \eta}{\partial \rho} \rho \Big|_0^{\rho_o} - \int_0^{\rho_o} \frac{\partial^2 \eta}{\partial \rho^2} \rho d\rho. \quad (57)$$

Upon rearranging, we see that

$$\int_0^{\rho_o} (\nabla^2 \eta) \rho d\rho = \frac{\partial \eta}{\partial \rho} \rho|_{\rho=\rho_o} \quad (58)$$

and by applying the boundary conditions, we find that the elastic energy from spontaneous curvature is

$$G_{\text{spont}} = -2\pi\sigma\kappa_b^{(2)}\epsilon\rho_o v_o. \quad (59)$$

Finally, with all contributions accounted for, we can assemble the free energy of the system, with contributions

$$G = G_{\text{el}}^{(1)} + G_{\text{el}}^{(2)} + G_{\text{line}} + G_{\text{spont}} + G_{\text{area}}, \quad (60)$$

such that the total free energy is

$$G = \pi\kappa_b\rho_o \left[ \epsilon^2 \left( \sigma\beta \frac{J_0(\beta\rho_o)}{J_1(\beta\rho_o)} + \frac{K_0(\rho_o)}{K_1(\rho_o)} \right) + 2(\chi - \epsilon\sigma v_o) \right] - \kappa_b(\sigma\beta^2 + 1)(\pi\rho_o^2 - \alpha), \quad (61)$$

with the superscript dropped,  $\kappa_b^{(2)} = \kappa_b$ . Before searching for the morphological minimizers of this equation, let us address one additional issue.

We demand that the membrane surface be free of ridges, that is, we match the slope of the membrane at the phase boundary ( $|\nabla\eta_1(\rho_o)| = |\nabla\eta_2(\rho_o)| = \epsilon$ ), because a slope mismatch would result in a divergence of the bending energy. This can be shown by direct calculation where the mismatch energy is calculated in a region,  $\rho_o \pm \delta/2$ , near the phase boundary

$$G_{\text{mismatch}} = \lim_{\delta \rightarrow 0} \pi\kappa_b \int_{\rho_o-\delta/2}^{\rho_o+\delta/2} (\nabla^2 \eta)^2 \rho d\rho = \lim_{\delta \rightarrow 0} \pi\kappa_b \int_{\rho_o-\delta/2}^{\rho_o+\delta/2} \left( \frac{\epsilon_1 - \epsilon_2}{\delta} \right)^2 \rho d\rho = \pi\kappa_b(\epsilon_1 - \epsilon_2)^2 \lim_{\delta \rightarrow 0} \frac{\rho_o}{\delta}, \quad (62)$$

where the only finite solution occurs when  $\epsilon_1 = \epsilon_2$ , that is, when the boundary slopes are matched between the domain and the surrounding membrane.

## 1.4 Gaussian Curvature

In line with our calculation of the various elastic energy terms, the following section explicitly calculates the elastic contribution from Gaussian curvature and makes an argument about its relevance to our elastic model. As discussed in the first section, the local curvature tensor is given by the matrix of partial second derivatives of the surface  $\eta$ , which in Cartesian coordinates takes the form

$$\mathcal{C} = \begin{bmatrix} \frac{\partial^2 \eta}{\partial x^2} & \frac{\partial^2 \eta}{\partial x \partial y} \\ \frac{\partial^2 \eta}{\partial y \partial x} & \frac{\partial^2 \eta}{\partial y^2} \end{bmatrix}. \quad (63)$$

The trace of this tensor is the sum of the principal curvatures, while the determinant is the Gaussian curvature [4]. Using the typical polar transformations  $\rho = \sqrt{x^2 + y^2}$  and  $\theta = \tan^{-1}(y/x)$ , the chain rule implies

$$\frac{\partial}{\partial x} = \frac{\partial \rho}{\partial x} \frac{\partial}{\partial \rho} + \frac{\partial \theta}{\partial x} \frac{\partial}{\partial \theta} \quad (64)$$

and

$$\frac{\partial}{\partial y} = \frac{\partial \rho}{\partial y} \frac{\partial}{\partial \rho} + \frac{\partial \theta}{\partial y} \frac{\partial}{\partial \theta}, \quad (65)$$

and using the equations of the principal curvatures, namely

$$\text{tr}[\mathcal{C}] = C_1 + C_2 = \frac{\partial^2 \eta}{\partial x^2} + \frac{\partial^2 \eta}{\partial y^2} \quad (66)$$

and

$$\det[\mathcal{C}] = C_1 C_2 = \frac{\partial^2 \eta}{\partial x^2} \frac{\partial^2 \eta}{\partial y^2} - \left( \frac{\partial^2 \eta}{\partial x \partial y} \right)^2, \quad (67)$$

it can be shown that the principal curvatures in polar coordinates with azimuthal symmetry are  $C_1 = \frac{\partial^2 \eta}{\partial \rho^2}$  and  $C_2 = \frac{1}{\rho} \frac{\partial \eta}{\partial \rho}$ . Then the Gaussian curvature contributes energy of the form

$$G_{\text{Gauss}} = \kappa_G \int_S (C_1 \cdot C_2) d^2 \rho. \quad (68)$$

Splitting the membrane into the domain and its surrounding region, this is written as

$$G_{\text{Gauss}} \simeq 2\pi \left( \kappa_G^{(1)} \int_0^{\rho_o} \left( \frac{\partial^2 \eta_1}{\partial \rho^2} \cdot \frac{1}{\rho} \frac{\partial \eta_1}{\partial \rho} \right) \rho d\rho + \kappa_G^{(2)} \int_{\rho_o}^{\infty} \left( \frac{\partial^2 \eta_2}{\partial \rho^2} \cdot \frac{1}{\rho} \frac{\partial \eta_2}{\partial \rho} \right) \rho d\rho \right) \quad (69)$$

where  $\kappa_G^{(i)}$  is the saddle-splay (Gaussian bending) modulus in region  $i$ . This can be evaluated by partial integration, writing

$$\int_0^{\rho_o} \left( \frac{\partial^2 \eta_1}{\partial \rho^2} \cdot \frac{1}{\rho} \frac{\partial \eta_1}{\partial \rho} \right) \rho d\rho = \left( \frac{\partial \eta_1}{\partial \rho} \right)^2 \Big|_0^{\rho_o} - \int_0^{\rho_o} \left( \frac{\partial^2 \eta_1}{\partial \rho^2} \cdot \frac{\partial \eta_1}{\partial \rho} \right) d\rho \quad (70)$$

which simplifies to

$$2\pi \kappa_G^{(1)} \int_0^{\rho_o} \left( \frac{\partial^2 \eta_1}{\partial \rho^2} \cdot \frac{\partial \eta_1}{\partial \rho} \right) d\rho = \pi \kappa_G^{(1)} \epsilon^2, \quad (71)$$

and likewise

$$2\pi \kappa_G^{(2)} \int_{\rho_o}^{\infty} \left( \frac{\partial^2 \eta_2}{\partial \rho^2} \cdot \frac{\partial \eta_2}{\partial \rho} \right) d\rho = -\pi \kappa_G^{(2)} \epsilon^2. \quad (72)$$

Finally, the contribution from Gaussian curvature is

$$G_{\text{Gauss}} = \pi \epsilon^2 (\kappa_G^{(1)} - \kappa_G^{(2)}) = \pi \kappa_b \epsilon^2 \cdot \frac{\kappa_G^{(1)} - \kappa_G^{(2)}}{\kappa_b}. \quad (73)$$

For a linear elastic and incompressible bilayer [8, 9], it has been analytically estimated that  $\kappa_b \simeq -\kappa_G$  [4], which has been experimentally supported in some lipid mixtures [4, 10], though measurements of  $\kappa_G$  are notoriously difficult due to its topological invariance through the Gauss-Bonnet Theorem. Given that this estimate shows that the magnitude of the Gaussian and mean bending moduli should be equal in each region, and that the mean bending modulus does not vary significantly between regions, we assume the dimensionless difference in the saddle-splay bending modulus between the domain and surrounding membrane is small (*i.e.*  $(\kappa_G^{(1)} - \kappa_G^{(2)})/\kappa_b \ll 1$ ), and hence ignore the contribution from Gaussian curvature altogether. That said, if we take the implications of this estimate for an incompressible bilayer at face value, we can write the energy of eqn. 73 as

$$G_{\text{Gauss}} = \pi \kappa_b \epsilon^2 (1 - \sigma), \quad (74)$$

and this term can be added to the total free energy, allowing Gaussian curvature to affect the morphological transition.

## 1.5 Equilibrium Domain Shapes

Having examined the elastic contributions to the free energy and origin of the boundary conditions, the problem statement is then to find minimizers of the total free energy, eqn. 61, where we allow  $\epsilon$ ,  $\beta$ , and  $\rho_o$  to vary independently. Hence we generate three simultaneous equations

$$\frac{\partial G}{\partial \epsilon} = 0 \quad \frac{\partial G}{\partial \beta} = 0 \quad \frac{\partial G}{\partial \rho_o} = 0. \quad (75)$$

Physically, the first equation can be interpreted as torque balance at the phase boundary, the second equation as conservation of domain area, and the third equation as lateral force balance at the phase boundary. The first equation can be written as<sup>2</sup>

$$\epsilon \left[ \sigma \beta \rho_o \frac{J_0(\beta \rho_o)}{J_1(\beta \rho_o)} + \rho_o \frac{K_0(\rho_o)}{K_1(\rho_o)} \right] = \sigma \rho_o v_o, \quad (76)$$

the second equation is the same as eqn. 55

$$\alpha = \pi \rho_o^2 \left[ 1 + \frac{\epsilon^2}{2} \left( 1 + \left( \frac{J_0(\beta \rho_o)}{J_1(\beta \rho_o)} \right)^2 - \frac{2}{\beta \rho_o} \frac{J_0(\beta \rho_o)}{J_1(\beta \rho_o)} \right) \right], \quad (77)$$

and the third equation is<sup>3</sup>

$$\frac{\epsilon^2}{2} \left[ \rho_o \left( \left( \frac{K_0(\rho_o)}{K_1(\rho_o)} \right)^2 - 1 \right) - \rho_o \sigma \beta^2 \left( 1 + \left( \frac{J_0(\beta \rho_o)}{J_1(\beta \rho_o)} \right)^2 \right) \right] = \rho_o (\sigma \beta^2 + 1) - \chi, \quad (78)$$

where we have used the first equation to greatly simplify the third. Specifying a particular dimensionless area, dimensionless line tension, and dimensionless spontaneous curvature we can use these three equations to solve for the boundary slope, Lagrange multiplier, and projected radius that minimize the free energy. Although, it is not that straightforward to find solutions; due to the oscillatory nature of  $J_k$ , there are actually multiple, discrete domain shapes that solve these equilibrium equations. Examining eqn. 76, we note that possible solutions of this equation, corresponding to discrete domain shapes, are separated by the discrete zeros of  $J_1(\beta \rho_o)$ . To a good approximation the  $n$ th zero of  $J_1(\beta \rho_o)$  is given by

$$\beta \rho_o = \frac{\pi}{4} + (n - 1)\pi, \quad (79)$$

where  $n \in [1 \dots \infty]$  is an integer. With this knowledge, we can bound the values of  $\beta \rho_o$  for the  $n$ th discrete domain shape to

$$\frac{\pi}{4} + (n - 1)\pi < \beta \rho_o < \frac{\pi}{4} + n\pi. \quad (80)$$

Thus, based on the values of  $\beta \rho_o$ , we know which discrete shape we are solving for, that is, which  $n$  mode shape. As  $n$  increases, the bounded values of  $\beta \rho_o$  push the elastic energy to ever higher levels, such that from the perspective of shapes that are accessible to thermal fluctuations, only the  $n = 1$  shape is accessible for all reasonable parameter values. Further, the line tensions required to buckle the domain for  $n > 1$  are outside the range of reasonable values. To demonstrate these concepts, Fig. 2 shows the numerical solutions to the equilibrium equations

---

<sup>2</sup>The inclusion of  $G_{\text{Gauss}}$  adds the term  $(1 - \sigma)$  in the brackets, modifying the quantitative results slightly.

<sup>3</sup>The inclusion of  $G_{\text{Gauss}}$  adds the term  $2\frac{\sigma-1}{\rho_o}$  in the brackets, modifying the quantitative results slightly.

for  $n = 1$  and  $n = 2$ . Looking at Fig. 2e, one can see that our dimpled solutions are within the bounds of eqn. 80 for  $n = 1$ .

Having picked the regime of lowest energy dimpling, we would also like to know where in the space of dimensionless area and line tension the dimpled states lie, that is, where is the phase boundary? We will explore this question in the scenario where  $v_o = 0$ ; in the case where  $v_o \neq 0$ , there is no stable flat state and hence no phase boundary for the lowest energy mode.

Approaching the phase boundary from either large domain area or large line tension the boundary slope  $\epsilon \rightarrow 0$  at some critical value of the membrane parameters, and hence in the above equations we can ignore terms  $O(\epsilon^2)$ . Not only does this simplify the equations, but precisely at the phase boundary, the  $O(\epsilon^2)$  terms are identically zero, such that the first equation gives

$$\sigma\beta \frac{J_0(\beta\rho_o)}{J_1(\beta\rho_o)} + \frac{K_0(\rho_o)}{K_1(\rho_o)} = 0, \quad (81)$$

the second equation gives

$$\rho_o = \sqrt{\frac{\alpha}{\pi}}, \quad (82)$$

and the third equation gives

$$\chi = \rho_o(\sigma\beta^2 + 1). \quad (83)$$

The first two equations can be solved numerically to find the critical value  $\beta_c$  at the phase boundary as a function of  $\alpha$ , and then the critical line tension for dimpling is  $\chi_c = (\sigma\beta_c^2 + 1)\sqrt{\alpha/\pi}$ . In the regime where the dimensionless domain area is small the relationship between these three equations simplifies to<sup>4</sup>

$$\chi_c \simeq 8\sigma\sqrt{\frac{\pi}{\alpha}}. \quad (84)$$

## 1.6 Scaling and the Critical Exponent

Using an approximation similar to how we derived the morphological phase boundary we can also derive the critical exponent of the dimpling transition. This exponent gives us a notion of how ‘fast’ a domain dimples once the transition has occurred, which is an important shape characteristic of the dimpling transition and will be crucial for understanding how domain interactions scale with domain size and size asymmetry.

It can be shown that the quantity  $\beta\rho_o \simeq \beta_c\sqrt{\alpha/\pi}$  after the domain has dimpled, as demonstrated in Fig. 2e. This approximation allows us to write the domain area conservation as

$$\alpha \simeq \pi\rho_o^2 \left(1 + \delta\frac{\epsilon^2}{2}\right), \quad (85)$$

where  $\delta = O(1)$  is a constant determined from eqn. 55. Using this equation solved for  $\rho_o$  and eqn. 83 solved for  $\beta$ , we can form a complicated transcendental equation with eqn. 81. For small domain area, this transcendental equation can be used to write the boundary slope as

$$|\epsilon| \simeq \sqrt{\frac{2}{\delta} \left( \frac{\chi}{\chi_c} - 1 \right)}, \quad (86)$$

or using eqn. 84 as

$$|\epsilon| \simeq \sqrt{\frac{1}{\delta} \left( \frac{\alpha}{\alpha_c} - 1 \right)}, \quad (87)$$

---

<sup>4</sup>The inclusion of  $G_{\text{Gauss}}$  changes this equation to  $\chi_c \simeq 4(\sigma + 1)\sqrt{\pi/\alpha}$ .

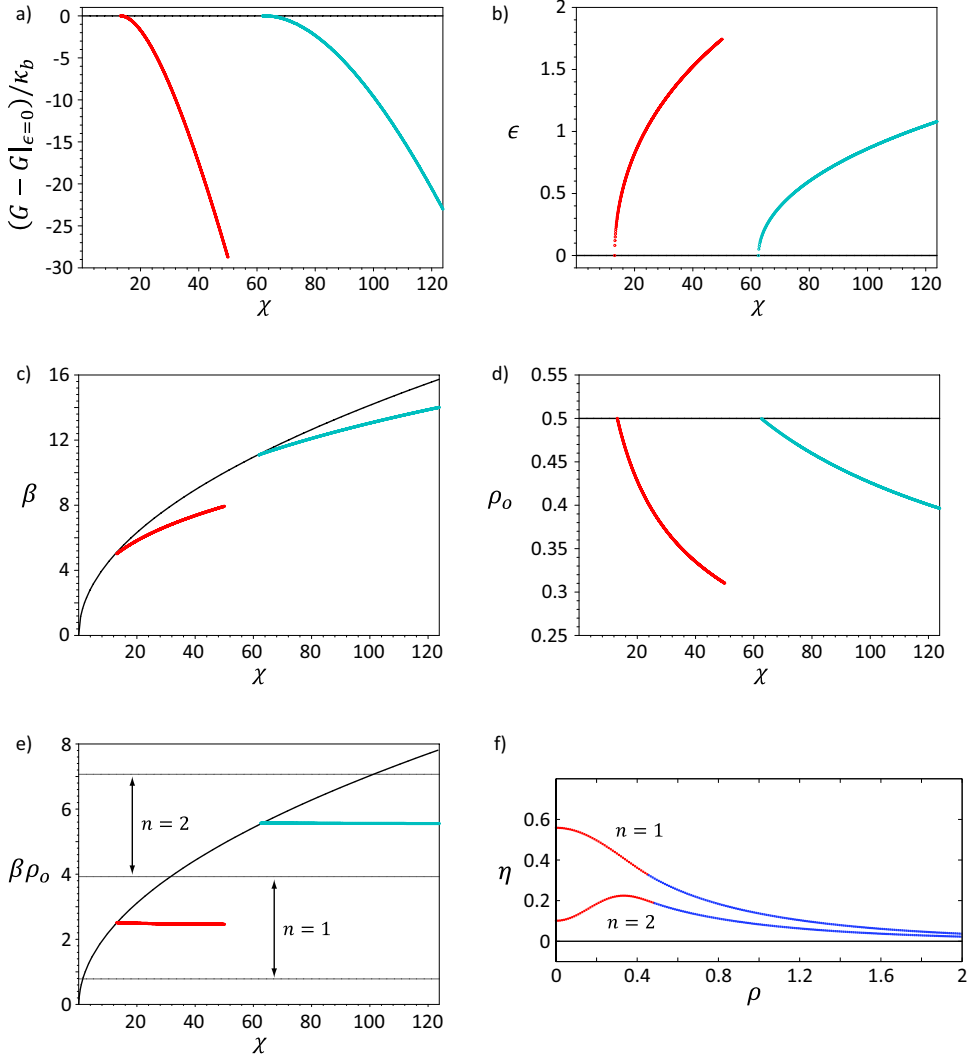


Figure 2: Numerical solutions for the equilibrium equations. Plots (a-d) show how morphological parameters vary as  $\chi$  increases, with  $\alpha = \pi/4$  and  $\sigma = 1$ . The red lines are for  $n = 1$ , while the blue lines are for  $n = 2$ , the black lines correspond to the flat state. e) This plot demonstrates that the values of  $\beta \rho_o$  are indeed bounded by eqn. 80, and that the product  $\beta \rho_o$  is approximately constant through the morphological transition. f) This plots shows the domain shapes for the modes ( $n = 1$ ,  $\chi \simeq 17$ ) and ( $n = 2$ ,  $\chi \simeq 68$ ).

with  $\alpha_c = 64\pi(\sigma/\chi)^2$ . An additional an  $O(1)$ , numerically-determined and multiplicative constant can be employed to make eqns. 86 and 87 even more accurate. This calculation shows that the critical exponent is equal to 1/2, whether line tension or domain area is increased, which means that the domains rise rapidly from the flat state once they have gone through the dimpling transition.

## 1.7 Divergence Theorem Solution for the Deformation Energy

We previously made use of the dimensionless functionals

$$G_{\text{el}}^{(1)} = \frac{\kappa_b}{2} \sigma \int_S \left( -\beta^2 (\nabla \eta_1)^2 + (\nabla^2 \eta_1)^2 \right) d^2 \rho \quad (88)$$

and

$$G_{\text{el}}^{(2)} = \frac{\kappa_b}{2} \int_S \left( (\nabla \eta_2)^2 + (\nabla^2 \eta_2)^2 \right) d^2 \rho, \quad (89)$$

which describe the contributions to the free energy from bending and membrane tension. Using the resulting Euler-Lagrange equations in the domain region

$$\nabla^2(\nabla^2 + \beta^2)\eta_1 = 0 \quad (90)$$

and

$$\nabla^2(\nabla^2 - 1)\eta_2 = 0 \quad (91)$$

in the surrounding membrane, we apply the boundary conditions  $|\nabla \eta_1(0)| = |\nabla \eta_2(\infty)| = 0$  and  $|\nabla \eta_1(\rho_o)| = |\nabla \eta_2(\rho_o)| = \epsilon$ . From these differential equations and boundary conditions we found solutions for the membrane shape

$$\eta_1(\rho) = -\epsilon \left[ \frac{1}{\beta} \frac{J_0(\beta\rho)}{J_1(\beta\rho_o)} - \frac{1}{\beta} \frac{J_0(\beta\rho_o)}{J_1(\beta\rho_o)} + \frac{K_0(\rho_o)}{K_1(\rho_o)} \right] \quad \text{and} \quad \eta_2(\rho) = -\epsilon \frac{K_0(\rho)}{K_1(\rho_o)}. \quad (92)$$

It might appear that the only way to solve for the energy given  $\eta_1$  and  $\eta_2$  is to perform a rather tedious integral, when in fact, there is a much more elegant way using the Divergence Theorem, in a way similar to previous calculations [7, 11].

We will perform a series of partial integrations in rapid succession, by rewriting the derivatives in the energy functional. We start by noticing

$$(\nabla \eta)^2 = \nabla \cdot (\eta \nabla \eta) - \eta \nabla^2 \eta. \quad (93)$$

The second derivative term is a bit more challenging, we notice that

$$\nabla \cdot (\nabla^2 \eta \nabla \eta) = \nabla^3 \eta \cdot \nabla \eta + (\nabla^2 \eta)^2 \quad (94)$$

and

$$\nabla \cdot (\eta \nabla^3 \eta) = \nabla^3 \eta \cdot \nabla \eta + \eta \nabla^4 \eta. \quad (95)$$

Subtracting these two equations yields

$$(\nabla^2 \eta)^2 = \eta \nabla^4 \eta + \nabla \cdot (\nabla^2 \eta \nabla \eta - \eta \nabla^3 \eta). \quad (96)$$

Let us tackle the functionals for the two regions separately; in region 1

$$-\beta^2 (\nabla \eta_1)^2 + (\nabla^2 \eta_1)^2 = \nabla \cdot (\nabla^2 \eta_1 \nabla \eta_1 - \eta_1 \nabla^3 \eta_1 - \beta^2 \eta_1 \nabla \eta_1) + \beta^2 \eta_1 \nabla^2 \eta_1 + \eta_1 \nabla^4 \eta_1, \quad (97)$$

which can be rearranged to

$$-\beta^2(\nabla\eta_1)^2 + (\nabla^2\eta_1)^2 = \nabla \cdot (\nabla^2\eta_1\nabla\eta_1 - \eta_1\nabla(\nabla^2 + \beta^2)\eta_1) + \eta_1\nabla^2(\nabla^2 + \beta^2)\eta_1. \quad (98)$$

Then recall that the Euler-Lagrange equations demand  $\nabla^2(\nabla^2 + \beta^2)\eta_1 = 0$ , and further, our condition that the change in area upon dimpling be finite gives  $(\nabla^2 + \beta^2)\eta_1 = const$ , hence this can be simplified to

$$-\beta^2(\nabla\eta_1)^2 + (\nabla^2\eta_1)^2 = \nabla \cdot (\nabla^2\eta_1\nabla\eta_1). \quad (99)$$

Upon substitution into the energy functional for region 1 we find

$$G_{el}^{(1)} = \frac{\kappa_b}{2}\sigma \int_S \left( -\beta^2(\nabla\eta_1)^2 + (\nabla^2\eta_1)^2 \right) d^2\rho = \frac{\kappa_b}{2}\sigma \int_S \nabla \cdot (\nabla^2\eta_1\nabla\eta_1) d^2\rho, \quad (100)$$

and then using the divergence theorem

$$G_{el}^{(1)} = \frac{\kappa_b}{2}\sigma \int_S \nabla \cdot (\nabla^2\eta_1\nabla\eta_1) d^2\rho = \frac{\kappa_b}{2}\sigma \oint_{\partial S} (\nabla^2\eta_1\nabla\eta_1) \cdot d\hat{\mathbf{n}}. \quad (101)$$

This last expression can be fully evaluated without a particular functional form of  $\eta_1$ , simply by applying azimuthal symmetry and knowing the boundary conditions, namely  $\nabla\eta_1(0) = 0\hat{\rho}$  and  $\nabla\eta_1(\rho_o) = \epsilon\hat{\rho}$ , resulting in

$$G_{el}^{(1)} = \pi\sigma\kappa_b\rho_o\epsilon(\nabla^2\eta_1)|_{\rho=\rho_o}. \quad (102)$$

The second region surrounding the domain is handled in a similar fashion. We write the integrand of the functional as

$$(\nabla\eta_2)^2 + (\nabla^2\eta_2)^2 = \nabla \cdot (\nabla^2\eta_2\nabla\eta_2 - \eta_2\nabla^3\eta_2 + \eta_2\nabla\eta_2) - \eta_2\nabla^2\eta_2 + \eta_2\nabla^4\eta_2, \quad (103)$$

which can be reorganized to

$$(\nabla\eta_2)^2 + (\nabla^2\eta_2)^2 = \nabla \cdot (\nabla^2\eta_2\nabla\eta_2 - \eta_2\nabla(\nabla^2 - 1)\eta_2) + \eta_2\nabla^2(\nabla^2 - 1)\eta_2. \quad (104)$$

In a similar fashion, application of the Euler-Lagrange equation,  $\nabla^2(\nabla^2 - 1)\eta_2 = 0$ , and the finite area change condition,  $(\nabla^2 - 1)\eta_2 = const$ , yield

$$(\nabla\eta_2)^2 + (\nabla^2\eta_2)^2 = \nabla \cdot (\nabla^2\eta_2\nabla\eta_2). \quad (105)$$

With subsequent application of the Divergence Theorem we get a relation similar to region 1, namely

$$G_{el}^{(2)} = \frac{\kappa_b}{2} \int_S \nabla \cdot (\nabla^2\eta_2\nabla\eta_2) d^2\rho = \frac{\kappa_b}{2} \oint_{\partial S} (\nabla^2\eta_2\nabla\eta_2) \cdot d\hat{\mathbf{n}}, \quad (106)$$

where application of the symmetry and boundary conditions, specifically  $\lim_{\rho \rightarrow \infty} \rho|\nabla\eta_2| = 0$  and  $\nabla\eta_2(\rho_o) = \epsilon\hat{\rho}$ , yields

$$G_{el}^{(2)} = -\pi\kappa_b\rho_o\epsilon(\nabla^2\eta_2)|_{\rho=\rho_o}. \quad (107)$$

Now we see that the total elastic free energy is a measure of the curvature change at the boundary between the two regions

$$G_{el} = \pi\kappa_b\rho_o\epsilon [\sigma(\nabla^2\eta_1) - (\nabla^2\eta_2)]|_{\rho=\rho_o}. \quad (108)$$

Using the solutions from the Euler-Lagrange equation, we recover the previously stated energy

$$G_{el} = \pi\kappa_b\rho_o\epsilon^2 \left( \sigma\beta \frac{J_0(\beta\rho_o)}{J_1(\beta\rho_o)} + \frac{K_0(\rho_o)}{K_1(\rho_o)} \right). \quad (109)$$

## 2 Vesicle Tension and Entropy

To keep our mechanical model of membrane morphology tractable and intuitive, certain assumptions were made about the physical state of the membrane. One of our assumptions was that the addition of membrane area due to domain deformation came at a constant cost per unit area, thus setting up a constant tension ensemble. In this section we will examine this assumption in detail, and show that while useful, the constant tension ensemble cannot be blindly employed in all situations. In particular, if the area change connected to a morphological transition (or set of transitions) is too large compared to a reference area, we must consider the membrane tension as a variable, thermally-dependent mechanical attribute of the membrane.

The choice of tension ensemble affects the equilibrium stability of domain morphologies. Our formulation of the equations of mechanical equilibrium shows that the dimpled domain morphology is at an energy extremum, however the use of a Lagrange multiplier turns that extremum into a saddle-point, hence obscuring the exact nature of the shape stability. Some of our preliminary work, using fully non-linear finite element methods, suggests that the dimpled morphology might only be a stable shape if the tension is a monotonically increasing function of the additional area required to deform the membrane. Fortunately, that is precisely the behavior described by a thermally active membrane - a regime of constant tension if domain deformations are small, and a monotonically increasing tension regime if the deformations are large.

For a vesicle with conserved volume and surface area, lateral tension may arise from one of two general sources. At higher tensions, the intrinsic area per lipid increases, corresponding to an areal strain ( $\phi$ ) and tension ( $\tau$ ) on the vesicle surface given by  $\tau \simeq K_A\phi$ , essentially the bilayer equivalent of Hooke's Law. At much lower tensions, this Hookean linear response is not valid; thermal fluctuations of the membrane absorb free area, generating a small, non-linear entropic tension. Our goal in this section is to use a common Fourier space technique to construct a model of this entropic tension [4, 12], namely the equation of state, and determine its implications for the constancy (or lack thereof) of tension on the surface of GUVs with lipid domains that change morphology. This analysis informs the generic mechanical model of the limits of the approximation of the constant tension ensemble. The result of this calculation will also help us form a more accurate model of membrane elasticity and deformation at finite temperature.

To these ends, the following subsections derive the equation of state in rigorous detail, and build intuition for how bending and tension regulate the thermal fluctuations of the membrane. An expression for the contribution to the free energy from a thermally active membrane is derived and a connection is made between the free energy in this thermal ensemble with the zero temperature, constant tension ensemble. Lastly, we try to estimate how changes in domain morphology couple to the thermal fluctuations on a conserved volume and surface area vesicle.

### 2.1 Constructing a Thermal Ensemble

Arguably, one of the most important concepts to discuss when constructing a mechanical model of a membrane is the ensemble in use, which can be loosely defined as the physical or thermodynamic relationship between the patch of membrane of interest and the external physical world. Looking back at eqn. 22, we see that the tension,  $\tau$ , is a material constant, independent of the shape of the membrane itself. This description is a constant tension ensemble, where changes in morphology add area at infinity, by pulling membrane from an external membrane reservoir at a fixed energy cost per unit area. This problem statement is strictly a mechanical model, free from the effects of temperature, or more precisely, it is a statistical mechanical model at

$T = 0$ . A real membrane at finite temperature is bombarded by various small molecules, (*e.g.* water, ions, and proteins) such that it is never in a flat state. Instead, the membrane undulates in time, with height fluctuations having a specific frequency spectrum that will be derived in this section. These undulations store area that can be surrendered upon application of tension, however the energetic cost of this change in projected unit area is not constant. This constitutes a new kind of tension ensemble, that links the tension in the mechanically deformed membrane region to the variable tension in a thermal membrane reservoir using an equation of state.

The physical reality is that changes in domain morphology (or any change in membrane morphology) and finite temperature bilayer undulations are happening simultaneously on the same patch of membrane, and are energetically coupled together. This coupling combined with only a statistical notion of the fluctuations makes this a difficult scenario to model. One avenue of approach is to construct an entropic tension ensemble as follows. The domain and its attendant mechanical morphologies exist on an infinite patch of membrane at zero temperature, and hence we can model domain morphologies within the framework of standard continuum mechanics. We then construct a thermally active membrane reservoir, with projected area  $\mathcal{A}$  and total area  $\mathcal{A}_o$ , that is able to exchange area with the zero temperature membrane patch, such that the total membrane area in the system is conserved, as shown in Fig. 3. By fixing the total area in the system and setting  $\mathcal{A}$  and  $\mathcal{A}_o$ , the equation of state of the reservoir defines the tension in *both* membrane regions. As the zero temperature membrane patch deforms, it pulls area from the thermal membrane reservoir, increasing the tension in both regions according to the non-linear equation of state. This effectively allows us to calculate membrane shapes with a strictly mechanical model, as we have done previously, but couples the continuum mechanics to an accurate representation of a bilayer of finite extent at finite temperature. Additionally, we will show that this analysis clarifies the relevance of the constant tension ensemble. For a system with a large enough thermal reservoir, the ratio  $\Delta\mathcal{A}/\mathcal{A}_o \ll 1$ , and hence the initial state of tension remains essentially unchanged when the zero temperature membrane changes morphology. If this condition is not met, we must consider the non-linear behavior of the equation of state, and its corresponding effects on the stability of dimpled and budded domain morphologies. The general result is that the non-linear equation of state yields a variable tension that tends to stabilize the dimpled state if enough excess area is available.

## 2.2 The Equation of State

We calculate the linearized equation of state in this low tension regime by splitting the reservoir's deformation profile, denoted here as simply  $h$ , into planar Fourier modes and using equipartition to calculate the amplitude of each mode. To derive the equation of state, we follow the standard treatment given in [4, 12] with all details shown here for completeness. Recall that the linearized deformation energy is given by

$$G_{\text{el}} = \frac{1}{2} \int_{\mathcal{S}} \left( \tau (\nabla h)^2 + \kappa_b (\nabla^2 h)^2 \right) d^2 \mathbf{r}, \quad (110)$$

where  $\mathcal{S}$  is the planar projected surface. The projected surface area is  $\mathcal{A}$ , and we assume for now that we are operating in the entropic tension regime where the area per lipid is conserved. While a two dimensional path integral formulation,

$$Z = \int \mathcal{D}[h] e^{-\frac{G_{\text{el}}[h]}{k_B T}}, \quad (111)$$

which constructs the partition function  $Z$  by summing the Boltzmann factors over all possible membrane configurations, is conceptually most straightforward, we will employ a Fourier space

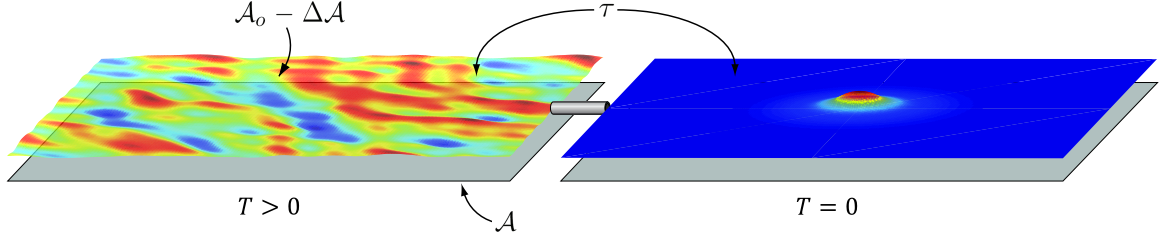


Figure 3: Schematic of an ensemble that couples the lateral tension of a zero temperature deformation field to a finite temperature membrane reservoir. The reservoir (left) has a total area  $A_o - \Delta A$  and a projected area  $A$ , where  $\Delta A \in [0 \dots (A_o - A)]$ . The mechanically deformed region (right - with dimpled domain) has an infinite projected area and an actual area  $\Delta A$  above the projected area, where  $\Delta A$  is the area required to deform the zero temperature membrane from a flat state. The small pipe represents a perfect thermal insulator that permits the flow of lipid from one region to the other, where the total amount of lipid in the ensemble is conserved, resulting in equal tension in both regions. When the zero temperature membrane is flat, the thermal reservoir has a projected area  $A$  and actual area  $A_o$ , which, through the equation of state, defines an initial resting tension in both regions.

approach to calculate the equation of state. For any *Monge* representation of the surface, we can write the membrane deformation as the Fourier transform

$$h(\mathbf{r}) = \frac{\mathcal{A}}{(2\pi)^2} \int h(\mathbf{q}) e^{-i\mathbf{q}\cdot\mathbf{r}} d^2\mathbf{q}, \quad (112)$$

with

$$\mathbf{q} = \frac{2\pi}{\sqrt{\mathcal{A}}} \mathbf{k}, \quad (113)$$

where  $\mathbf{k} = (n_1, n_2)$  with  $n_1$  and  $n_2$  as integer wave numbers. For a sufficiently large membrane, we are well-justified in using the continuous Fourier Transform, though this approximation breaks down for patches of membrane with area near the area of a single lipid. Then the vector derivatives from the energy functional are

$$\nabla h = \frac{\mathcal{A}}{(2\pi)^2} \int (-i\mathbf{q}) h(\mathbf{q}) e^{-i\mathbf{q}\cdot\mathbf{r}} d^2\mathbf{q}, \quad (114)$$

and

$$\nabla^2 h = -\frac{\mathcal{A}}{(2\pi)^2} \int |\mathbf{q}|^2 h(\mathbf{q}) e^{-i\mathbf{q}\cdot\mathbf{r}} d^2\mathbf{q}, \quad (115)$$

such that the terms of the deformation functional become

$$(\nabla h)^2 = \frac{\mathcal{A}^2}{(2\pi)^4} \int \int (\mathbf{q} \cdot \mathbf{q}') h(\mathbf{q}) \overline{h(\mathbf{q}')} e^{-i(\mathbf{q}-\mathbf{q}')\cdot\mathbf{r}} d^2\mathbf{q} d^2\mathbf{q}', \quad (116)$$

and

$$(\nabla^2 h)^2 = \frac{\mathcal{A}^2}{(2\pi)^4} \int \int (\mathbf{q} \cdot \mathbf{q}')^2 h(\mathbf{q}) \overline{h(\mathbf{q}')} e^{-i(\mathbf{q}-\mathbf{q}')\cdot\mathbf{r}} d^2\mathbf{q} d^2\mathbf{q}'. \quad (117)$$

Explicitly performing the spatial integrals gives

$$\int (\nabla h)^2 d^2\mathbf{r} = \frac{\mathcal{A}^2}{(2\pi)^4} \int \int \int (\mathbf{q} \cdot \mathbf{q}') h(\mathbf{q}) \overline{h(\mathbf{q}')} e^{-i(\mathbf{q}-\mathbf{q}')\cdot\mathbf{r}} d^2\mathbf{q} d^2\mathbf{q}' d^2\mathbf{r}, \quad (118)$$

and

$$\int (\nabla^2 h)^2 d^2 \mathbf{r} = \frac{\mathcal{A}^2}{(2\pi)^4} \int \int \int (\mathbf{q} \cdot \mathbf{q}')^2 h(\mathbf{q}) \overline{h(\mathbf{q}')} e^{-i(\mathbf{q}-\mathbf{q}') \cdot \mathbf{r}} d^2 \mathbf{q} d^2 \mathbf{q}' d^2 \mathbf{r}. \quad (119)$$

We recognize that

$$\int e^{-i(\mathbf{q}-\mathbf{q}') \cdot \mathbf{r}} d^2 \mathbf{r} = (2\pi)^2 \delta(\mathbf{q} - \mathbf{q}'), \quad (120)$$

such that these integrals simplify to

$$\int (\nabla h)^2 d^2 \mathbf{r} = \left( \frac{\mathcal{A}}{2\pi} \right)^2 \int |\mathbf{q}|^2 |h(\mathbf{q})|^2 d^2 \mathbf{q} \quad (121)$$

and

$$\int (\nabla^2 h)^2 d^2 \mathbf{r} = \left( \frac{\mathcal{A}}{2\pi} \right)^2 \int |\mathbf{q}|^4 |h(\mathbf{q})|^2 d^2 \mathbf{q}. \quad (122)$$

The deformation energy can now be written as a sum of independent Fourier modes

$$G_{\text{el}} = \frac{1}{2} \left( \frac{\mathcal{A}}{2\pi} \right)^2 \int_{\frac{\pi}{\sqrt{\mathcal{A}}}}^{\frac{\pi}{\sqrt{a_o}}} |h(\mathbf{q})|^2 (\tau |\mathbf{q}|^2 + \kappa_b |\mathbf{q}|^4) d^2 \mathbf{q}, \quad (123)$$

where we integrate from the smallest  $q$  vector magnitude, corresponding to the size of the entire projected membrane  $\pi/\sqrt{\mathcal{A}}$ , to the highest  $q$  vector magnitude, corresponding to the lipid intermolecular spacing  $\pi/\sqrt{a_o}$ , where  $a_o$  is the area per lipid.

This free energy can now be used in the canonical partition function to calculate various properties of interest on a fluctuating membrane at equilibrium. The amplitudes of each mode,  $|h(\mathbf{q})|$ , are degrees of freedom over which we can sum the partition function, however, since they are independent quadratic degrees of freedom, we know that each mode absorbs energy  $k_B T/2$  from the thermal reservoir, such that

$$\frac{k_B T}{2} = \langle |h(\mathbf{q})|^2 \rangle \frac{\mathcal{A}}{2} (\tau |\mathbf{q}|^2 + \kappa_b |\mathbf{q}|^4), \quad (124)$$

and from the definition of the Fourier transform in eqn. 112, a factor of  $\mathcal{A}/(2\pi)^2$  remains with the integral, and this can be rearranged to

$$\langle |h(\mathbf{q})|^2 \rangle = \frac{k_B T}{\mathcal{A} (\tau |\mathbf{q}|^2 + \kappa_b |\mathbf{q}|^4)}. \quad (125)$$

Using our previously defined elastic decay length,  $\lambda = \sqrt{\kappa_b/\tau}$ , this can be recast in a form with fewer effective parameters,

$$\langle |h(\mathbf{q})|^2 \rangle = \lambda^2 \frac{k_B T}{\tau \mathcal{A}} \frac{1}{(\lambda |\mathbf{q}|)^2 + (\lambda |\mathbf{q}|)^4}, \quad (126)$$

useful for making scaling arguments. To get a feel for the magnitudes of these fluctuations, we can plug in the minimum and maximum wave vectors to find the maximum and minimum, respectively, root-mean-square height deviations, and find

$$\left[ \sqrt{\langle |h(\mathbf{q})|^2 \rangle} \right]_{|\mathbf{q}|_{\max}} \simeq \frac{a_o}{\pi^2} \left( \frac{k_B T}{\mathcal{A} \kappa_b} \right)^{1/2} \sim 10^{-7} \text{ nm} \quad (127)$$

and

$$\left[ \sqrt{\langle |h(\mathbf{q})|^2 \rangle} \right]_{|\mathbf{q}|_{\min}} \simeq \left[ \frac{k_B T}{\pi^2 \tau} \left( 1 + \frac{(\pi \lambda)^2}{\mathcal{A}} \right)^{-1} \right]^{1/2} \sim 100 \text{ nm}, \quad (128)$$

on a vesicle with a  $20 \mu\text{m}$  diameter and resting tension of  $10^{-5} k_B T / \text{nm}^2$ . Thus we see that on small length scales, the membrane is locally very flat. To get an idea of the membrane height gradient over different wavelengths, which helps validate the use of a Monge gauge, we can multiply these height deviations by their corresponding wave vector magnitude to find

$$|\nabla h|_{\min} \simeq \left[ |\mathbf{q}| \sqrt{\langle |h(\mathbf{q})|^2 \rangle} \right]_{|\mathbf{q}|_{\max}} \simeq \left( \frac{a_o k_B T}{\pi^2 \mathcal{A} \kappa_b} \right)^{1/2} \sim 10^{-6} \quad (129)$$

and

$$|\nabla h|_{\max} \simeq \left[ |\mathbf{q}| \sqrt{\langle |h(\mathbf{q})|^2 \rangle} \right]_{|\mathbf{q}|_{\min}} \simeq \left[ \frac{k_B T}{\tau \mathcal{A}} \left( 1 + \frac{(\pi \lambda)^2}{\mathcal{A}} \right)^{-1} \right]^{1/2} \sim 0.01. \quad (130)$$

These estimates give us two important pieces of information. The estimate of the root-mean-square height fluctuation tells us that in the ‘real’ physical scenario, on the length scales of domain morphology the thermal fluctuations will be statistically smaller than the height deformations caused by domain morphology. The second estimate shows that the small gradient approximation employed through this section is valid for studying membrane fluctuations.

To better understand the nature of the thermal fluctuations, specifically to build intuition for how the fluctuation modes are regulated, we examine two naturally-arising regimes in more detail. For small  $\lambda|\mathbf{q}|$ , the quadratic term dominates the denominator to give a log-log power law of the form

$$\ln \left[ \langle |h(\mathbf{q})|^2 \rangle \frac{\tau \mathcal{A}}{\lambda^2 k_B T} \right] = -2 \ln [\lambda|\mathbf{q}|], \quad (131)$$

while for large  $\lambda|\mathbf{q}|$ , the quartic term dominates and to give a log-log power law of the form

$$\ln \left[ \langle |h(\mathbf{q})|^2 \rangle \frac{\tau \mathcal{A}}{\lambda^2 k_B T} \right] = -4 \ln [\lambda|\mathbf{q}|]. \quad (132)$$

Where these two power laws cross is the ‘corner’ frequency,  $\lambda|\mathbf{q}|_c = 1$ , as shown in Fig. 4a. Frequencies below the corner frequency, having a much higher amplitude, absorb the vast majority of the free area, and hence are almost exclusively regulated by tension. On the other hand, frequencies above the corner frequency correspond to a high degree of curvature but do not absorb significant area, and hence are almost exclusively regulated by bending stiffness.

Moving towards the equation of state of the reservoir, as we have shown in previous sections, the difference between projected and actual area can be written as an integral, and can now also be represented in Fourier-space as

$$\mathcal{A}_o - \mathcal{A} = \frac{1}{2} \int (\nabla h)^2 d^2 \mathbf{r} = \frac{1}{2} \left( \frac{\mathcal{A}}{2\pi} \right)^2 \int \langle |h(\mathbf{q})|^2 \rangle |\mathbf{q}|^2 d^2 \mathbf{q}, \quad (133)$$

where upon replacing the formula for the mean mode variances we find

$$\mathcal{A}_o - \mathcal{A} = \frac{k_B T}{4\pi \kappa_b} \frac{\mathcal{A}}{2\pi} \int \frac{1}{\frac{\tau}{\kappa_b} + |\mathbf{q}|^2} d^2 \mathbf{q}. \quad (134)$$

By choosing polar coordinates on an isotropic membrane,  $d^2\mathbf{q} = 2\pi q dq$ , this can be written as

$$\frac{\mathcal{A}_o - \mathcal{A}}{\mathcal{A}} = \frac{k_B T}{4\pi\kappa_b} \int_{\frac{\pi}{\sqrt{\mathcal{A}}}}^{\frac{\pi}{\sqrt{a_o}}} \frac{q}{\frac{\tau}{\kappa_b} + q^2} dq. \quad (135)$$

The single greatest contribution to the integrand comes from modes at the corner frequency. The result of this integral is the entropic equation of state [12]

$$\frac{\mathcal{A}_o - \mathcal{A}}{\mathcal{A}} = \frac{k_B T}{8\pi\kappa_b} \ln \left[ \frac{1 + \frac{\pi^2 \kappa_b}{a_o \tau}}{1 + \frac{\pi^2 \kappa_b}{\mathcal{A} \tau}} \right]. \quad (136)$$

This equation of state is the mathematical relationship that, for a given bending modulus, relates a given total membrane area and tension to the observed projected area, or alternately stated, it relates the total membrane area and given projected area to the magnitude of tension on the membrane. This equation of state is the key to deriving the energetic contribution to membrane deformation free energy from the thermal reservoir. Additionally, it is straight forward to include membrane stretch because it corresponds to the relatively simple transformation  $\mathcal{A}_o \rightarrow \mathcal{A}_o(1 + \tau/K_A)$ , such that the equation of state becomes

$$\frac{\mathcal{A}_o}{\mathcal{A}} \left( 1 + \frac{\tau}{K_A} \right) - 1 = \frac{k_B T}{8\pi\kappa_b} \ln \left[ \frac{1 + \frac{\pi^2 \kappa_b}{a_o \tau}}{1 + \frac{\pi^2 \kappa_b}{\mathcal{A} \tau}} \right], \quad (137)$$

and now  $\mathcal{A}_o$  is interpreted as the full, zero tension area of the bilayer.

From eqn. 136, notice that if  $\tau \rightarrow \infty$  or  $T \rightarrow 0$ , the right-hand side goes to zero and  $\mathcal{A} = \mathcal{A}_o$ , confirming that  $\mathcal{A}_o$  is the actual area of the membrane, or in other words, the number of lipids multiplied by the equilibrium area per lipid, and implies  $\mathcal{A} < \mathcal{A}_o$ . Examining the right-hand side of this equation, two reference tensions emerge, between which nearly all tensions of interest lie. From the denominator, the lower bound reference tension is set by  $\pi^2\kappa_b/\mathcal{A}_o \sim 10^{-7} k_B T / \text{nm}^2 \ll \tau$  for any sufficiently large piece of membrane (e.g. vesicle with radius 10  $\mu\text{m}$  or more). Likewise, from the numerator, the upper bound reference tension is  $\pi^2\kappa_b/a_o \sim 400 k_B T / \text{nm}^2 \gg \tau$  considering that a nominal membrane will rupture at tensions above  $\sim 5 k_B T / \text{nm}^2$ . Thus within that range the equation of state can be written as

$$\frac{\mathcal{A}_o - \mathcal{A}}{\mathcal{A}} \simeq \frac{k_B T}{8\pi\kappa_b} \ln \left[ \frac{\pi^2 \kappa_b}{a_o \tau} \right]. \quad (138)$$

This also shows that for sufficiently large patches of membrane, the lower bound wave vector plays almost no role in the equation of state. Likewise, the equation of state is only logarithmically sensitive to any errors in choice of the maximum wave vector. Together, these facts give us confidence that the equation of state is rather robust, and does not depend on the fine details of lipid structure, nor large-scale membrane conformations. Looking back at eqn. 136, as tension decreases towards zero, the projected area shrinks to a state where the bending rigidity stabilizes the membrane undulations. In the limit of zero membrane tension, the difference between the actual and projected areas increases to a degree defined by

$$\frac{\mathcal{A}_o - \mathcal{A}}{\mathcal{A}} \Big|_{\tau=0} = \frac{k_B T}{8\pi\kappa_b} \ln \left[ \frac{\mathcal{A}}{a_o} \right]. \quad (139)$$

The solution to this transcendental equation for  $\mathcal{A}$  is the minimum projected area of the membrane,  $\mathcal{A}_{\min}$ , where with reasonable values for the bending modulus and area per lipid, it is

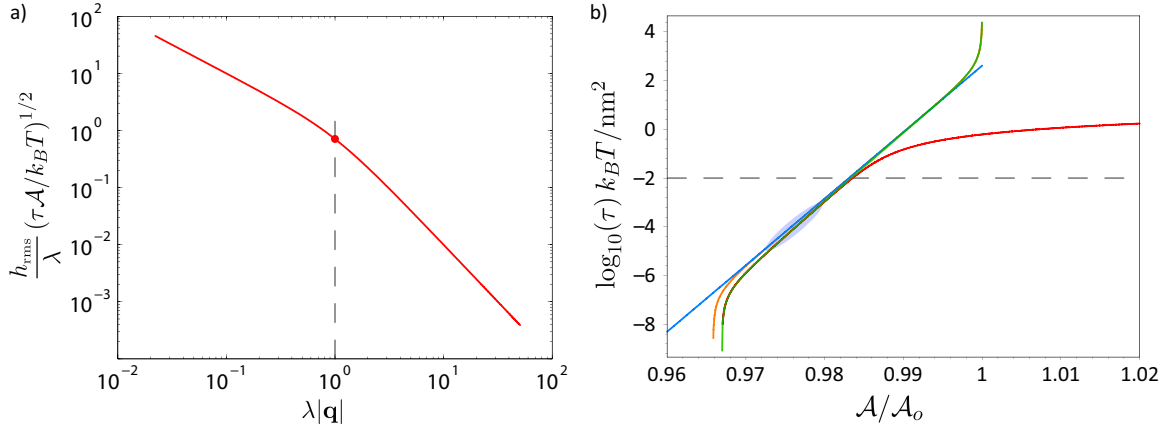


Figure 4: Regimes of Entropic Tension. a) Log-log plot of the fluctuation RMS height as a function of the dimensionless wave vector magnitude. The relatively high RMS height of frequencies below the corner frequency is regulated by tension, while the very low RMS height of frequencies greater than the corner frequency is regulated by bending. The circle indicates the corner frequency at which fluctuations switch from being tension regulated to bending regulated. b) Plots of the entropic tension as a function of frame area relative to total, zero tension bilayer area. The green line is the exact formula from eqn. 141, while the orange and blue lines are the approximations of eqn. 143. The red line is the full entropic and elastic equation of state from eqn. 137. The grey ellipse shows the approximate regime of entropic tension in which our experiments reside, known from measurements of the elastic decay length  $\lambda$ . The dashed line shows the tension above which one must account for changes in  $a_o$  due to stretch. For all plots the bending modulus is  $\kappa_b = 25 k_B T$ , the lipid size is  $a_o = 0.6 \text{ nm}^2$ , the stretch modulus is  $K_A = 60 k_B T/\text{nm}^2$ , and the nominal vesicle size is  $\mathcal{A}_o = 4\pi(10000 \text{ nm})^2$ .

straightforward to show that the maximum entropic areal strain is bounded by

$$0 < \frac{\mathcal{A}_o - \mathcal{A}}{\mathcal{A}} \Big|_{\tau=0} \leq 0.05, \quad (140)$$

for all reasonable membrane sizes, implying that in many situations we can use  $\mathcal{A} \simeq \mathcal{A}_o$  - this will be a useful approximation in calculations that follow. In fact, this upper bound areal strain is not reached until  $\mathcal{A}_o/a_o \sim 10^{15}$ ! The exact entropic equation of state (eqn. 136) can be explicitly solved for  $\tau$ , yielding

$$\tau = \frac{\pi^2 \kappa_b}{a_o} \cdot \frac{1 - \frac{a_o}{\mathcal{A}} e^{\left(\frac{\mathcal{A}_o - \mathcal{A}}{\mathcal{A}} \frac{8\pi\kappa_b}{k_B T}\right)}}{e^{\left(\frac{\mathcal{A}_o - \mathcal{A}}{\mathcal{A}} \frac{8\pi\kappa_b}{k_B T}\right)} - 1}. \quad (141)$$

This equation of state represents a derivative of the free energy with respect to projected area, namely

$$G_{\text{ent}} = \int_{\mathcal{A}_{\min}}^{\mathcal{A}} \tau(\mathcal{A}') d\mathcal{A}', \quad (142)$$

with  $\kappa_b$ ,  $\mathcal{A}_o$  and  $a_o$  as parameters. The difficulty of this integral is significantly reduced if we realize that in certain strategic locations, we can substitute  $\mathcal{A} \rightarrow \mathcal{A}_o$ , justified by the implications of eqn. 139, to get

$$\tau = \frac{\pi^2 \kappa_b}{a_o} \cdot \frac{1 - \frac{a_o}{\mathcal{A}_o} e^{\left(\frac{\mathcal{A}_o - \mathcal{A}}{\mathcal{A}_o} \frac{8\pi\kappa_b}{k_B T}\right)}}{e^{\left(\frac{\mathcal{A}_o - \mathcal{A}}{\mathcal{A}_o} \frac{8\pi\kappa_b}{k_B T}\right)} - 1} \simeq \frac{\pi^2 \kappa_b}{a_o} e^{-\frac{8\pi\kappa_b}{k_B T} \frac{\mathcal{A}_o - \mathcal{A}}{\mathcal{A}_o}}. \quad (143)$$

Integrating this equation gives

$$G_{\text{ent}} = G_o + k_B T \frac{\pi \mathcal{A}_o}{8a_o} e^{-\frac{8\pi\kappa_b}{k_B T} \frac{\mathcal{A}_o - \mathcal{A}}{\mathcal{A}_o}}, \quad (144)$$

with  $G_o$  defined by  $G_{\text{ent}}|_{\mathcal{A}=\mathcal{A}_{\min}} = 0$ . The meaning of this equation is unambiguous; as we increase the frame area from its zero tension resting value of  $\mathcal{A}_{\min}$ , the free energy exponentially increases because the entropic undulations of the membrane are flattened out. Recalling the arrangement we are using to connect domain morphology to the thermal membrane reservoir, as shown in Fig. 3, we interpret changes in morphology as changes in the actual amount of lipid in the thermal reservoir, such that

$$\Delta\mathcal{A} = \frac{1}{2} \int_S (\nabla h)^2 d^2\mathbf{r}, \quad (145)$$

where this height function  $h$  resides in the zero temperature region. Substituting this into the free energy, we can write the elastic functional as

$$G_{\text{el}} = G_{\text{ent}}|_{\mathcal{A}_o \rightarrow \mathcal{A}_o - \Delta\mathcal{A}} + \frac{\kappa_b}{2} \int_S (\nabla^2 h)^2 d^2\mathbf{r}, \quad (146)$$

or more explicitly as

$$G_{\text{el}} = G_o + k_B T \frac{\pi \mathcal{A}_o}{8a_o} e^{-\frac{8\pi\kappa_b}{\mathcal{A}_o k_B T} (\mathcal{A}_o - \mathcal{A} - \frac{1}{2} \int_S (\nabla h)^2 d^2\mathbf{r})} + \frac{\kappa_b}{2} \int_S (\nabla^2 h)^2 d^2\mathbf{r}, \quad (147)$$

and the variation is still taken with respect to  $h$ , as  $\frac{\delta G_{\text{el}}}{\delta h} = 0$ . This has the pleasing property that if the morphological deformation field is zero, the membrane system returns to the equation of state defined by entropic fluctuations.

We can take this calculation a few steps further by asking: In what regime does the constant tension ensemble match the results of this entropic ensemble? Looking at the first two terms of eqn. 147, the regime where tension would be constant is

$$\frac{8\pi\kappa_b}{k_B T} \frac{\Delta\mathcal{A}}{\mathcal{A}_o} \ll 1, \quad (148)$$

yielding the approximation to the entropic component of the free energy

$$G_{\text{ent}} \simeq G_o + k_B T \frac{\pi \mathcal{A}_o}{8a_o} e^{-\frac{8\pi\kappa_b}{k_B T} \frac{\mathcal{A}_o - \mathcal{A}}{\mathcal{A}_o}} \left( 1 + \frac{8\pi\kappa_b}{k_B T} \frac{\Delta\mathcal{A}}{\mathcal{A}_o} \right). \quad (149)$$

Readjusting the zero of the free energy, this can be written as

$$G_{\text{ent}} \simeq G'_o + \underbrace{\frac{\pi^2 \kappa_b}{a_o} e^{-\frac{8\pi\kappa_b}{k_B T} \frac{\mathcal{A}_o - \mathcal{A}}{\mathcal{A}_o}}}_{\text{eqn. 143 for } \tau} \frac{1}{2} \int_S (\nabla h)^2 d^2 \mathbf{r}. \quad (150)$$

Taking a nominal bending modulus of  $\kappa_b = 25 k_B T$  and vesicle diameter of  $20 \mu\text{m}$ , we can use eqn. 148 to estimate the area change above which we must consider changes to the entropic reservoir, and find that the tension is approximately constant for the upper bound value of  $\Delta\mathcal{A} < 2 \mu\text{m}^2$ . This means that a single domain with flat radius of roughly  $800 \text{ nm}$  or less can fully bud without changing the resting tension in the membrane significantly. In another estimate, this means that on the vesicle surface  $\sim 150$  domains of area  $\alpha = \pi/4$  with  $\lambda = 1 \mu\text{m}$ , which in real units corresponds to domains with a flat diameter  $1 \mu\text{m}$ , can dimple to have a boundary slope of  $\epsilon = 0.25$  and still maintain an essentially constant frame tension. This is a reasonable estimate which says that the constant tension ensemble is relevant, although depending on the vesicle size and the exact composition of the lipid mixture, the domains may be larger and/or more numerous, and the dimpling process may yield lower values of  $\Delta\mathcal{A}$  per domain than the above estimates depending on the values of  $\epsilon$ . This alludes to a model where it is the total area change of all domains that couples to the tension of the thermal reservoir; hence for tension to be constant, domains must not only be small, but there must be low enough number of them such that their combined  $\Delta\mathcal{A}$  is less than the values suggested by eqn. 148.

To put these results in further experimental context, we explore how the entropic tension changes when a domain of area  $\mathcal{A}_D$ , on a GUV with area  $\mathcal{A}_o$ , changes its morphology from flat to budded. We assume the vesicle is nearly spherical, and hence the volume of the vesicle is  $V = \mathcal{A}^{3/2}/3\sqrt{4\pi}$ , where  $\mathcal{A}$  represents the frame area of the GUV with the flat domain. We assume the domain forms a spherical bud, in which case, it requires volume  $V_D = \mathcal{A}_D^{3/2}/3\sqrt{4\pi}$  to complete this change in morphology. This change in volume corresponds to a change in frame area, such that the new frame area is

$$\mathcal{A}_n = \left( \mathcal{A}^{3/2} - \mathcal{A}_D^{3/2} \right)^{\frac{2}{3}}. \quad (151)$$

Via the phase boundary, the same morphological change isolates a certain amount of lipid from the vesicle, such that

$$\mathcal{A}'_o = \mathcal{A}_o - \mathcal{A}_D. \quad (152)$$

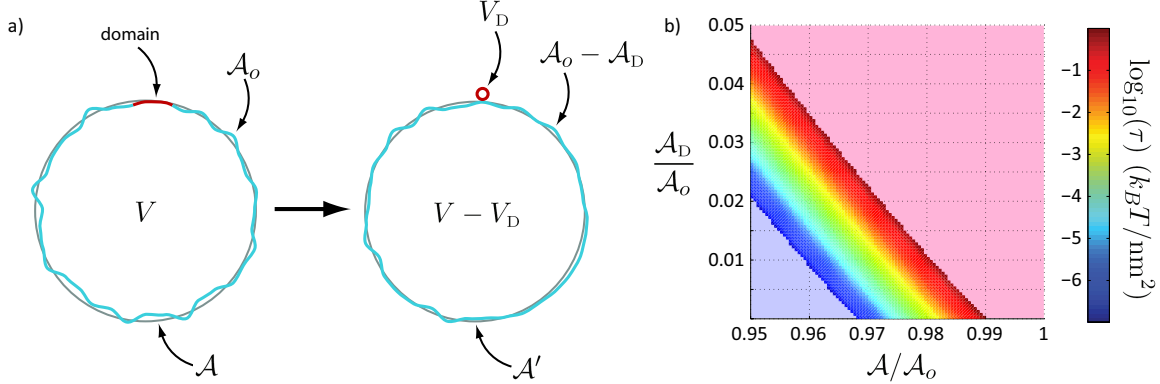


Figure 5: Effects of domain budding on entropic tension. a) This schematic shows how the budding of a domain from a large vesicle, conserves total membrane area and enclosed volume, but changes the frame area and actual area available for fluctuations on the vesicle, increasing the entropic tension. b) Plot of the membrane tension upon budding of a domain whose size is a fraction of the total membrane area,  $A_D/A_o$ , where the initial state had a relative frame area  $A/A_o$ , which specifies an initial state of tension. The light blue area indicates tensions below the minimum tension  $\pi^2 \kappa_b / A_o$ , whereas the light red region indicates tensions where membrane stretch becomes important.

This effectively causes a change of variable in eqn. 141 from

$$\frac{A_o}{A} \rightarrow \frac{A'_o}{A_n} = \frac{1 - \frac{A_D}{A_o}}{\left( \left( \frac{A}{A_o} \right)^{3/2} - \left( \frac{A_D}{A_o} \right)^{3/2} \right)^{2/3}} \simeq \frac{A_o}{A} \left( 1 - \frac{A_D}{A_o} \right). \quad (153)$$

We can now calculate the tension as a function of the relative frame area ( $A/A_o$ ) and the budding domain area relative to the total vesicle area ( $A_D/A_o$ ), as shown in Fig. 5.

The end result of these calculations is that there is a regime in which tension is constant and a regime in which tension rises exponentially as a domain changes morphology. In which regime a vesicle finds itself depends on the number and size distribution of domains on its surface. It is likely that for large vesicles with a low number of small domains, the tension is approximately constant, while for vesicles with larger, more numerous domains the tension cannot be considered constant. In those cases where the tension is exponentially sensitive to domain morphology, it should not have an effect on the actual shape of the dimpled domain because one can always readjust the zero of the free energy about the current state of tension and explore shapes in that region of phase space under the approximation of the constant tension ensemble. Further, we speculate that an exponentially rising tension has the effect of stabilizing dimples against budding; in a sense, complicating the relatively simple phase diagram of the constant tension ensemble, by demanding that we know not only elastic constants of the membrane and domain size, but extrinsic features of the membrane, like the total membrane area.

### 3 The 1D Interaction Potential

As mentioned in the text, the 1D interaction potential is an approximation that makes calculations relatively easy by absorbing all the changes that occur during interaction into the boundary

conditions of the surrounding membrane. The following subsection will derive the 1D potential in detail and explain the manner in which boundary conditions are imposed. In addition, these ideas permit us to examine how differences in domain size might effect the pairwise interaction potential. We explicitly assume that the shapes of the domains are constant during the interaction; the domains are only allowed to rotate with respect to the flat integration plane. However, the membrane surrounding the domain is allowed to deform in response to this rotation. Casting this into a one-dimensional model allows us to easily find analytical solutions for the interaction potential. In one dimension, there are three regions of membrane to consider: two regions of membrane which extend from the outer domain edges out to infinity on either side and an inner region between the two domains from  $-d/2$  to  $d/2$ , where  $d$  is the separation between domain edges.

The elastic energy of the 1D membrane deformation, like the 2D case, is a sum of tension and bending terms. Using Fig. 6, let us refer to the blue region to left with the label  $l$ , the blue region in between the domains with the label  $c$ , and the blue region to the right with the label  $r$ . Then, similar to the 2D scenario, in the left region the elastic energy is

$$G_l[\eta_l(x)] = \frac{\kappa_b s}{2\lambda} \int_{-\infty}^0 \left( \left( \frac{\partial \eta_l}{\partial x_l} \right)^2 + \left( \frac{\partial^2 \eta_l}{\partial x_l^2} \right)^2 \right) dx_l, \quad (154)$$

in the right region

$$G_r[\eta_r(x)] = \frac{\kappa_b s}{2\lambda} \int_0^\infty \left( \left( \frac{\partial \eta_r}{\partial x_r} \right)^2 + \left( \frac{\partial^2 \eta_r}{\partial x_r^2} \right)^2 \right) dx_r, \quad (155)$$

and in the center region

$$G_c[\eta_c(x)] = \frac{\kappa_b s}{2\lambda} \int_{-\frac{d}{2}}^{\frac{d}{2}} \left( \left( \frac{\partial \eta_c}{\partial x_c} \right)^2 + \left( \frac{\partial^2 \eta_c}{\partial x_c^2} \right)^2 \right) dx_c. \quad (156)$$

Then the total elastic energy is the sum of these three parts. The parameter  $s$  is the effective one dimensional length over which the interaction occurs; the exact value is absorbed into the data fitting routine. In Fig. 6,  $s$  would be the distance the membrane goes ‘into’ the page. These functionals generate Euler-Lagrange equations identical in form to those in section 2, however they are now one dimensional. The solutions are all of the form

$$\eta_i = a_1^{(i)} e^{x_i} + a_2^{(i)} e^{-x_i} + a_3^{(i)} x_i + a_4^{(i)}. \quad (157)$$

As we will show, there are two qualitatively different interactions that are distinct realizations of the same four boundary conditions. The results of this analysis are that we explain the domain repulsion in terms of elastic parameters and domain morphology and predict as of yet unobserved attractive interactions for opposite parity domains. Further, we can use results from previous sections to estimate the effects of domain size and size asymmetry.

### 3.1 Interactions of Asymmetric Domains

We refer to domains whose curvature have the same sign as being of the same ‘parity’, however their size, boundary slope or elastic properties may differ. The parity itself is encoded by the sign of the slope boundary condition, whereas size asymmetry or elastic differences are reflected in the magnitude of the boundary slope and projected domain sizes as demonstrated in the following calculation.

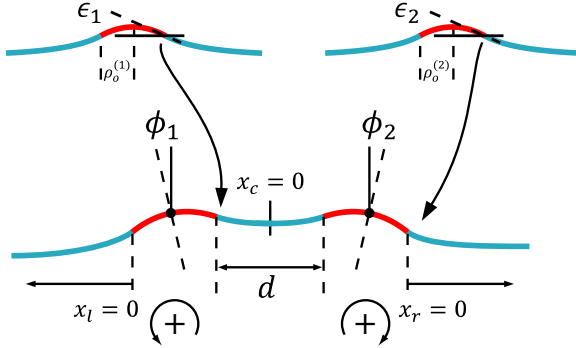


Figure 6: A detailed view of the four distinct boundary conditions in the 1D model of interaction between two dimpled domains. If both domains are the same size, then  $\epsilon_1 = \epsilon_2$  and  $\phi_1 = \phi_2$ . The boundary slopes,  $\epsilon_i$ , are set by the single domain energy minimization described earlier. The inner domain edge separation is  $d$ , and the tilt angle sign convention is shown below each angle  $\phi_i$ . The energy is calculated by integrating the membrane shape over the three blue regions, adherent to the boundary conditions.

For the outer membrane regions, the boundary conditions are that the membrane be flat far from the domain edges, in particular

$$\frac{\partial \eta_l}{\partial x_l} \Big|_{x_l=-\infty} = \frac{\partial \eta_r}{\partial x_r} \Big|_{x_r=\infty} = 0, \quad (158)$$

that the change in 1D ‘area’ due to interaction be finite, and we arbitrarily set  $x_l(-\infty) = x_r(\infty) = 0$ , which immediately leads to

$$\eta_l = a_1 e^{x_l}, \quad (159)$$

for the left hand side and

$$\eta_r = a_2 e^{-x_r}, \quad (160)$$

for the right hand side. As the domains approach each other, a preferred rotation angle will emerge; applying the small gradient/angle approximation, namely  $\tan(\phi_i) \simeq \phi_i$ , this boundary slope is

$$\frac{\partial \eta_l}{\partial x_l} \Big|_{x_l=0} = \phi_1 - \epsilon_1, \quad (161)$$

in the left region and

$$\frac{\partial \eta_r}{\partial x_r} \Big|_{x_r=0} = \epsilon_2 - \phi_2, \quad (162)$$

in the right region. Taking  $\phi_i$  and  $s/\lambda$  as small allows us to neglect the small contributions to the interaction energy from the change in domain projected area with the rotations  $\phi_i$ . Then the final solutions for the outer regions are

$$\eta_l = (\phi_1 - \epsilon_1) e^{x_l} \quad \text{and} \quad \eta_r = (\phi_2 - \epsilon_2) e^{-x_r}. \quad (163)$$

In the inner region  $\epsilon_2$  changes sign and the slope boundary conditions read

$$\frac{\partial \eta_c}{\partial x_c} \Big|_{x_c=-d/2} = \epsilon_1 + \phi_1 \quad \text{and} \quad \frac{\partial \eta_c}{\partial x_c} \Big|_{x_c=d/2} = -(\epsilon_2 + \phi_2). \quad (164)$$

Additionally, for the membrane to be contiguous, we must impose the height boundary conditions

$$\eta_c|_{x=-d/2} = \eta_l|_{x_l=0} + 2\rho_o^{(1)}\phi_1 \quad (165)$$

on the left side and

$$\eta_c|_{x=d/2} = \eta_r|_{x_r=0} + 2\rho_o^{(2)}\phi_2 \quad (166)$$

on the right side, where again we have applied the small angle approximation. Application of these four boundary conditions yields a complicated expression for the membrane shape in between the domains.

The solutions for the membrane shape in the three regions can be integrated in the appropriate elastic functionals, giving a rather complicated expression for the energy as a function of  $\phi_1$  and  $\phi_2$ . The preferred domain tilt is found by minimizing this energy with respect to the available rotations,  $\frac{\partial G}{\partial \phi_i} = 0$ , giving

$$\phi_1(d) \simeq -\epsilon_2 e^{-d} \quad \text{and} \quad \phi_2(d) \simeq -\epsilon_1 e^{-d}. \quad (167)$$

Substituting the exact equations for  $\phi_i(d)$  into  $G(d) = G_l + G_c + G_r$  gives the 1D interaction potential in the small gradient limit

$$G(d) = 2\kappa_b\epsilon_1\epsilon_2 \frac{s}{\lambda} e^{-d} \left( 1 + f(\epsilon_i, \rho_o^{(i)}, d) \right) \simeq 2\kappa_b\epsilon_1\epsilon_2 \frac{s}{\lambda} e^{-d}, \quad (168)$$

where the function  $f$  is

$$f = \frac{\left( \rho_o^{(1)}\epsilon_2 - \rho_o^{(2)}\epsilon_1 \right)^2}{\epsilon_1\epsilon_2} \left[ 4\rho_o^{(1)}\rho_o^{(2)} + e^d \left( d - 2 + 2(\rho_o^{(1)} + 1)^2 + 2(\rho_o^{(2)} + 1)^2 \right) \right]^{-1}. \quad (169)$$

Using the relationships for  $\rho_o^{(i)}(\alpha_i, \epsilon_i)$  and  $\epsilon_i(\alpha_i)$  from eqns. 85 and 87, respectively, one can show that  $f \ll 1$  for all reasonable parameter values.

In processing the experimental data, we made the assumption that the material properties of all domains were identical and their areas were approximately equal, hence  $\epsilon_1 = \epsilon_2$ , thus the two outer regions of membrane are identical, the inner region is an even function, and  $f = 0$ . One important feature to notice about this potential is that  $\epsilon_1$  and  $\epsilon_2$  are multiplicative factors; if both domains have the same parity they will repel, whereas if they have opposite parity they will attract. Size asymmetry is addressed in some detail in the following subsection. The precise fit model used in data analysis was

$$G(r) = a_1 e^{-r/\lambda} + a_2, \quad (170)$$

where  $a_i$  are fit parameters, and the distance parameter used in the text is  $r = \lambda(2\rho_o + d)$ , where throughout this section we refer to  $\lambda_2 = \lambda$ . The constant  $a_2$  shifts the zero of the potential which is arbitrarily set when taking the logarithm of the radial distribution function.

Prior to our work, theoretical efforts [13] showed that membrane proteins which deform the membrane midplane exert a repulsive force on each other of the limiting form

$$G(r) \simeq \pi\kappa_b [2\epsilon_1\epsilon_2\rho_o^2 K_0(r/\lambda) + (\epsilon_1^2 + \epsilon_2^2)\rho_o^4 K_2^2(r/\lambda)] \simeq 2\pi\kappa_b\epsilon_1\epsilon_2\rho_o^2 K_0(r/\lambda). \quad (171)$$

Assuming that the dimpled domain shape is constant during interaction, this model maps directly onto the domain interaction scenario with the effective cross-section of interaction having the intuitively pleasing form of projected domain area  $s \simeq \lambda\pi\rho_o^2$ . This model and the exponential

model can be fit to the data presented in the text. The two models are visually indistinguishable in their fit quality, though there is a slight change in the measured length-scale of interaction, of about 12%. Fig. 7 graphically compares these two models to experimental data.

Additionally, we used fully non-linear, 2D finite element calculations of the elastic interaction of domains to validate these analytical models; the results for an example symmetric interaction are shown in Fig. 8.

### 3.2 Effects of Domain Size Asymmetry

Due to the stochastic nature of how domains initially form, there are always slight (or sometimes more than slight) size differences between all the domains on a vesicle's surface. This experimental reality is demonstrated in the domain area histograms of Figs. 13, 14 and 15. In this subsection we derive scaling laws that allow us to comment on how mean domain size and size asymmetry affect the strength of the interaction. We presume that on the surface of a vesicle the domains are sparse enough that pairwise interactions dominate, that is, multi-body interactions are negligible.

We begin by rewriting the exponential interaction as a function of the domain center-to-center distance,  $r = \lambda(\rho_o^{(i)} + \rho_o^{(j)} + d_{ij})$ , such that we can define the interaction between the  $i$ th and  $j$ th domains as

$$G_{ij} = 2\kappa_b \epsilon_i \epsilon_j \frac{s_{ij}}{\lambda} e^{\left(\rho_o^{(i)} + \rho_o^{(j)}\right)} e^{-r/\lambda}, \quad (172)$$

showing that it is the product of a distance-dependent and size-dependent function; we now examine the size-dependent function, which we will call  $\sigma_{ij}(\alpha_i, \alpha_j)$  for ease of notation. To explicitly calculate how domain sizes affect the strength of the interaction, recall from eqn. 87 that the boundary slope of each domain can be written as

$$|\epsilon_i| \simeq \sqrt{\frac{1}{\delta} \left( \frac{\alpha_i}{\alpha_c} - 1 \right)}, \quad (173)$$

where it is important to note that  $\alpha_c$  is not a domain-dependent quantity - it is set by the material properties of the membrane, and hence for any interaction to take place between domains, *both* must have an area greater than  $\alpha_c$ . For this reason, we define  $\alpha_i/\alpha_c = \hat{\alpha}_i$  where  $\hat{\alpha}_i > 1$ .

To understand the underlying scaling relationship, we must comment on how  $s_{ij}$  behaves with changes in  $\alpha_i$  and  $\alpha_j$ . Clearly, the potential should scale symmetrically with changes in the size of either domain, or in other words  $s(\alpha_i + \Delta\alpha, \alpha_j) = s(\alpha_i, \alpha_j + \Delta\alpha)$  if  $\alpha_i = \alpha_j$ . If we make the approximation that  $s/\lambda \simeq \pi\rho_o^2$  in the case of equal domain areas, as indicated by the 2D model [13], then to lowest order, symmetry dictates that  $s_{ij}/\lambda \simeq \pi\rho_o^{(i)}\rho_o^{(j)}$ . Then using eqn. 85 we can relate the boundary slope and domain size to the projected radius by

$$\rho_o^{(i)} = \sqrt{\frac{2\alpha_c}{\pi} \left( \frac{\hat{\alpha}_i}{\hat{\alpha}_i + 1} \right)}. \quad (174)$$

After a few algebraic manipulations, we can write

$$\sigma_{ij}(\hat{\alpha}_i, \hat{\alpha}_j) = \frac{4}{\delta} \kappa_b \alpha_c \sqrt{\hat{\alpha}_i \hat{\alpha}_j} \sqrt{\frac{(\hat{\alpha}_i - 1)(\hat{\alpha}_j - 1)}{(\hat{\alpha}_i + 1)(\hat{\alpha}_j + 1)}} e^{\sqrt{\frac{2\alpha_c}{\pi}} \left[ \sqrt{\frac{\hat{\alpha}_i}{\hat{\alpha}_i + 1}} + \sqrt{\frac{\hat{\alpha}_j}{\hat{\alpha}_j + 1}} \right]} \quad (175)$$

which characterizes the strength of the pairwise potential given the sizes of the two domains, and material constants. This also gives us the useful scaling relationship that as the average

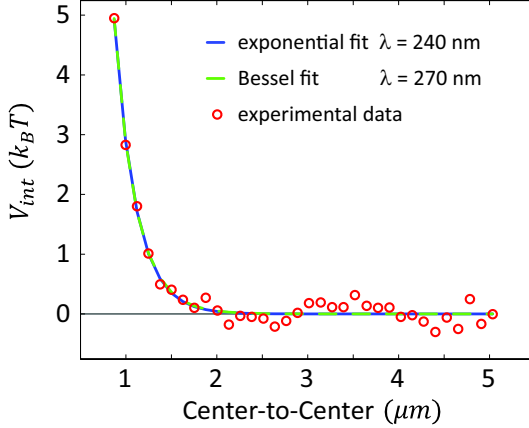


Figure 7: Comparison of different interaction models. Using the same data as in the text, we show graphically that an exponentially repulsive interaction is indistinguishable from a Bessel function repulsion (eqn. 171). The only notable difference is that for such excellent alignment of the two models, a slightly different length-scale of interaction must be chosen for each.

domain size increases, the strength of the potential scales approximately linearly as

$$\sigma(\hat{\alpha}) = \frac{4}{\delta} \kappa_b \alpha_c \hat{\alpha} \cdot \frac{\hat{\alpha} - 1}{\hat{\alpha} + 1} \cdot e^{2\sqrt{\frac{2\alpha_c}{\pi}} \frac{\hat{\alpha}}{\hat{\alpha}+1}}, \quad (176)$$

thus larger domains should repel each other more strongly than smaller domains. We characterize the difference in domain sizes by writing the mean domain size as

$$\bar{\alpha}_{ij} = \frac{1}{2}(\hat{\alpha}_i + \hat{\alpha}_j), \quad (177)$$

and their percent difference as

$$c_{ij} = \frac{\hat{\alpha}_i - \hat{\alpha}_j}{\bar{\alpha}_{ij}}, \quad (178)$$

which defines the transformation  $\bar{\alpha}_{ij}(1 + c_{ij}/2) = \hat{\alpha}_i$  and  $\bar{\alpha}_{ij}(1 - c_{ij}/2) = \hat{\alpha}_j$ . We can make these substitutions to find  $\sigma_{ij}(\bar{\alpha}_{ij}, c_{ij})$ , giving a rather complicated expression for the scaling factor of the potential as a function of the mean size of the two domains and their size difference. Finally, these scaling arguments culminate in Fig. 9, where we take the ratio of the scaling factor for some given value of  $c$  and  $\bar{\alpha}$  and normalize it by the scaling factor at the same  $\bar{\alpha}$  but  $c = 0$  (*i.e.*  $\sigma_{ij}/\sigma_{ij}|_{c=0}$ ), in essence giving a measure of the relative change in the strength of the potential as size asymmetry increases. This ratio is relatively insensitive to the value  $\alpha_c$ , however to be complete, we show plots for two different values of  $\alpha_c$ . The result is that the potential remains relatively unchanged within certain bounds of the size asymmetry. The specific values of this bound are set by the mean size  $\bar{\alpha}$  and a specified tolerance  $p < \sigma_{ij}/\sigma_{ij}|_{c=0} < 1$ . Additionally, this analysis shows that for conserved mean domain size, increasing size asymmetry tends to weaken the strength of the interaction, since  $\sigma_{ij}/\sigma_{ij}|_{c=0} \leq 1$ .

### 3.2.1 Corrections from Size Asymmetry

With these results, we can begin to connect the distribution of sizes found in a real experiment to the manner in which size asymmetry changes the potential of mean force. Specifically, in

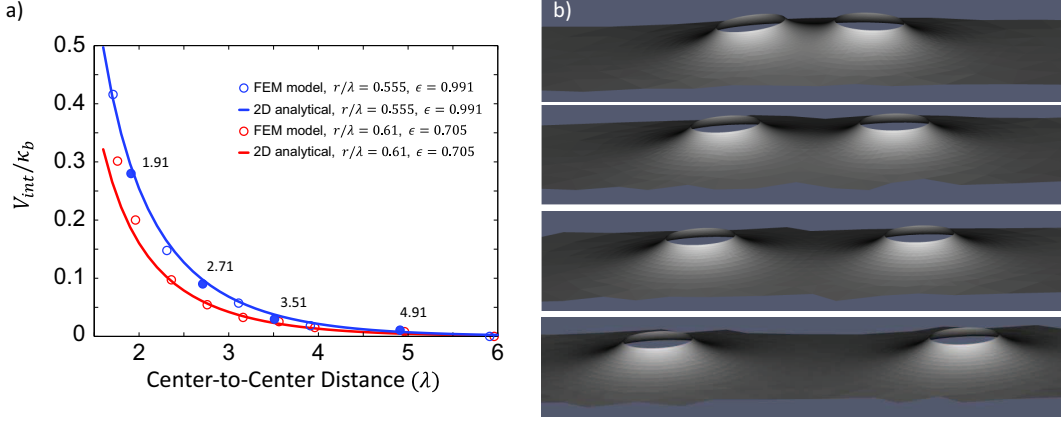


Figure 8: Comparison of the 2D interaction model of [13] and fully non-linear finite-element analysis. a) Plots of the interaction potential between symmetric domains as a function of center-to-center distance for two different domain sizes, as indicated in the legend. The fit functions are of eqn. 171 with  $\epsilon_1 = \epsilon_2$ . b) Non-linear finite element solution for the membrane shape with two rigid, interacting domains - the lipid domains are not shown. As the domains get closer, they tilt as predicted by the 1D theory, and the membrane between them becomes ever more deformed. Each of the solid blue data points in (a) correspond to a frame in (b). This figure made in collaboration with and adapted from [14].

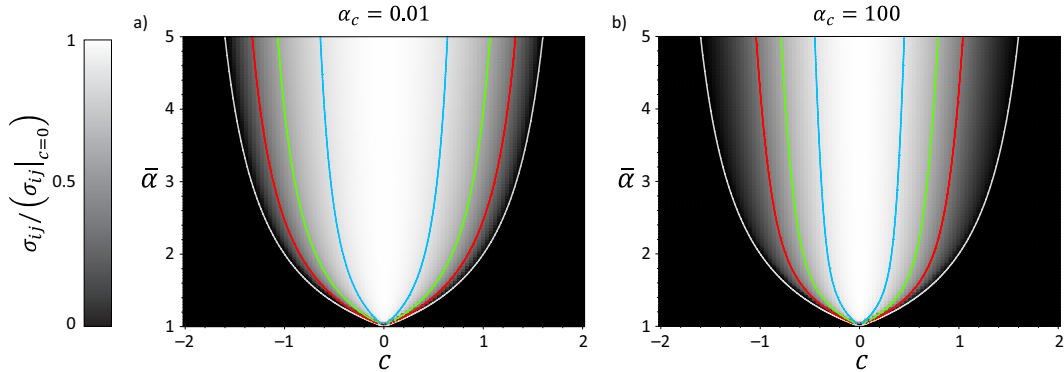


Figure 9: Effects of domain size and size asymmetry on the strength of the interaction potential. Plots (a) and (b) are the ratio of the scaling factor  $\sigma_{ij}$  normalized by the scaling factor with the same mean size but zero size asymmetry. The bounded values of  $c$  are shown for tolerances of  $p = 0.9$  (blue),  $p = 0.7$  (green) and  $p = 0.5$  (red), with the white line outlining the extent of possible values of  $c$  for a given  $\bar{\alpha}$ . If we demand that the change in the strength of the potential be less than 10%, then the size asymmetry should be between  $-1/2 \lesssim c \lesssim 1/2$ . Additionally, these plots show that for a given mean size, asymmetry tends to weaken the potential. Plot (a) uses  $\alpha_c = 0.01$  while plot (b) uses  $\alpha_c = 100$ , showing that the bounds of  $c$  are fairly insensitive to the value of  $\alpha_c$ .

this subsection we will derive a correction to the potential of mean force from the width of the distribution of scaling factors  $\sigma_{ij}$ .

For a vesicle with a given number of domains, there are  $N$  distinct domain pairs, and hence  $N$  distinct pairwise interactions between those domains. The radial distribution function describes the probability of finding two domains a distance  $r$  apart from domain center-to-center. As explained in section 7.1, the measured potential  $V_{\text{eff}}(r)$  is the sum of the potential of mean force, here denoted by  $\bar{G}(r)$ , and a fictitious potential  $V_{\text{fict}}(r)$  that is the same for all domains on a given vesicle. Then the radial distribution function is given by

$$P(r) = \frac{1}{\bar{Z}} e^{-(\bar{G}(r) + V_{\text{fict}}(r))}, \quad (179)$$

where

$$\bar{Z} = \int_0^{2R_{\text{fict}}} e^{-(\bar{G}(r) + V_{\text{fict}}(r))} dr, \quad (180)$$

$R_{\text{fict}}$  is a parameter in the fictitious potential, and the energies are measured in units of  $k_B T$ . The fictitious potential is a property of the vesicle and microscope optics only, and hence is the same for all pair interactions. The upper bound of the integral is set by the fact that  $\lim_{r \rightarrow 2R_{\text{fict}}} [V_{\text{fict}}] = \infty$ . On the vesicle surface the same radial distribution function is given by the sum of the radial distribution functions from each pair of domains, that is

$$P(r) = \frac{1}{N} \sum_{ij} \frac{1}{Z_{ij}} e^{-(G_{ij}(r) + V_{\text{fict}}(r))}, \quad (181)$$

where

$$Z_{ij} = \int_0^{2R_{\text{fict}}} e^{-(G_{ij}(r) + V_{\text{fict}}(r))} dr \quad (182)$$

and  $i$  and  $j$  span the set of distinct domain pairs. Equating these two expressions and solving for the measured potential of mean force gives

$$\bar{G}(r) = -\ln \left[ \frac{\bar{Z}}{N} \sum_{ij} \frac{1}{Z_{ij}} e^{-G_{ij}} \right] = -\ln \left[ \frac{\bar{Z}}{N} \sum_{ij} \frac{1}{Z_{ij}} e^{-\sigma_{ij} e^{-r/\lambda}} \right]. \quad (183)$$

The only change in the pairwise potential from one domain pair to another is the value of  $\sigma_{ij}$  and the only intrinsic parameter that changes from one domain to another is the size  $\alpha$ . Thus for a given distribution of domain sizes  $p(\alpha)$ , there is a distribution of the values of  $\sigma$  for domain pairs,  $p(\sigma)$ , that depends on the joint probability distribution  $p(\alpha_1|\alpha_2) \simeq p(\alpha_1)p(\alpha_2)$ . Finding the connection between these two distributions is quite complicated, and given the complex functional form of  $\sigma_{ij}$  in eqn. 175, we would not be able to analytically solve it. That said, using Monte Carlo methods it is straightforward to generate the appropriate  $p(\alpha_1|\alpha_2)$  and corresponding  $p(\sigma)$  given a measured  $p(\alpha)$ .

Let us assume that the sum can be converted to an integral, such that we can write

$$\bar{G}(r) = -\ln \left[ \int p(\sigma) \frac{\bar{Z}}{Z(\sigma)} e^{-\sigma e^{-r/\lambda}} d\sigma \right]. \quad (184)$$

To make progress, let us posit the form of  $p(\sigma)$  as a Gaussian

$$p(\sigma) = \frac{e^{-\frac{(\sigma-\bar{\sigma})^2}{2a^2}}}{a\sqrt{2\pi}} \quad (185)$$

with a standard deviation  $a$  much smaller than the mean, which allows us to make the approximation  $Z(\sigma) \simeq \bar{Z}$ , and take the bounds of the integral to infinity such that the potential of mean force can be written as

$$\bar{G}(r) \simeq -\ln \left[ \int_{-\infty}^{\infty} p(\sigma) e^{-\sigma e^{-r/\lambda}} d\sigma \right]. \quad (186)$$

Then examining the integral we find

$$\int_{-\infty}^{\infty} p(\sigma) e^{-\sigma e^{-r/\lambda}} d\sigma = e^{\left( \frac{a^2}{2} e^{-2r/\lambda} - \bar{\sigma} e^{-r/\lambda} \right)}, \quad (187)$$

and finally we can write the potential of mean force as the mean pairwise interaction plus a correction term related to the width of the distribution  $p(\sigma)$

$$\bar{G}(r) = \bar{\sigma} e^{-r/\lambda} - \frac{a^2}{2} e^{-2r/\lambda}, \quad (188)$$

although this result is only valid if the underlying distribution for  $\sigma$  is Gaussian. In general the correction term can be arbitrarily complex given the possible distributions of  $p(\alpha)$ , and corresponding distributions of  $p(\sigma)$ . The key points of this result are that it makes sense to approximate the measured potential as a mean pairwise potential, and it shows that asymmetry, here characterized by  $a$ , tends to make the measured potential weaker, a result qualitatively supported by the reduction in the strength and increase in the apparent length scale of the potentials as size asymmetry increases, as shown in Figs. 13, 14 and 15.

## 4 Coarse Control of Membrane Tension and Inducing Phase Separation

As explained in the text of the paper, there are essentially four main parameters that dictate where in the space of possible morphologies a particular vesicle will find itself: bending stiffness, applied membrane tension, phase boundary line tension and domain size. Of those, the bending stiffness and line tension are dictated by the composition of the membrane, and are not thought to be independent of each other [15]. Considering the difficulty of changing composition *in situ* and the fact that these parameters are not varied independently, we used membrane tension as the ‘knob’ in our experiment when trying to induce different morphologies. However, control of membrane tension in these experiments is not an exact procedure (as it is, for instance, in micropipette aspiration [5]).

Multi-component GUVs were formed in a 100 mM sucrose solution via heated electroformation ( $\sim 50$  C) to be above the phase separation temperature<sup>5</sup>. The electroformate containing the GUVs was then aliquoted into a number of glucose solutions that were within a few mOsm of the 100mM sucrose solution found inside the vesicles. For instance, the 100 mM sucrose electroformate might be diluted into aliquots of 96, 98, 100, 102, 104, 106, 108, and 110 mM glucose solutions at a dilution of  $\sim 1 : 100$  sucrose:glucose (v/v). A range of sugar dilutions, and hence a range of membrane tensions, is employed because precise control of the osmolar gradients between the inside and outside of the vesicle is not possible. This lack of fine osmolar control is due to measurement errors in the sugar concentrations at the millimolar level and more importantly there is evaporation occurring during the electroformation and handling that causes

---

<sup>5</sup>See the online protocol - <http://www.rpgroup.caltech.edu/lab/electroformation.pdf>

slight variations in sugar concentration. Each of these aliquots would then be examined under epi-fluorescence to determine which had yielded the proper osmolar gradient and membrane tension, as determined by the resulting morphologies (*i.e.* many aliquots have vesicle tensions too high to observe dimpling or budding).

Even with the composition controlled and the tension roughly dictated by the osmolar gradient, individual vesicle composition varies and the thermal history plays a part in the observed phase behavior. Key to observing the described morphologies is a degree of control over the thermal history of any one vesicle. Above the de-mixing transition temperature, the membrane is a homogeneous mix of the three molecular components and hence there are no domains. The precise conditions under which phase separation occurs have some variance from one preparation to another [16, 17], but once the transition has occurred we consistently observe the same types of domain morphologies and qualitative kinetics, as shown in Fig. 10. Using a custom built, electronically controlled microscope temperature stage, we were able to dynamically control the temperature of the sample. Our best results occurred when we ‘rapidly’ decreased the temperature ( $\sim -10$  K/min) through the transition temperature, but avoided the formation of a gel phase; the gel phase yields distinctly different morphologies and dynamics, a topic of interest on its own.

## 5 Error Introduced by the Curved Vesicle Surface

Giant unilamellar vesicles are an intrinsically curved surface, whose geometry leads to distortion of distance measurements in the image plane. Measurements of domain interaction are taken at the top or bottom of vesicles where the surface is nearly flat, and hence the measured distance is minimally distorted. However, we can estimate the severity of distance distortion by considering the error introduced by the curvature of the vesicle surface relative to the projected (*i.e.* 2D) image plane. The function  $f = \sqrt{R^2 - (x_1^2 + x_2^2)}$  is the hemi-spherical height function specifying the position of the vesicle surface relative to the flat image plane,  $R$  is the vesicle radius, and  $x_i$  are the Cartesian coordinates in the image plane. The distance between any two points on the vesicle surface is specified by the ‘great’ circle that connects those two points. This has a particularly simple interpretation in the case of a sphere; the geodesic is a circle that intersects the two points of interest and whose center is common with the sphere. Thus given two domains of interest, whose image plane positions are  $(x_1^{(j)}, x_2^{(j)})$ , we define their spherical unit vectors by

$$\hat{r}_j = \left[ \frac{x_1^{(j)}}{R}, \frac{x_2^{(j)}}{R}, \sqrt{1 - \left( \left( x_1^{(j)}/R \right)^2 + \left( x_2^{(j)}/R \right)^2 \right)} \right], \quad (189)$$

with the origin at the sphere’s center. The resulting geodesic distance on the vesicle surface is given by

$$l_{\text{act}} = R \cos^{-1}(\hat{r}_1 \cdot \hat{r}_2). \quad (190)$$

The error in distance measurement between any two points on the vesicle is

$$m = \frac{l_{\text{act}} - l}{l_{\text{act}}}, \quad (191)$$

where  $l$  is the measured distance (*i.e.* distance in the image plane), with the explicit formula

$$l = \sqrt{(x_1^{(1)} - x_1^{(2)})^2 + (x_2^{(1)} - x_2^{(2)})^2}. \quad (192)$$

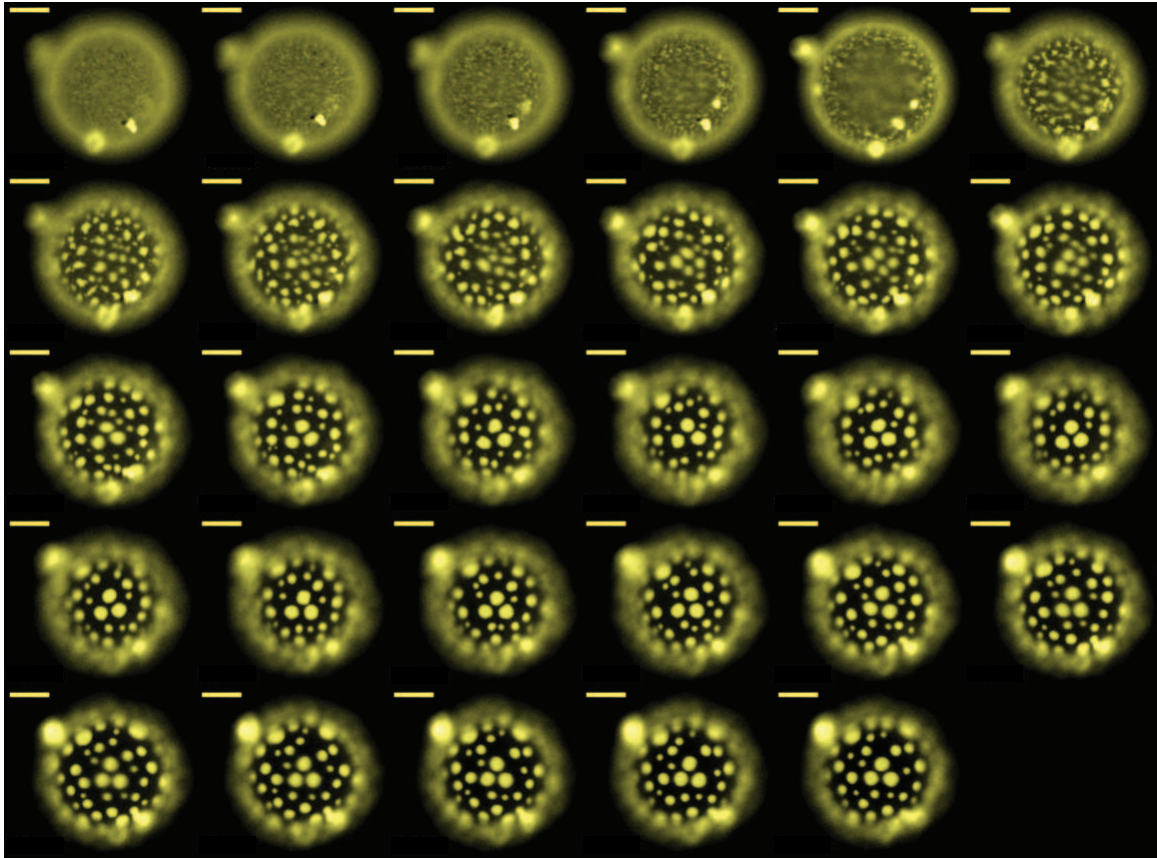


Figure 10: Lipid phase separation and domain formation. A multi-component GUV is driven through the de-mixing transition by a reduction in temperature to form discrete domains, via a process analogous to spinodal decomposition. The time between frames is 1.6 s. The domains are fluid, circular, and many are of the dimpled morphology. Due to the stochastic nature of their formation, the domains cover a range of sizes; the observed distribution of domain sizes persists (with the occasional coalescence event) on the time-scale of an hour or more, which is much longer than the minute time-scale for full phase separation on a higher tension GUV. The radial distribution function of domains on this vesicle would yield a measure of the potential of mean force between domains. The scale bars are  $10\mu\text{m}$ .

For the purposes of estimation and formulaic simplicity, we derive a simple formula for the error as measured from the projected vesicle center, where we use the azimuthal symmetry and integrate the error explicitly to find

$$m = 1 - \frac{l/R}{\cos^{-1} \left( \sqrt{1 - \left( \frac{l}{R} \right)^2} \right)} \simeq \frac{1}{6} \left( \frac{l}{R} \right)^2. \quad (193)$$

The dimensionless quantity  $l/R \in [0 \dots 1]$  quantifies how far a domain is from the projected vesicle center. The maximum possible error occurs when we measure from the image plane center to a point on the equator of the sphere ( $l/R = 1$ ), resulting in an underestimate of  $\sim 36\%$  (exactly  $1 - 2/\pi$ ) in the measured distance. If we demand that at most a 10% error in distance measurement is acceptable, this constrains our measurements to be within a circle of radius  $l/R \simeq 0.71$ . This calculation gives an estimate of the error in distance measurement, but in reality, the exact error introduced by the surface curvature is a complicated function of the precise positions of each domain relative to the center of the spherical vesicle.

Let us do a sample calculation to make a more concrete connection to our experiments. Given a nominal vesicle size of  $R = 15\mu\text{m}$ , we should be able to measure out to approximately  $l = 10.6\mu\text{m}$  from the projected vesicle center with an error in distance measurement of less than 10%. On the surface of the sphere, this maximum allowed  $l$  would correspond to a change in the vesicle height of  $\sim 4.4\mu\text{m}$ . The depth-of-field of our 20x objective is about  $\sim 4\mu\text{m}$  (a 4x multiplier tube on the camera effectively increases the magnification to 80x without changing the depth-of-field).

Our domain tracking software was written to reject domains which appeared out of focus and/or distorted from a circle, as discussed in section 7. Hence, if we ensure that the top (or bottom) of the vesicle is in focus, domains which break our 10% error condition are rejected. The exact numbers will change with different sized vesicles, but due to the fact that a larger vesicle is relatively flat over a larger area, this model calculation shows that for any vesicle  $R \gtrsim 15\mu\text{m}$  our software automatically rejects domains that do not meet the error criteria.

## 6 *In vitro Selection and Representative Data*

In this section, we describe: how we chose vesicles for data collection and analysis, some of the common problems with selecting vesicles and collecting data, and the generic quality of collected data.

After the formation of multi-component GUVs, the raw solution of vesicles is diluted in an osmolar-balanced glucose solution to roughly regulate the membrane tension, as discussed in section 4. A viewing chamber is created using two #1 cover-slips with an O-ring between them, loaded with  $\sim 135\mu\text{l}$  of the osmolar balanced vesicle solution. Small density gradients between the glucose outside and sucrose inside the vesicles sediment them toward the bottom of the chamber, where the dilution ratio is adjusted such that there is a single, sparse layer of vesicles (*i.e.* no stacked vesicles). In all the data shown here, the vesicles were close to the glass substrate (roughly within a vesicle radius), but had a small  $z$ -displacement between the substrate and the lower focal plane of the vesicle, indicating that the vesicles were not resting directly on the substrate. At approximately 1 cm in diameter, the viewing chamber is small enough that we can scan the entire chamber, examining hundreds of vesicles relatively quickly.

Within a single field of view we look for vesicles that meet the following criteria:

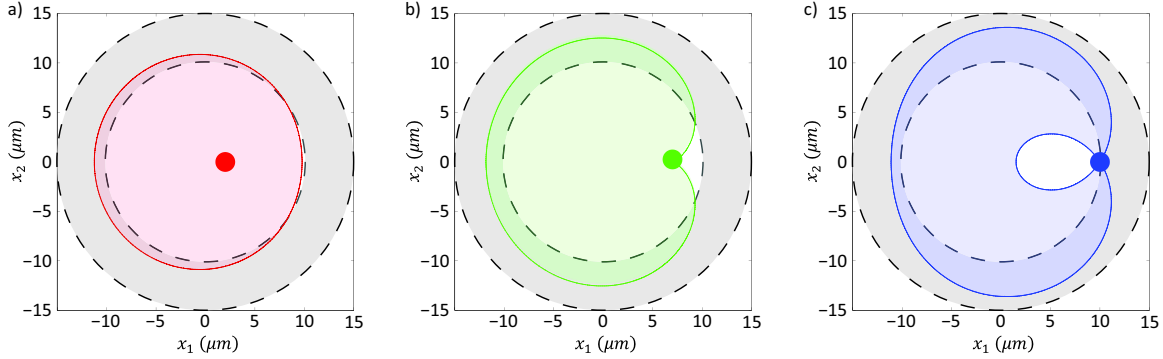


Figure 11: Examining spatial regions of acceptable distance measurement error. In all plots, the outer dashed line shows the projected equator of a vesicle with  $R = 15 \mu\text{m}$ , and the region defined by the inner dashed line is where the depth-of-field of the objective will show domains in focus; the grey region will be out of focus. In all plots, the domain radius is  $r = 1 \mu\text{m}$ . a) A domain is placed at  $x_1 = 2 \mu\text{m}$  and  $x_2 = 0 \mu\text{m}$ ; other domains that lie inside the red region have a measured distance error of less than 10%. b) A domain is placed at  $x_1 = 7 \mu\text{m}$  and  $x_2 = 0 \mu\text{m}$ ; other domains that lie inside the green region have a measured distance error of less than 10%. c) A domain is placed at  $x_1 = 10 \mu\text{m}$  and  $x_2 = 0 \mu\text{m}$ ; other domains that lie inside the blue region have a measured distance error of less than 10%. In (b) and (c) the smaller white regions indicate regions of measurement error greater than 10%.

- Vesicle size needs to be large enough that we can clearly resolve domains, given the optical limits of the microscope, and large enough that there is an appreciable area of the vesicle at the top or bottom where we can approximate the surface as flat (see section 5). This usually corresponds to vesicles with a radius greater than  $\sim 10 \mu\text{m}$ .
- Vesicles need to be ‘clean’, by which we mean the vesicle itself does not have any obvious tubes, protrusions, or internal structures attached to it, nor should it have other vesicles nearby obstructing the view of the image plane or excessively polluting the image with light from outside the image plane.
- While we have recorded vesicles with domains of a wide distribution of sizes, we prefer vesicles whose domain sizes are in a narrower range, usually with a standard deviation half the mean size. In cases where we want to observe many closely interacting domains, or disperse domains, the interaction potentials tend to be less noisy the narrower the distribution of domain sizes. See the following paragraphs and subsection 3.2 for more discussion of domain size asymmetry.
- Slight thermally-driven fluid flows in the chamber can cause vesicles to drift in the image plane, and beyond a certain drift speed ( $\sim 10 \mu\text{m}/\text{s}$ ) it becomes impractical to follow even the best vesicles that meet the above criteria. That said, most vesicles are quite stationary in the image plane, with drift speeds of only a few microns per minute.

Figure 12 shows a typical microscope view from which vesicles would be chosen for data collection, and subsequent analysis.

Rather than offer our own subjective interpretation of data quality, we present a subset of the 29 total data sets that have a relatively low areal density of domains, showing the range

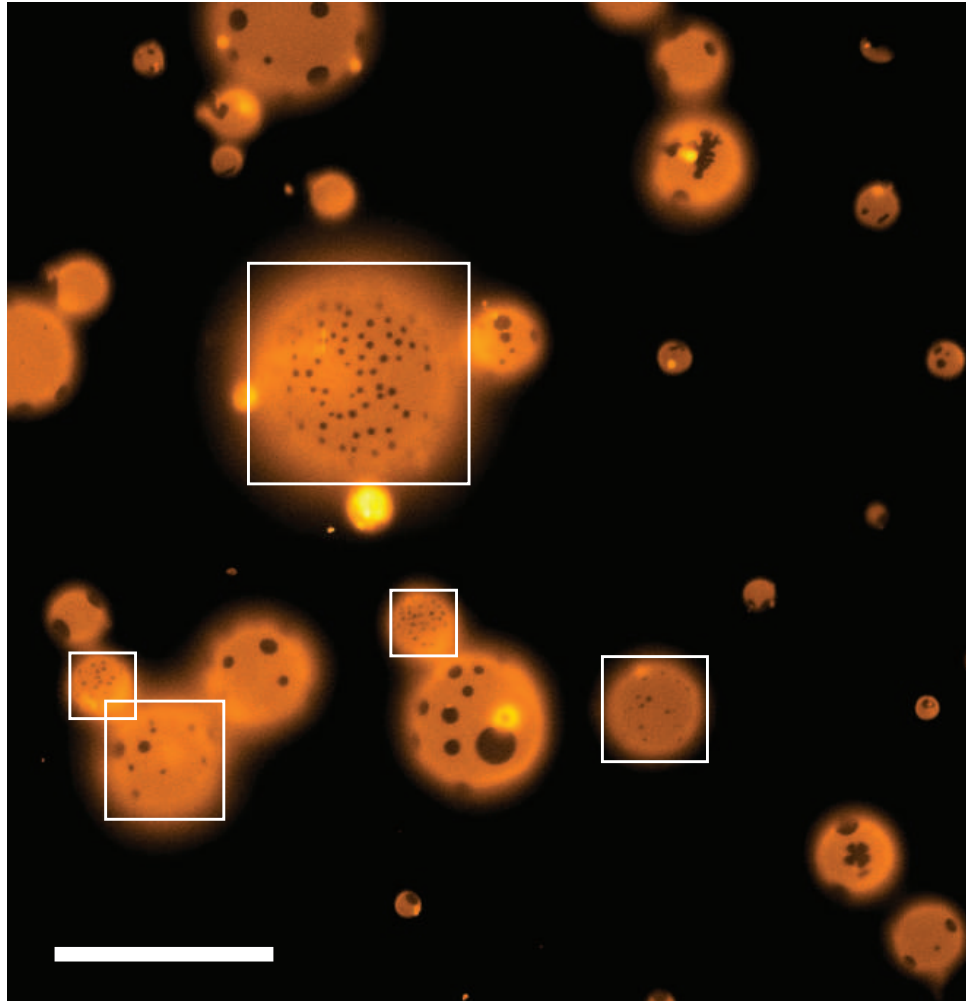


Figure 12: A typical view of phase-separated GUVs in the TRITC fluorescence channel. This field of view is at 20X magnification, though most measurements were taken at 80X. This particular combination of field of view and membrane compositions shows dark domains in a light surrounding membrane. The white squares outline vesicles from which data would likely be collected. The scale bar is  $50\ \mu\text{m}$ .

from very poor data sets up to what we consider very good data sets. We classify a good data set solely in terms of the noise characteristics of the interaction potential. Data sets with low noise, whose potentials are relatively smooth, have well-resolved features and are considered to be of the highest quality. Generally, the noise is related to the chosen spatial resolution of the potential; increased spatial resolution decreases the number of events in each bin of the histogram and hence lowers the signal to noise ratio. Higher levels of noise in the interaction potential also arise from a vesicle whose domains have a widely varying size distribution, as demonstrated in Fig. 15. The qualitative explanation of the correlation between increasing width of the domain area distribution and increasing noise in the measured potentials is as follows: if all domains are the same size, then the pairwise potential describing the interaction between each unique domain pair has the same scaling factor (*i.e.* eqn. 175), and hence each measurement of a pairwise distance is essentially sampling from the same underlying distribution, thus the signal to noise ratio is high. On the other hand, if all the domains are different sizes, the scaling factors of the potentials associated with each unique domain pair are different, hence each measurement of a pairwise distance is sampling from the distribution describing only that pair's interaction. All those measurements, describing distinct pairwise interactions, are then combined to form the potential of mean force, however, being made up of a large number of slightly different pairwise potentials, the potential of mean force has lower signal to noise.

The only degree of subjectivity that we will add is a classification system where data sets will be put into one of three categories according to the quality of their interaction potentials: good (Fig. 13), fair (Fig. 14) and poor (Fig. 15). In the following figures we give two examples of each type of data set, and state how many data sets fall within each classification. For each data set we show a plot of the raw, uncorrected histogram of domain positions, the raw and corrected potentials resulting from that histogram, a histogram of the number of domains found in each frame, and a histogram of the identified domain areas. A clear correlation exists between vesicles whose domains have a wide size distribution and interaction potentials with higher noise, as demonstrated in the figures.

## 7 Domain Tracking and Data Analysis

Having established that we can measure distances between domains in the image plane to within a reasonable error tolerance, we are in a good position to begin transforming images into quantitative data. After a suitable vesicle has been chosen, images are collected in the form of 16 bit TIFF stack image files. Each stack contains  $\sim 500$  to 1500 frames collected at a rate such that diffusion allows the domains to explore their local configuration space during the course of the video - a typical time scale is 50 - 200 ms between frames. If the domain density is approximately constant during the stack collection, then the system is in quasistatic equilibrium, and time ordering of the frames is not necessary. Thus any software that identifies domains need only calculate the distances between domains in each frame, and combine data from all frames to construct a radial distribution function for the entire stack - tracking domains through time gives no additional information for the purposes of our measurement.

Regarding the ‘nuts-and-bolts’ level of image processing required to construct the radial distribution function, each image progresses through three phases of processing: i) background removal and contrast adjustment, ii) edge detection and brightness filtering, and iii) morphological selection. Each of these phases has a number of parameters that may be tuned to best fit a particular data set. The rest of this section discusses each phase in some detail.

It is often easier to process data sets where the vesicles are stationary and closely cropped

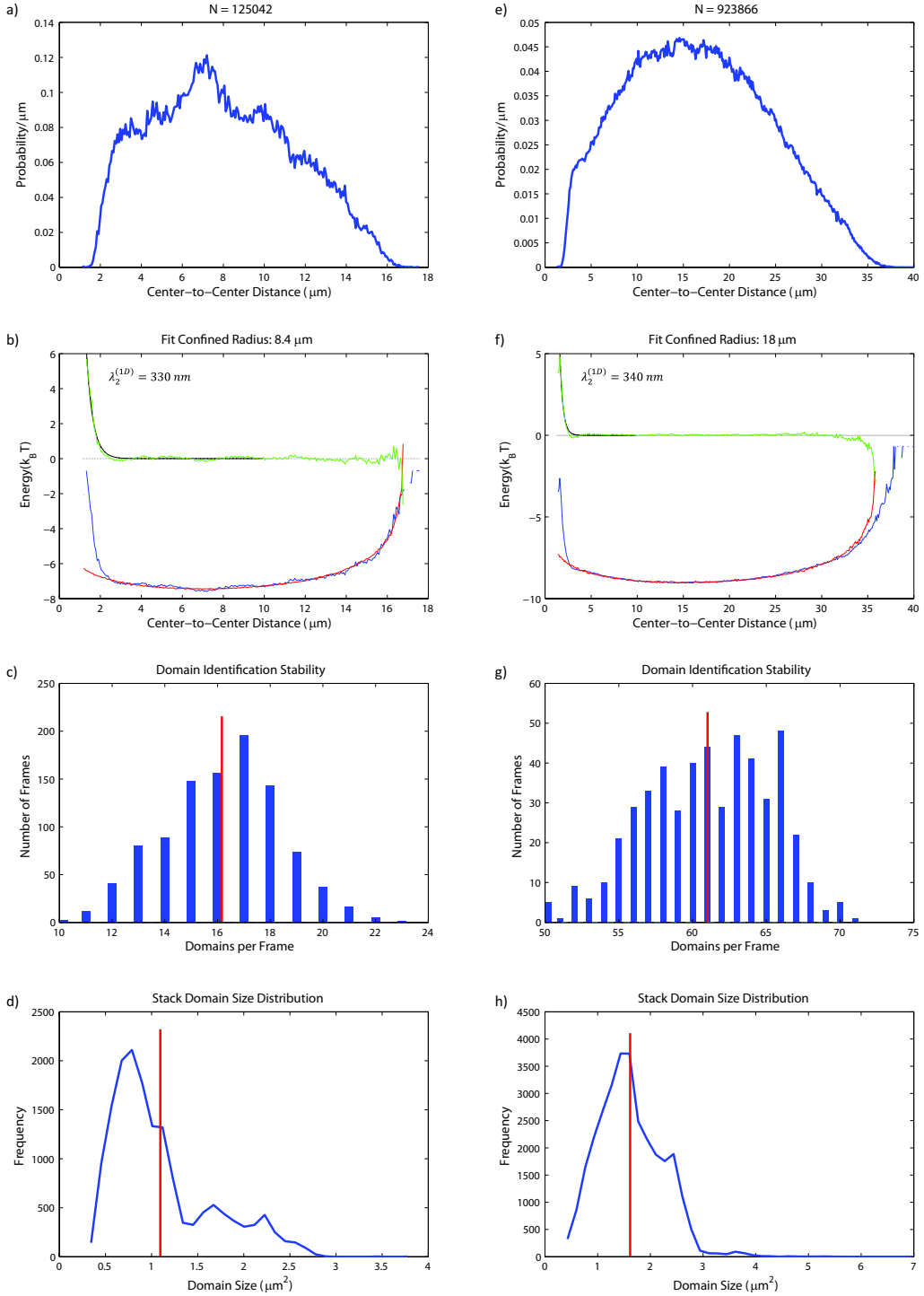


Figure 13: Representative ‘good’ quality domain interaction data. Each column represents a unique ‘good’ quality data set, in total 12 of 29 data sets. Plots (a) and (e) show the raw distribution of domain distances, where  $N$  is the total number of unique distances measured. Plots (b) and (f) show the raw (blue), fictitious (red), and corrected (green) potential of mean force. The black line is a fit to eqn. 170, with the length scale indicated on the graph, corresponding to  $\tau \simeq 2 \times 10^{-4} k_B T/\text{nm}^2$  with  $\kappa_b = 25 k_B T$ . Plots (c) and (g) are histograms of the number of domains identified in each frame. Plots (d) and (h) are the distribution of domain areas throughout the stack. In (c), (d), (g) and (h) the red line is the mean.

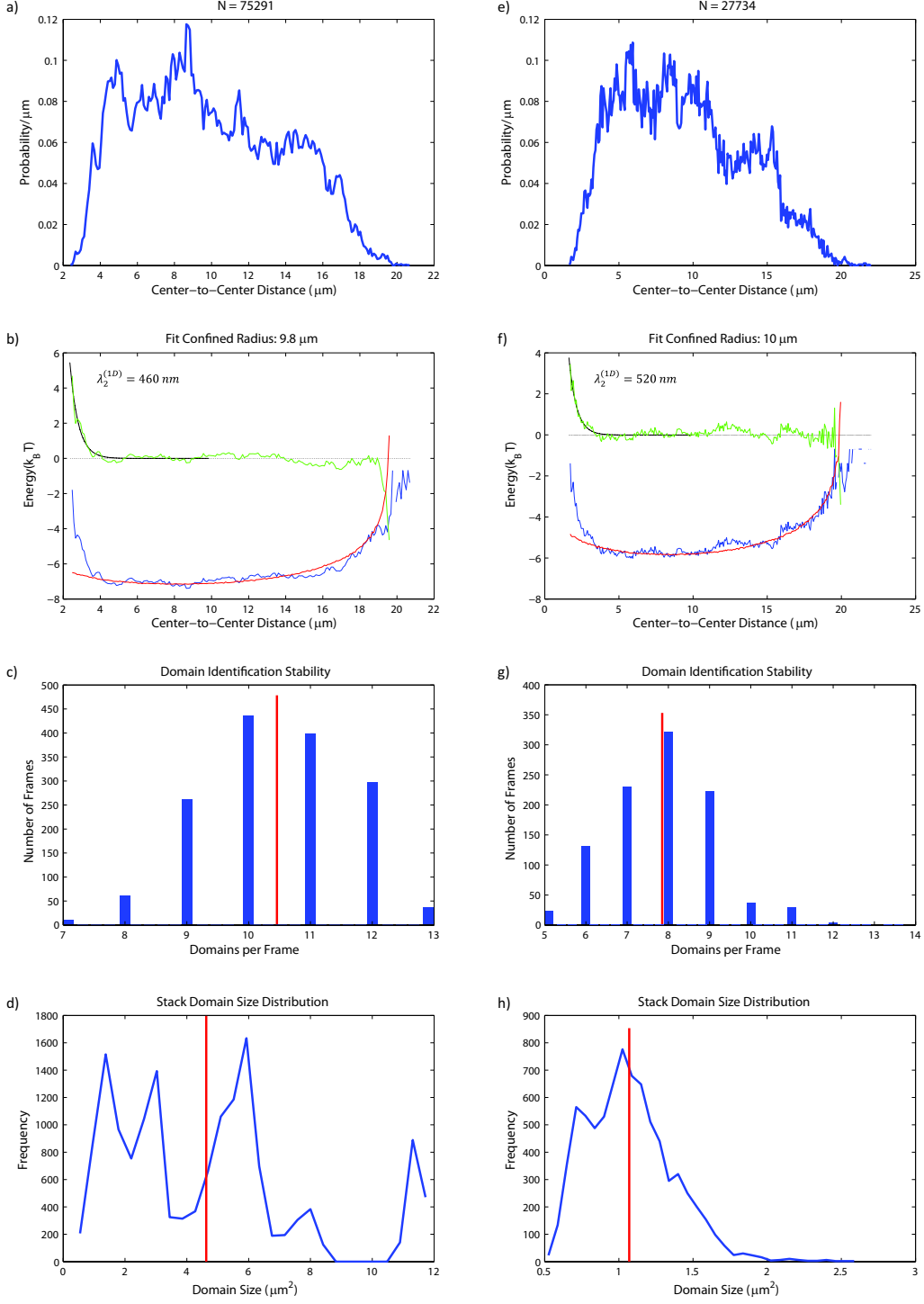


Figure 14: Representative ‘fair’ quality domain interaction data. Each column represents a unique ‘fair’ quality data set, in total 6 of 29 data sets. Plots (a) and (e) show the raw distribution of domain distances, where  $N$  is the total number of unique distances measured. Plots (b) and (f) show the raw (blue), fictitious (red), and corrected (green) potential of mean force. The black line is a fit to eqn. 170, with the length scale indicated on the graph, corresponding to  $\tau \simeq 1 \times 10^{-4} k_B T/\text{nm}^2$  with  $\kappa_b = 25 k_B T$ . Plots (c) and (g) are histograms of the number of domains identified in each frame. Plots (d) and (h) are the distribution of domain areas throughout the stack. In (c), (d), (g) and (h) the red line is the mean.

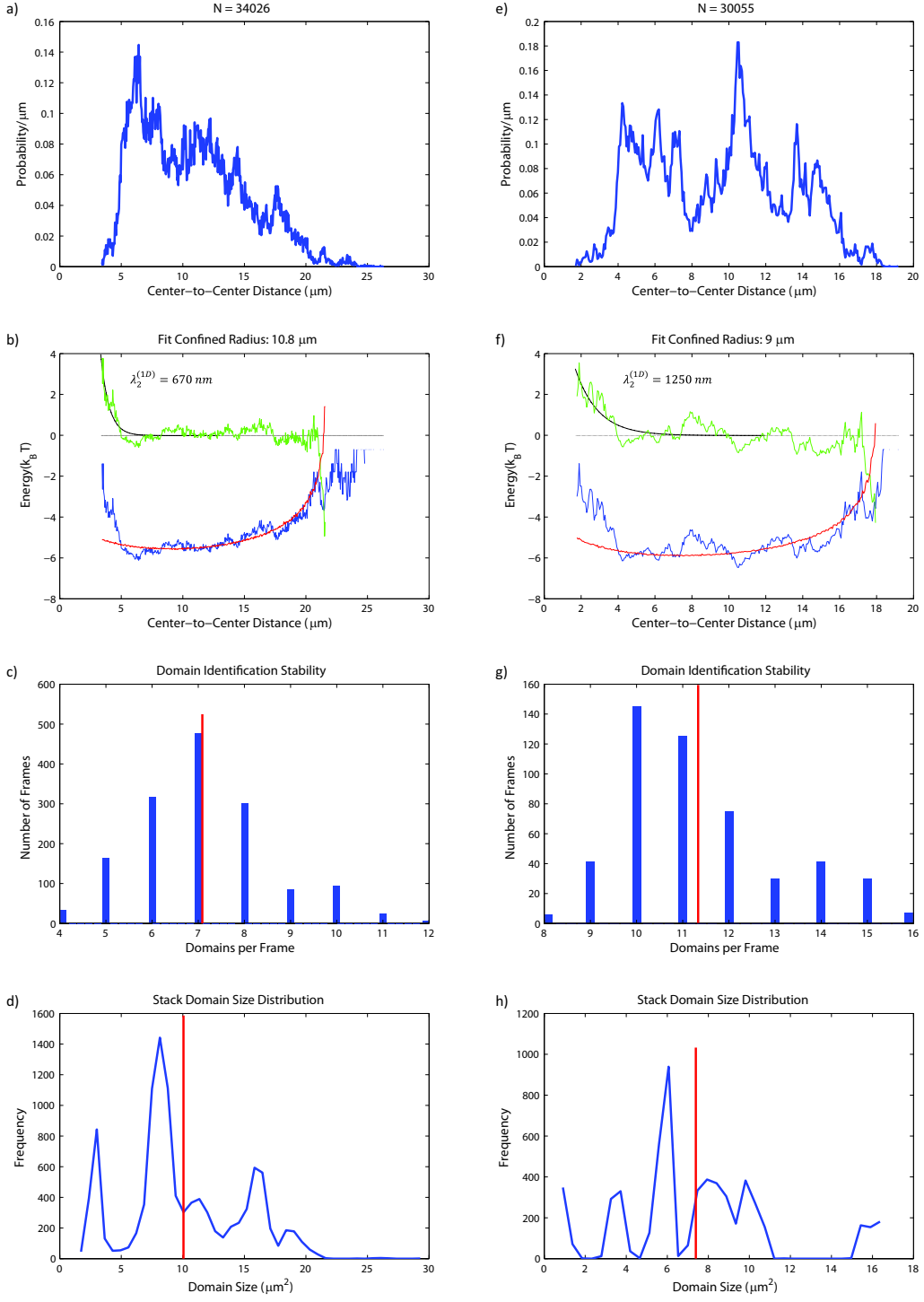


Figure 15: Representative ‘poor’ quality domain interaction data. Each column represents a unique ‘poor’ quality data set, in total 11 of 29 data sets. Plots (a) and (e) show the raw distribution of domain distances, where  $N$  is the total number of unique distances measured. Plots (b) and (f) show the raw (blue), fictitious (red), and corrected (green) potential of mean force. The black line is a fit to eqn. 170, with the length scale indicated on the graph, corresponding to  $\tau \simeq 4 \times 10^{-5} k_B T/\text{nm}^2$  with  $\kappa_b = 25 k_B T$ . Plots (c) and (g) are histograms of the number of domains identified in each frame. Plots (d) and (h) are the distribution of domain areas throughout the stack. In (c), (d), (g) and (h) the red line is the mean.

to the total image size. We wrote a separate piece of software that translates a vesicle to be stationary in time - many data sets require such alignment.

Background removal and contrast adjustment are not required to process a stack, however, they help compensate for brightness changes due to photo-bleaching, and can enhance contrast between a domain and its background, thereby making edges easier to find. For each data set, we employ one of two methods. The first method, which is more manual but generally yields better results, is outlined in Fig. 16. The second method is more automated, using so-called ‘adaptive’ contrast adjustment, briefly:

- a square tile size of  $n \times n$  pixels is chosen such that the tile fully encompasses a domain and its local background
- the image is divided into regions of that tile size and the contrast in each region is enhanced according to standard histogram equalization
- each tile is then bilinearly interpolated with the neighboring tiles to prevent fictitious edges

In regions of the image where no domain is present, the adaptive contrast adjustment enhances the noise, but such regions neither pass the brightness nor morphological criteria. The tile size is the only user-specified parameter in this stage of domain tracking. The contrast-adjusted image from either method is then passed onto the second stage of the algorithm - edge detection and brightness filtering.

The well-known and robust *Canny* edge detection algorithm [18], as implemented in MatLab<sup>©</sup>, is used to find domain edges in the contrast-adjusted images, whether the domains are bright in a dark background or dark in a bright background. The edge detection algorithm requires three user-specified parameters to find edges, however those parameters need little tuning between data sets. Our software only examines ‘connected’ objects as potential domains, thus if an edge is found it must topologically make a circle to be examined further. Once the edge detection has found a topologically circular element, it examines that element to determine if it has the correct general brightness features - for instance, a light domain in a dark background should be brighter at its center than in the transition zone at the domain edge. The user specifies a cut-off for the ratio of the edge-to-center brightness, thereby allowing the edge detection algorithm to be promiscuous in what edges it detects and connects into circles. Those circular elements are then checked against the relevant edge-to-center brightness cut-off; only connected objects that meet the criterion are queried in the next stage for their morphological properties.

Once topologically circular objects have been found that meet the brightness criterion, they must also have roughly the correct shape, namely a circle. There are many ways to measure how much a given shape deviates from a circle; our software uses the dimensionless measure of the square of the perimeter length divided by the area,  $\ell_{\text{perim}}^2/4\pi A$ . Using this measure a perfect circle has a value of 1, and higher values correspond to less circular objects. The user specifies a cut-off above which the object is rejected. There are two main reasons why a domain might appear acircular. First, it could be that the domain is in focus but is near the vesicle equator, and hence lies in a region where its projection is elliptical and thus our distance measurement error is too high. Second, it could be that the domain is partially out of focus, such that the point-spread-function of the microscope warps the shape into something acircular. These domains would not have a well-defined center, and hence might also break our error tolerance criterion. For domains near the equatorial regions of the vesicle, these effects often occur simultaneously. The final morphological criterion is that any putative domain must lie within a certain reasonable size range, the minimum and maximum of which is specified by the

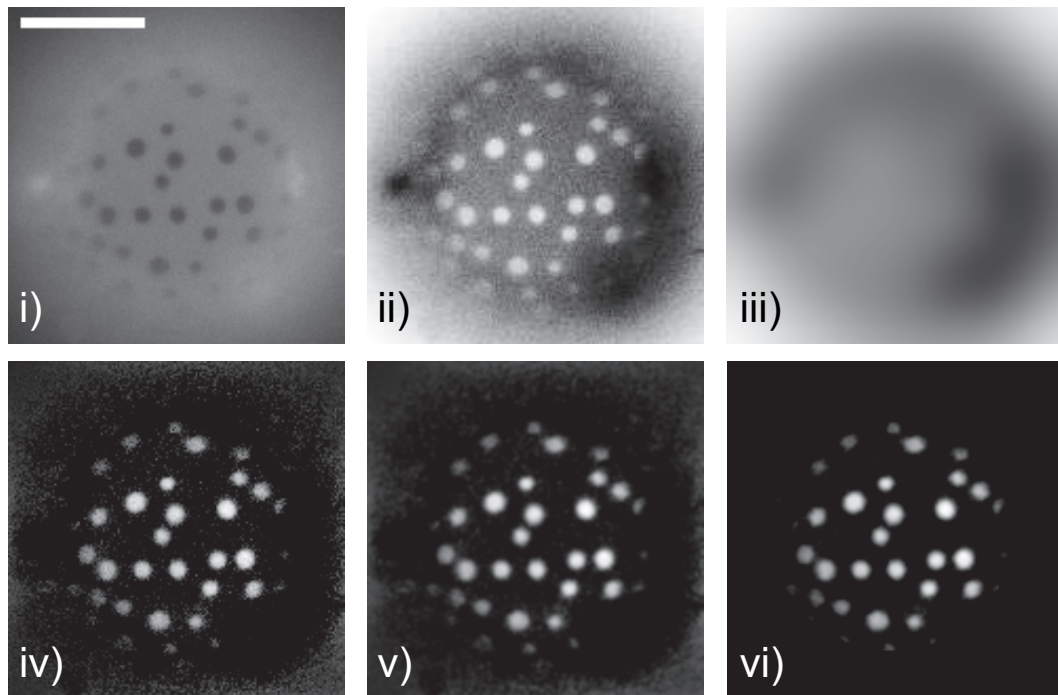


Figure 16: Example of manual background removal and contrast adjustment. i) The raw fluorescence image; in this case dark domains in a light background, but the method also applies to reverse contrast vesicles. ii) Inverted (i) and contrast maximized by 0.5% histogram thresholding. iii) Gaussian blur of (ii) using a 30 pixel radius. iv) Subtraction of (iii) from (ii), essentially removing background and increasing the signal-to-noise of the domains. v) Gaussian blur of (iv) using a 1 pixel radius - this decreases high frequency noise that can trigger the edge detection algorithm without sacrificing spatial resolution. vi) Finally, spatially irrelevant intensities are removed and the stack contrast is adjusted. The scale bar is  $20 \mu\text{m}$ .

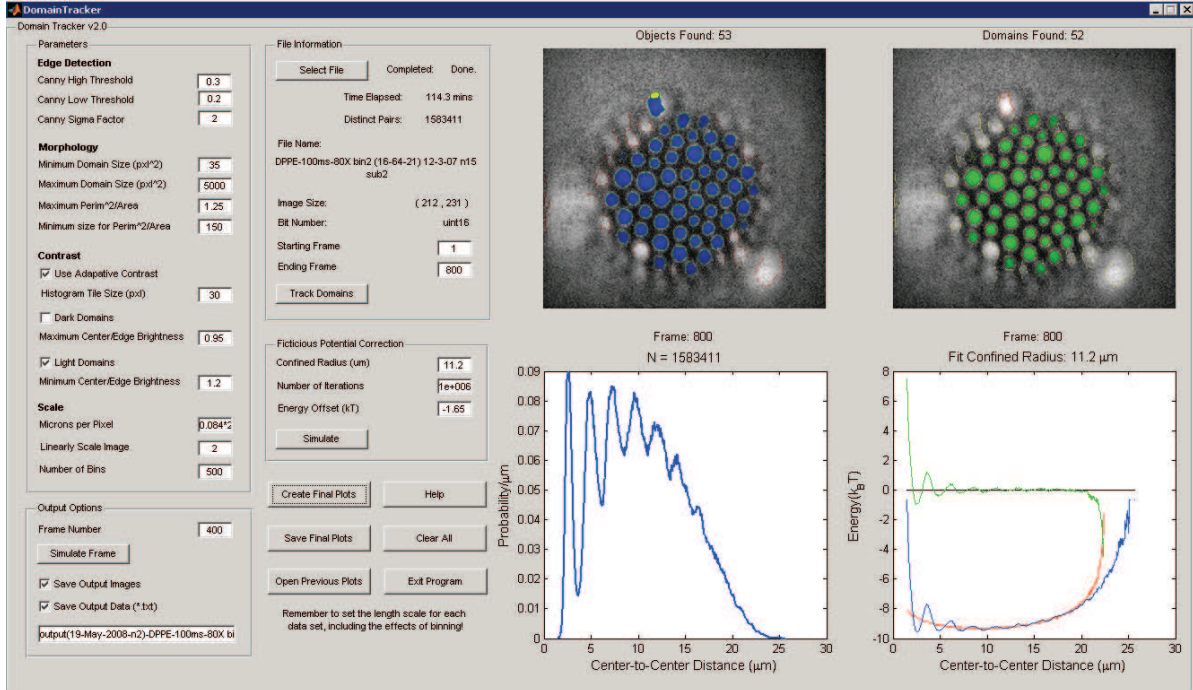


Figure 17: Screen shot of the domain tracking software. Parameters for contrast adjustment, edge detection, brightness, and morphological criteria are entered on the left. The top left graph shows connected-edge objects that have met the brightness criterion in blue (failed in yellow). The top right graph shows in green the subset of blue objects which have also met the morphological criteria. The lower left graph is the radial distribution function for the entire stack. The lower right graph is the natural logarithm of that probability distribution (in blue), the simulated fictitious potential (in red), and their difference - the potential of mean force (in green).

user. For instance, a putative domain with an area of only a few pixels or an area approaching the size of the entire vesicle would likely be rejected for being too small or too large, respectively.

Any object that has passed through these three stages is then considered a well-resolved domain. Each domain's center is then identified by a simple first-moment calculation, and the centers are used to calculate the pairwise distances in each image. The pairwise distance data from the entire stack is then combined and binned into a probability distribution for the separation of two domains. The natural logarithm of that probability distribution is then the potential of mean force between domain pairs. Figure 17 shows a screen-shot of the program after a data set has been processed.

## 7.1 The Fictitious Confining Potential

Extracting the interaction energy from the statistical distribution of distances between domains is not entirely straightforward. As we have just shown, we can reasonably assume that the surface is flat in our measurements, and hence the actual distances we measure are not severely distorted. However, there is also an effect coming from the circular geometry of our measurement. More specifically, all of the domains the software detects are confined to lie in a circle of some

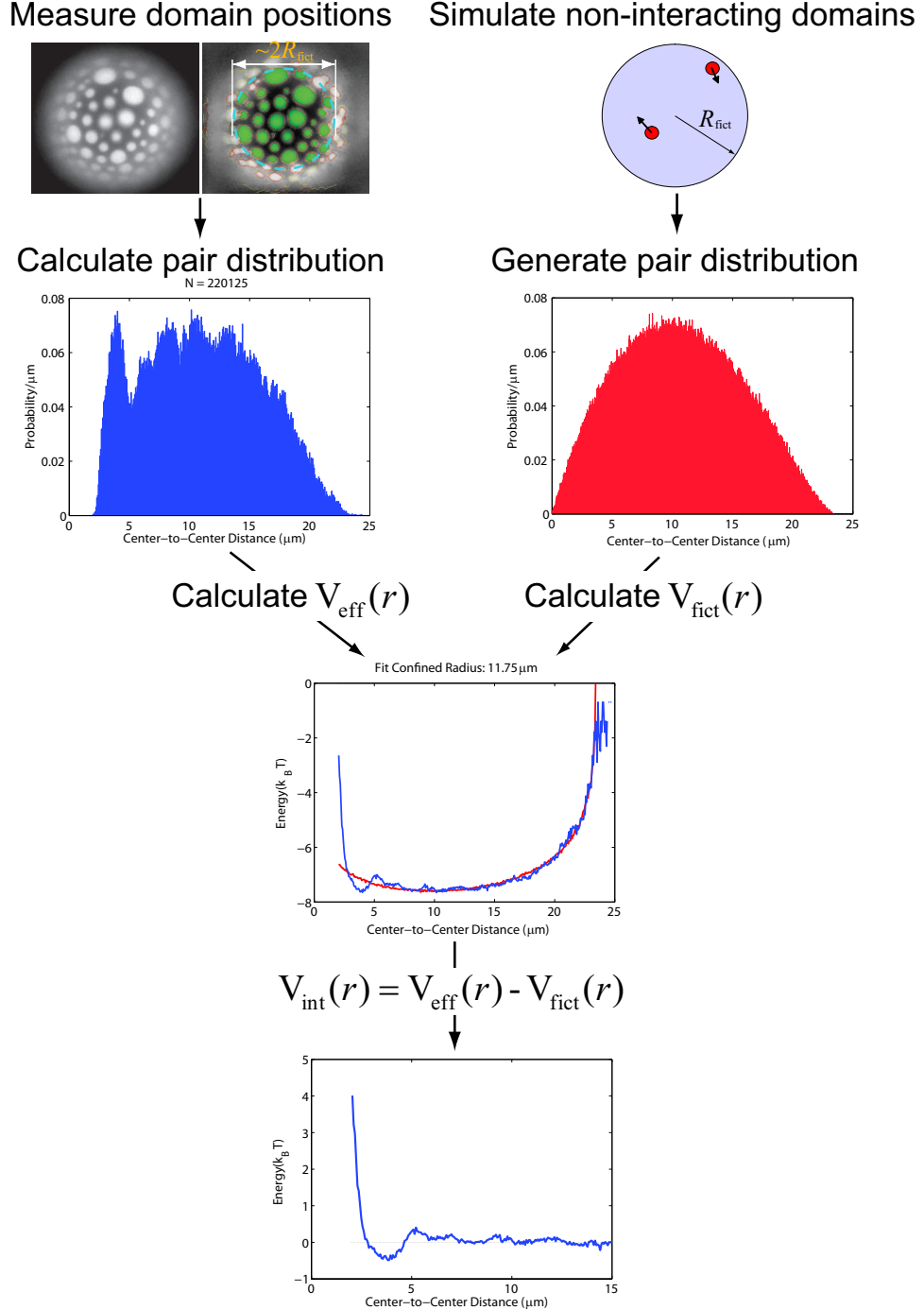


Figure 18: Flow diagram explaining how the fictitious potential is removed from measured data. The positions of well-resolved domains are measured, the radial distribution function is generated, and the effective potential between the domains is calculated as the blue line. Simultaneously, the radial distribution function for two non-interacting domains in a user-defined circle of radius  $R_{\text{fict}}$  is generated, and the corresponding fictitious potential is calculated as the red line. Subtracting the fictitious potential from the effective potential leaves only the potential of mean force,  $V_{\text{int}}(r)$ . Intervals of  $r$  with very low statistics are excluded.

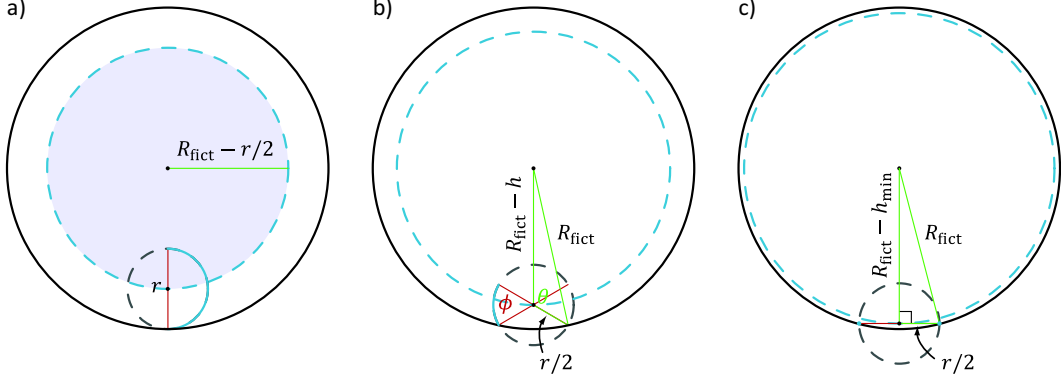


Figure 19: Geometric relationships for the analytical calculation of the fictitious potential. a) This schematic shows the first contribution to the density of states,  $P_1(r)$ . Two points separated by a distance  $r$ , as shown by the red line, sweep out  $\pi$  radians for every point in the gray region, contributing a statistical weight proportional to the product of the area of the gray region and the length of the solid blue line. b) This schematic shows the second contribution to the density of states,  $P_2(r)$ . If the points lie outside of the gray region in (a), the density of states for a given value of  $h$  is proportional to the product of the length of the dashed blue line and the solid blue line. Then all such contributions for  $h \in [h_{\min} \dots r/2]$  must be summed. c) This schematic shows the geometric origin of the minimum height,  $h_{\min}$ , as a function of the separation  $r$ .

effective radius ( $R_{\text{fict}}$ ), smaller than the radius of the vesicle ( $R$ ). This means that any two domains we detect will be maximally separated by  $2R_{\text{fict}}$ . When making a histogram of the pairwise distance data, we never detect two domains farther apart than this distance, and thus it appears there is a strong confining potential keeping all domains within  $2R_{\text{fict}}$  of each other. The actual interaction energy we measure is the sum of this fictitious confining potential,  $V_{\text{fict}}(r)$ , and the real interaction potential,  $V_{\text{int}}(r)$ ,

$$V_{\text{eff}}(r) = V_{\text{int}}(r) + V_{\text{fict}}(r). \quad (194)$$

The fictitious confining potential can be easily simulated via Monte Carlo methods. Given a circle of radius  $R_{\text{fict}}$ , we generate a uniform distribution of points within the circle and calculate the radial distribution function as shown in the upper right of Fig. 18. The negative natural logarithm of this distribution is  $V_{\text{fict}}(r)$ . All that remains is to pick a proper  $R_{\text{fict}}$  for a given data set; that is, to isolate the correct interaction potential there is one fit parameter for each data set. An example of processed data is shown in Fig. 18.

### 7.1.1 The Geometric Derivation

Given certain constraints of our analysis software, it is often quicker to generate the fictitious potential via Monte Carlo methods, though in this section we will show a geometric derivation that leads to a closed form expression for the fictitious potential. A key result is that the fictitious potential for any value of  $R_{\text{fict}}$  is simply a scaled version of the same underlying function.

As we have shown previously, the measured potential of mean force is the sum of the interaction potential and the fictitious potential, which, in terms of the underlying probability distributions can be written as

$$V_{\text{eff}}(r) = -\ln [P_{\text{int}}(r) \cdot P_{\text{fict}}(r)], \quad (195)$$

where the distribution  $P_{\text{fict}}(r)$  is somehow related to the geometry of the space available to two non-interacting domains, essentially ‘counting’ up the number of states with a separation  $r$ . This geometric relationship can be found exactly for a circle as follows. First, consider two points a distance  $r$  apart connected by a line segment, whose center lies at some position inside the circle defined by  $(R_{\text{fict}} - r/2)$  as shown in Fig. 19a. For every point inside this region we can rotate the line segment about its center point to find the density of states with separation  $r$ , where the rotation is restricted to  $\pi$  radians to avoid double counting. We refer to this contribution to  $P_{\text{fict}}(r)$  as

$$P_1(r) = \underbrace{\frac{\pi}{2} \cdot \frac{r}{2}}_{\text{rotation}} \cdot \underbrace{\pi \left(R - \frac{r}{2}\right)^2}_{\text{region area}}. \quad (196)$$

For those states with separation  $r$  whose connecting line segment has its center outside the region defined by  $(R_{\text{fict}} - r/2)$  not all rotations of the line segment are available. Referring to Fig. 19b, the rotation of the line segment is now defined by the angle  $\phi$ , which depends on the distance,  $h$ , from the outer circle,  $R_{\text{fict}}$ . Determining this angle is then only a matter of geometry, where using the law of cosines and the fact that  $\phi = 2\theta - \pi$ , one finds

$$\phi(\bar{r}, \bar{h}) = 2 \cos^{-1} \left[ \frac{(1 - \bar{h})^2 + (\bar{r}/2)^2 - 1}{\bar{r}(1 - \bar{h})} \right] - \pi, \quad (197)$$

where for ease of notation we now define  $\bar{r} = r/R_{\text{fict}}$  and  $\bar{h} = h/R_{\text{fict}}$ . Then for each value of  $h$  the density of states with rotation  $\phi$  and separation  $r$  is simply the product of  $r/2$ , the angle  $\phi$ , and the circumference of the circle defined by  $(R_{\text{fict}} - h)$ , as shown by the dashed blue line in Fig. 19b. Summing these contributions for all available values of  $h$  we find the second contribution to  $P_{\text{fict}}(r)$ ,

$$P_2(r) = \int_{h_{\min}(r)}^{\frac{r}{2}} \underbrace{2\pi(R_{\text{fict}} - h)}_{\text{circumference}} \underbrace{\frac{r}{2} \phi(r, h)}_{\text{rotation}} dh. \quad (198)$$

For a given value of  $r$  there is some value of  $h$  below which there are no available states, or in other words  $\phi = 0$ , as shown in Fig. 19c. This value can be found by solving  $\phi = 0$  for  $\bar{h}$  giving

$$\bar{h}_{\min} = 1 - \sqrt{1 - \left(\frac{\bar{r}}{2}\right)^2}. \quad (199)$$

Then the total density of states for a separation  $\bar{r}$  is given by the sum

$$P_{\text{fict}}(\bar{r}) = \frac{1}{a} (P_1(\bar{r}) + P_2(\bar{r})) = \frac{\pi R_{\text{fict}}^3}{a} \left[ \pi \frac{\bar{r}}{2} \left(1 - \frac{\bar{r}}{2}\right)^2 + \int_{\bar{h}_{\min}}^{\frac{\bar{r}}{2}} (1 - \bar{h}) \bar{r} \phi(\bar{r}, \bar{h}) d\bar{h} \right], \quad (200)$$

where  $a$  is a normalization constant defined by

$$a = \pi R_{\text{fict}}^3 \int_0^2 \left[ \pi \frac{\bar{r}}{2} \left(1 - \frac{\bar{r}}{2}\right)^2 + \int_{\bar{h}_{\min}}^{\frac{\bar{r}}{2}} (1 - \bar{h}) \bar{r} \phi(\bar{r}, \bar{h}) d\bar{h} \right] d\bar{r}. \quad (201)$$

Then finally, the properly normalized distribution is

$$P_{\text{fict}}(\bar{r}) = \nu \left[ \pi \frac{\bar{r}}{2} \left(1 - \frac{\bar{r}}{2}\right)^2 + \int_{\bar{h}_{\min}}^{\frac{\bar{r}}{2}} (1 - \bar{h}) \bar{r} \phi(\bar{r}, \bar{h}) d\bar{h} \right] \quad (202)$$

where  $\nu \simeq 2.4675$  and  $P_{\text{fict}}(r) = P_{\text{fict}}(\bar{r})/R_{\text{fict}}$ . Fig. 20 compares this analytical result to the fictitious radial distribution function generated by Monte Carlo methods, showing excellent agreement between the two methods. Additionally, this analytical result shows that the fictitious radial distribution function for any value of  $R_{\text{fict}}$ , is simply a scaled version of  $P_{\text{fict}}(\bar{r})$ .

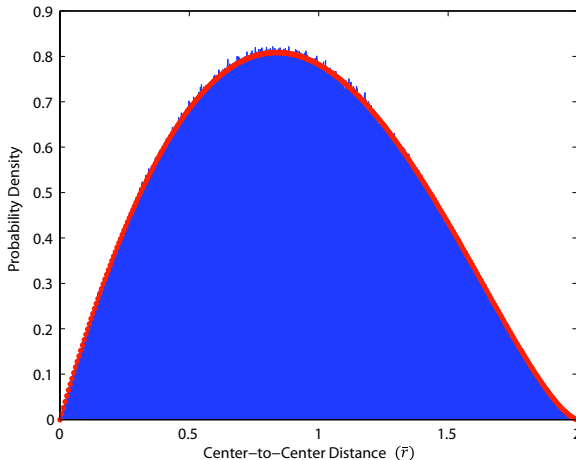


Figure 20: Comparison of the fictitious radial distribution function from analytical and Monte Carlo methods. The fictitious radial distribution function generated by Monte Carlo methods is shown in the blue histogram, while the distribution calculated from  $P_{\text{fict}}(\bar{r})$  is shown by the orange points, both plotted as a function of the point separation  $\bar{r}$ .

## References

- [1] Lipowsky R (1992) Budding of membranes induced by intramembrane domains. *J Phys II France* 2:1925–1840.
- [2] Sens P, Turner MS (2006) Budded membrane microdomains as tension regulators. *Phys Rev E* 73:031918.
- [3] Harden JL, Mackintosh FC, Olmsted PD (2005) Budding and domain shape transformations in mixed lipid films and bilayer membranes. *Phys Rev E* 72:011903.
- [4] Boal D (2002) *Mechanics of the Cell*. Cambridge University Press, 1st edition.
- [5] Rawicz W, Olbrich KC, McIntosh T, Needham D, Evans E (2000) Effect of chain length and unsaturation on elasticity of lipid bilayers. *Biophys J* 79:328–39.
- [6] Huang HW (1986) Deformation free energy of bilayer membrane and its effect on gramicidin channel lifetime. *Biophys J* 50:1061–70.
- [7] Wiggins P, Phillips R (2005) Membrane-protein interactions in mechanosensitive channels. *Biophys J* 88:880–902.
- [8] Tosh RE, Collings PJ (1986) High pressure volumetric measurements in dipalmitoylphosphatidylcholine bilayers. *Biochim Biophys Acta* 859:10–4.
- [9] Seemann H, Winter R (2003) Volumetric properties, compressibilities and volume fluctuations in phospholipid-cholesterol bilayers. *Zeitschrift fur physikalische Chemie* 217:831–846.
- [10] Marsh D (2006) Elastic curvature constants of lipid monolayers and bilayers. *Chem Phys Lipids* 144:146–59.

- [11] Nielsen C, Goulian M, Andersen OS (1998) Energetics of inclusion-induced bilayer deformations. *Biophys J* 74:1966–83.
- [12] Helfrich W, Servuss RM (1984) Undulations, steric interactions and cohesion of fluid membranes. *Il Nuovo Cimento* 3:137–151.
- [13] Weikl TR, Kozlov MM, Helfrich W (1998) Interaction of conical membrane inclusions: Effect of lateral tension. *Phys Rev E* 57:6988–6995.
- [14] Ma L (2009) Finite element modeling of shell structures in cell biology: Applications for cell membranes and viral capsids. *PhD Dissertation, UCLA*.
- [15] Kuzmin PI, Akimov SA, Chizmadzhev YA, Zimmerberg J, Cohen FS (2005) Line tension and interaction energies of membrane rafts calculated from lipid splay and tilt. *Biophys J* 88:1120–33.
- [16] Buboltz JT, Bwalya C, Williams K, Schutze M (2007) High resolution mapping of phase behavior in a ternary lipid mixture: Do lipid-raft phase boundaries depend on sample-prep procedure? *Langmuir* 23:11968–11971.
- [17] Veatch SL, Keller SL (2003) Separation of liquid phases in giant vesicles of ternary mixtures of phospholipids and cholesterol. *Biophys J* 85:3074–83.
- [18] Canny J (1986) A computational approach to edge detection. *IEEE Transactions on Pattern Analysis and Machine Intelligence* PAMI-8:679–698.